Title
Highly Active Heterogeneous Catalysts for Carbon Dioxide Reduction to Value-Added Chemicals

Author
Kim, Sunkyu

Publication Date
2021

UNIVERSITY OF CALIFORNIA,
IRVINE

Highly Active Heterogeneous Catalysts for Carbon Dioxide Reduction to Value-Added Chemicals

DISSERTATION

submitted in partial satisfaction of the requirements
for the degree of

DOCTOR OF PHILOSOPHY

in Chemical and Biomolecular Engineering

by

Sunkyu Kim

Dissertation Committee:
Assistant Professor Erdem Sasmaz, Chair
Professor Plamen Atanassov
Professor Ali Mohraz

2021

DEDICATION

To

my loving parents, sister, and friends

in recognition of their worth

TABLE OF CONTENTS

LIST OF FIGURES

LIST OF TABLES

Page

ACKNOWLEDGEMENTS

I would like to express the deepest appreciation to my committee chair, Assistant Professor Erdem Sasmaz, who has continually been supportive of my success in regard to research and scholarship. Without his guidance and invaluable advice, this dissertation would not have been possible.

I would also like to thank my committee members, Professor Plamen Atanassov and Professor Ali Mohraz for serving on my dissertation committee and their valuable time. I remain thankful for them who have helped me reach my goal throughout the time of study here.

I thank the Elsevier for permission to include Chapter One of my dissertation, which was originally published in *Applied Catalysis B: Environmental*. I thank Professor Jochen Lauterbach, Dr. Michael J. Lance, Nicole Cordonnier, and Bradie S. Crandall as the co-author listed in this publication for co-working. I also thank American Chemical Society for permission to include portion of Chapter two of my dissertation, which was originally submitted in *ACS Catalysis*.

VITA

Sunkyu Kim

2014	B.S. in Chemical Engineering, Inha University, South Korea
2016	M.S. in Chemical Engineering, Inha University, South Korea
2021	Ph.D. in Chemical and Biomolecular Engineering, University of California, Irvine, USA

FIELD OF STUDY

Heterogeneous Catalysis and Reaction Engineering

ABSTRACT OF THE DISSERTATION

Highly Active Heterogeneous Catalysts for Carbon Dioxide Reduction to Value-Added Chemicals

by

Sunkyu Kim

Doctor of Philosophy in Chemical and Biomolecular Engineering

University of California, Irvine, 2021

Assistant Professor Erdem Sasmaz, Chair

Carbon dioxide (CO_2) utilization is indispensable to reduce high atmospheric CO_2 concentration, attributing to global warming and ocean acidification. Reduction of CO_2 into high value-added chemicals and fuels is a promising process to mitigate CO_2 emissions and opens possibilities to have carbon-based energy production with net-zero carbon emissions. CO_2 is the most oxidized form of carbon and thermodynamically stable. To effectively reduce CO_2, nanotubular yolk–shell catalysts for methane reforming, and tandem catalysts for direct CO_2 hydrogenation to light olefins were developed. In the former process, Ni yolks encapsulated with SiO_2 shell demonstrated excellent stability with a high resistance to carbon deposition in the confined morphology due to the efficient CO desorption. Forming Pt–Ni single-atom alloys on the yolks pushed the catalyst operating temperature down to 500 °C and further improved the catalyst stability due to the enhanced Ni reducibility. In the latter process, indium oxide supported on zirconia and SAPO-34 zeolite were operated as a tandem catalyst to produce a high light olefins selectivity by shifting the reaction equilibrium to the right for the CO_2 to methanol conversion. Zirconia promoted with yttria (YSZ) inhibited the reduction and hydroxylation of active indium sites. The improved oxygen vacancy formation in YSZ and strong metal–support interaction between indium oxide and YSZ resulted in stable light olefins production. These discoveries can be adopted to the current power generation and manufacturing processes to utilize CO_2 emissions to produce high value-added chemicals with net-zero carbon emissions.

INTRODUCTION

Serious climate change arising from the large amount of greenhouse gas (GHG) emissions by anthropogenic activities should be hindered by mitigating the emissions. Many efforts contributed from global institutions have emphasized that limiting the temperature increase below 2 °C by 2050 is required to slow down the climate change.[1] At the same time, the need for valuable chemical resources has been exponentially grown by human civilization in the modern times, and the global energy consumption is projected to rise by 50% between 2020 and 2050.[2] While the renewable energy consumption is expected to suppress the fossil-based energy consumption by 2050, the global natural gas and liquid fuel consumption are expected to rise by 40% and 20%, respectively. Therefore, it is imperative to develop the process to convert cheap and abundant sources into high value-added chemicals and fuels to solve both environmental concerns and meet the growing energy demand at the same time. GHG emissions have been continuously increasing over the decades, with CO_2 being the primary GHG, accounting for 82%, followed by methane (CH_4), composing 10% by human activities. The combustion of fossil fuels for electricity generation remains the largest source of CO_2 emissions in the US.[3–5] Figure 1 shows global carbon emissions from fossil fuels since 1900, and CO_2 emissions have increased

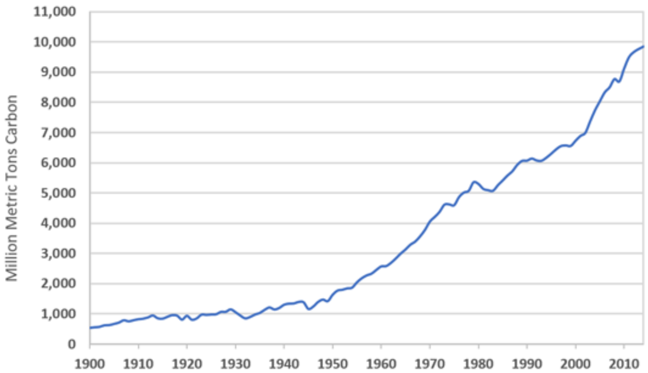

Figure 1. Global carbon emissions from fossil fuels

by more than 100% since 1970. The CO_2 emissions are related to energy consumption and economic growth, and they need to be controlled to mitigate their effect on climate change.[6]

The main climate change mitigation can be employed by decarbonization techniques through renewable energy, carbon capture and storage, or switching to low-carbon fuels.[7] The CO_2 gas captured or separated from fossil fuels-based processes can be utilized in the production of chemicals and fuels by introduction of alternative energy sources.[8] Although transforming CO_2 as the direct carbon source to chemicals and fuels cannot eliminate carbons over the complete life cycles, it can produce more environmental production, which also can solve the high energy demand in modern society. Transition to a low-carbon such as natural gas can be a promising approach to realize a net-zero carbon economy and environmental sustainability. Natural gas contains CH_4 which can be converted to hydrogen (H_2) with thermal processes through methane reforming.[9,10] The H_2 created by the methane reforming can be implanted to other reactions such as reverse water-gas shift (RWGS) or CO_2 hydrogenation in order to produce high value-added chemicals such as methanol, light olefins, and diesel.[11] Therefore, efficient and selective catalysts in an integrated reactor with a minimum of energy cost need to be developed to produce targeted products and realize a low carbon economy.

CHAPTER 1

Nanotubular Yolk–Shell Catalysts for Tri-Reforming of Methane

1.1 Introduction

Many concepts have been explored to utilize CO_2 as a feedstock including hydrogenation, reforming, mineralization, photoreduction, electroreduction, co-polymerization and bio-catalytic conversion.[12–15] Among them, synthesis gas (syngas, a mixture gas of H_2 and carbon monoxide) production through the application of reforming is proposed to be a valuable technology, which can be developed in the midterm by using novel catalytic routes to break C–O bonds and convert CO_2 to valuable chemicals.[12,16,17] Tri-reforming of methane (TRM) is a unique process that can be applied to utilize CO_2 emissions directly from a combustion source using natural gas as the primary reactant.[10,18–20] It has been reported that fossil fuel-fired power plants integrated with the TRM process could reduce CO_2 emissions by up to 85%.[21] TRM involves synergetic combination of dry reforming of methane (DRM, (1.1)), steam reforming of methane (SRM, (1.2)), and partial oxidation of methane (POM, (1.3)) as shown in the following reactions:

$$CH_4 + CO_2 \rightarrow 2CO + 2H_2 \qquad \Delta H^o = +247.3\ \mathrm{kJ \cdot mol^{-1}} \qquad (1.1)$$

$$CH_4 + H_2O \rightarrow CO + 3H_2 \qquad \Delta H^o = +206.3\ \mathrm{kJ \cdot mol^{-1}} \qquad (1.2)$$

$$CH_4 + (1/2)O_2 \rightarrow CO + 2H_2 \qquad \Delta H^o = -35.6\ \mathrm{kJ \cdot mol^{-1}} \qquad (1.3)$$

In TRM, the CO_2 in the flue gas can be converted to syngas by DRM. DRM produces a H_2/CO molar ratio of 1, which can potentially be used for the production of liquid hydrocarbons and oxygenates.[22] Although DRM has the advantage of utilizing CO_2 as an oxidizer, it is a highly endothermic reaction, and it needs a pure CO_2 stream with suffering from carbon deposition leading to catalyst deactivation.[23–25] Coupling DRM with SRM and POM can provide the advantage of adjusting the H_2/CO molar ratios produced between 1 and 2.5, desired for the Fischer–Tropsch, methanol, and dimethyl ether synthesis.[26–30] Incorporation of H_2O and O_2 as an oxidizer into the feed stream can eliminate carbon deposition and reduce energy needs through POM.[31,32] The synergetic combination of three reactions in TRM eliminates the need for pre-separate CO_2, which can further decrease the energy consumption and cost of operation.

Nickel (Ni)-based catalysts are widely studied for TRM as they have a low cost compared to noble metals and show high activity at 750 ºC.[10,18,20,33,34] The addition of promoters to the Ni-based catalysts can further increase the activity and stability of the material by strengthening the metal–support interaction, providing high oxygen storage capacity and creating strong basic sites for CO_2 activation.[35–37] Ni structures supported or promoted with ceria (CeO_2) can improve the TRM activity, as CeO_2 can store and release oxygen reversibly due to its oxygen vacancies and reversible valence redox property (Ce^{3+}/Ce^{4+}).[38,39] In addition to the promoters, the effect of CeO_2-based supports on TRM activity has been investigated, in which small Ni particle sizes on CeO_2-based supports are reported to be beneficial for stable activity.[40,41] In these earlier studies, the effect of promoters or order of metal impregnation on the TRM activity has been examined. However, the interaction among active Ni, promoter, and support, and the effect of particle size on the TRM activity has not been identified.

Catalyst morphologies with unique physical and chemical properties, i.e., core/yolk–shell structures have been investigated in reforming reactions and shown to have high resistance to carbon deposition and sintering due to the confinement effect and enhanced metal–support interaction.[42–51] Compared to the core–shell, the yolk–shell structures (Figure 1.1) contain a void space between the core metals and the outer shell materials which can provide additional properties to the material. The unique nanoreactor environment of the yolk–shell can facilitate chemical storage and confinement of the reactants, intermediates, and products. The cavity between the yolk and shell provides not only high exposed active areas but also a homogenous environment for catalysis.[52–56] Few papers have been published on the core/yolk–shell catalysts for DRM and POM. These studies emphasize that shell thickness, yolk size, pore size and porosity can influence the activity and stability of core/yolk–shell catalysts for DRM.[57–59] In addition, core–shell catalysts promoted with La and Ce can further improve the stability of the catalyst by reducing the surface carbon growth in DRM and POM.[52,60] To date, there is only one study reported the activity of a Ni@SiO_2 core–shell catalyst under various feed stream concentrations in TRM. In this study, formation of a core–shell structure is inconclusive and the

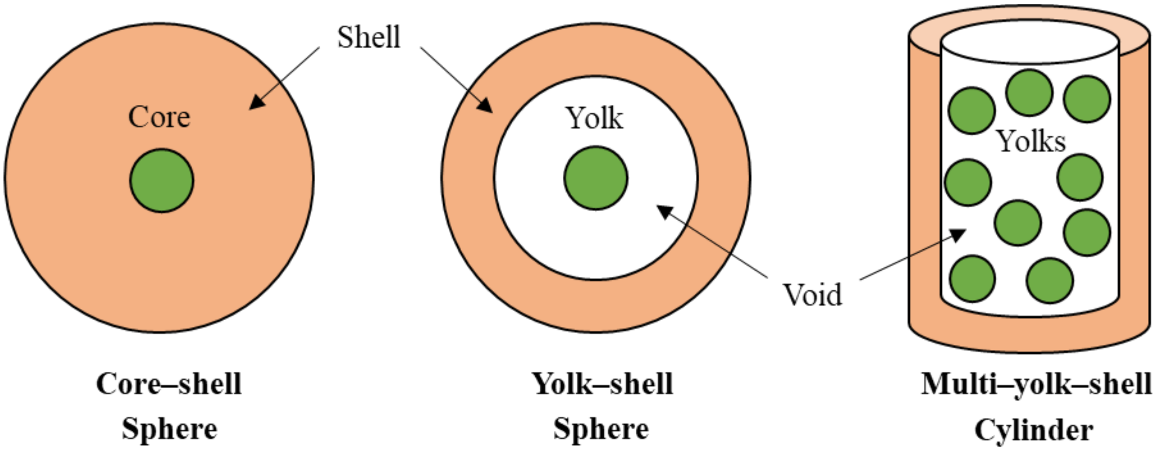

Figure 1.1. Schematic illustration of the core–shell, yolk–shell, and nanotubular multi–yolk–shell structures.

effect of Ni particle size on the TRM activity at various oxidizer to methane feed ratios could not be understood.[61]

It is important to note that TRM can be operated at different oxidizer ($CO_2 + H_2O + O_2$) to methane (O/M) feed ratios. Variations in CH_4 concentration in the feed stream can dramatically influence the catalyst performance for TRM. Generally, a catalyst for TRM should be able to exhibit high carbon resistance under reducing conditions ($O/M \leq 1$), while re-oxidation of active metallic Ni to NiO should be hindered under oxidizing conditions ($O/M > 1$).[61,62] Most of the studies involving core/yolk–shell structures were performed under DRM conditions, and the effects of catalyst morphology and Ni–promoter interaction on the TRM activity at various O/M feed ratios have not been investigated. In this work, we have evaluated the TRM activity and stability of nanotubular NiCe@SiO_2 multi–yolk–shell catalysts at different O/M feed ratios and identified the influence of yolk size and Ni–Ce interaction on the catalytic performance. To the best of our knowledge, this is the first study reporting the effect of morphology on the activity of the yolk–shell structured catalysts at various O/M feed ratios under TRM.

1.2 Experimental Methods

1.2.1 Catalyst synthesis

The nanotubular NiCe@SiO_2 multi–yolk–shell catalyst was synthesized by reverse microemulsion method, and the chemical reagents were used as purchased without any further purification. The solution containing 0.2 M nickel nitrate hexahydrate ($Ni(NO_3)_2 \cdot 6H_2O$, 98%, Alfa Aesar) and 0.05 M cerium nitrate hexahydrate ($Ce(NO_3)_3 \cdot 6H_2O$, 99%, Sigma Aldrich) in 4 ml of deionized (DI) water was added dropwise to the microemulsion dissolved in 0.17–0.26 M 1-hexadecyl trimethyl ammonium bromide (CTAB) ($CH_3(CH_2)_{15}N(CH_3)_3Br$, 98%, Alfa Aesar) in 15 ml of 1-butanol ($CH_3(CH_2)_3OH$, anhydrous, 99.8%, Sigma Aldrich) and 80 ml of cyclohexane (C_6H_{12}, 99%, Alfa Aesar) mixture. After stirring the solution for 1 h, the transparent microemulsion solution was heated up to 70 °C in an oil bath, and 0.7 ml of hydrazine (N_2H_4, anhydrous, 98%, Sigma Aldrich) with 0.5 M sodium hydroxide (NaOH, Fisher Chemical) in 1.5 ml DI was added to the solution dropwise, followed by further stirring for 40 min. The solution was cooled down to room temperature and aged for another 2 h under stirring. Finally, 1.5 ml of tetraethyl orthosilicate (TEOS) ($Si(OC_2H_5)_4$, 99% Sigma Aldrich) was added to the solution dropwise, and after 1 h, 1.5 ml of ammonium hydroxide solution (NH_4OH, 28% NH_3, Alfa Aesar) was added to the solution dropwise. The final solution was aged for 1 day for hydrolysis and condensation of the silica precursor. The solution was washed with ethanol and separated by centrifuging. The washed sample was dried at 100 °C overnight, and then calcined in static air at 500 °C for 4 h with a ramping rate of 5 °C min^{-1}. Different yolk sizes and tube diameters can be obtained by controlling the water to surfactant (CTAB) molar ratio. A low water/CTAB ratio leads to larger yolk size with a shorter tube diameter, and a high water/CTAB ratio forms a smaller yolk size with a longer tube diameter. $NiCe@SiO_2^A$, $NiCe@SiO_2^B$, and $NiCe@SiO_2^C$ catalysts were prepared in a water to CTAB ratio of 12.6, 15.8, and 18.9, respectively. For comparison, conventional $NiCe/SiO_2^{WI}$ was synthesized by a wet impregnation method. 0.02 M $Ni(NO_3)_2 \cdot 6H_2O$, 0.005 M $Ce(NO_3)_3 \cdot 6H_2O$, and 0.5 g of fumed silica (SiO_2, Sigma Aldrich) were mixed in 50 ml ethanol (C_2H_6O, anhydrous, Fisher Chemical). The whole mixture was stirred overnight, and the material was dried at 100 °C overnight, followed by calcination at 500 °C in stagnant air for 4 h with a ramping temperature rate of 5 °C min^{-1}.

1.2.2 Characterization

Field emission scanning electron microscopy (FESEM, Zeiss Ultra plus) and transmission electron microscopy (TEM, Hitachi H8000) images were obtained to investigate the morphology of the catalysts. Histogram distributions of yolk size were generated by analyzing TEM images, and 100 yolks were used for each distribution. The elemental mapping of the catalysts was collected using a scanning transmission electron microscope (STEM, FEI Talos F200X). The weight percent of Ni and Ce in the samples was analyzed by inductively coupled plasma optical emission spectroscopy (ICP-OES, Optima 2000 DV). Powder X-ray diffraction (XRD) patterns of the catalysts were obtained by using a Rigaku MiniFlex II with CuKα source radiation ($\alpha = 1.5406$) for 2θ range of 10°–80° with a step rate of $2° \text{ min}^{-1}$. The crystallite size of the components was calculated using the Scherrer equation from the peaks at the (111) phase of each chemical element. The specific surface area of the sample was measured using a Micromeritics ASAP 2020. The samples were degassed at 300 °C for 7 h to remove the moisture prior to the measurements. Hydrogen temperature programmed reduction (H_2-TPR) was performed using a Micromeritics AutoChem II to identify the interaction between active species and supports and determine the reducibility of the catalysts. First, 50 mg of catalyst was heated up to 300 °C and held for 1 h under He flow to eliminate moisture and contaminants, and then cooled down to 30 °C. After the preparation step, the temperature of the catalyst was increased from 30 °C to 900 °C at a ramping rate of 10 °C min^{-1} in a 10% H_2/Ar mixture, and the H_2 consumption was monitored by a thermal conductivity detector (TCD). The amount of H_2 reduced was calibrated by using CuO. H_2 pulse chemisorption experiments were performed with the same apparatus as H_2-TPR to determine the dispersion of Ni. First, 100 mg of catalyst was reduced under 10% H_2/Ar at 600 °C for 5 h. Then the catalyst was purged at 610 °C for 1 h and cooled down to 35 °C under He flow. H_2 pulse chemisorption was conducted at 35 °C in 10% H_2/Ar with 8 min intervals. The oxidation states of the elements presented in catalysts were determined by X-ray photoelectron spectroscopy (XPS) with a Kratos Axis Ultra DLD using AlKα radiation, and the binding energy was calibrated to the signal of C 1s at 284.8 eV. The spectra were obtained after the samples were reduced in H_2 at 600 °C for 1 h. Thermogravimetric analysis (TGA) was employed using a TGA-50 Shimadzu to determine carbon deposition on the spent catalyst. The sample weight loss was characterized under air flow from 30 °C to 900 °C with a ramping temperature of 10 °C min^{-1}. Raman spectra were obtained using an XploRA PLUS system from Horiba in the backscattering configuration at a 638 nm wavelength to determine the nature of carbon formed on the spent catalyst.

1.2.3 TRM activity

The performance of the catalyst for TRM was tested in a fixed-bed reactor at atmospheric pressure. 75 mg of the catalyst was placed between quartz wool in a quartz reactor with an inner diameter of 7 mm. Water was injected into an evaporator via a peristaltic pump and mixed with the reaction gases. The reaction gases (CH_4, CO_2, O_2, and N_2) were introduced to the evaporator via mass flow controllers. The reactor was placed in a furnace and the temperature of the catalyst was measured by a K-type thermocouple placed inside the catalyst bed. The effluent gases were passed through a condenser in which water vapor was removed, and their concentration was measured with a gas chromatograph (GC) using TCD. Prior to the reaction, all catalysts were reduced at 600 °C for 1 h with 25% H_2 balanced with N_2. Following the reduction, the catalysts were heated up to a reaction temperature of 750 °C under N_2 flow. The TRM reaction was carried out for 20 h in a gas hourly space velocity (GHSV) of 60,000 ml g^{-1} h^{-1} at different O/M feed ratios including 0.85 ($CH_4 : CO_2 : H_2O : O_2 = 2.59 : 1 : 1 : 0.2$), 1 ($CH_4 : CO_2 : H_2O : O_2 =$

2.2 : 1 : 1 : 0.2), 1.1 (CH_4 : CO_2 : H_2O : O_2 = 2 : 1 : 1 : 0.2) and 1.25 (CH_4 : CO_2 : H_2O : O_2 = 1.76 : 1 : 1 : 0.2). The catalytic activity was calculated using the following equations:

$$\text{Conversion (\%)} = \frac{F_{\text{react,in}} - F_{\text{react,out}}}{F_{\text{react,in}}} \times 100 \qquad (1.4)$$

$$H_2 \text{ yield (\%)} = \frac{F_{\text{H2,out}}}{2F_{\text{CH4,in}} + F_{\text{H2O,in}}} \times 100 \qquad (1.5)$$

$$\text{CO yield (\%)} = \frac{F_{\text{CO,out}}}{F_{\text{CO2,in}} + F_{\text{CH4,in}}} \times 100 \qquad (1.6)$$

$$H_2/\text{CO ratio} = \frac{F_{\text{H2,out}}}{F_{\text{CO,out}}} \qquad (1.7)$$

where F is the molar flow rate of the reagent species measured at the inlet and outlet of the reactor. The reproducibility of the catalytic activity for all experiments is within ±5%.

1.3 Results and Discussion

1.3.1 Characterization of fresh catalysts

Figure 1.2a–c show TEM images of nanotubular NiCe@SiO_2^A, NiCe@SiO_2^B, and NiCe@SiO_2^C multi–yolk–shell catalysts synthesized in a solution containing water/CTAB molar ratios of 12.6, 15.8, and 18.9, respectively. The yolk nanoparticles of each catalyst are shown to be dispersed uniformly with a mean size of 32.9 nm, 23.7 nm, and 20.0 nm for NiCe@SiO_2^A, NiCe@SiO_2^B, and NiCe@SiO_2^C, respectively. The yolks of NiCe@SiO_2^A, NiCe@SiO_2^B, and NiCe@SiO_2^C are encapsulated by SiO_2 with an average tube diameter of 41.8 nm, 243.0 nm, and 275.0 nm, respectively. The nanotubular multi–yolk–shell structure prepared at a high concentration of CTAB, i.e. NiCe@SiO_2^A, consists of larger yolks with a smaller diameter tube, whereas the nanotubular multi–yolk–shell structure synthesized at a low concentration of CTAB,

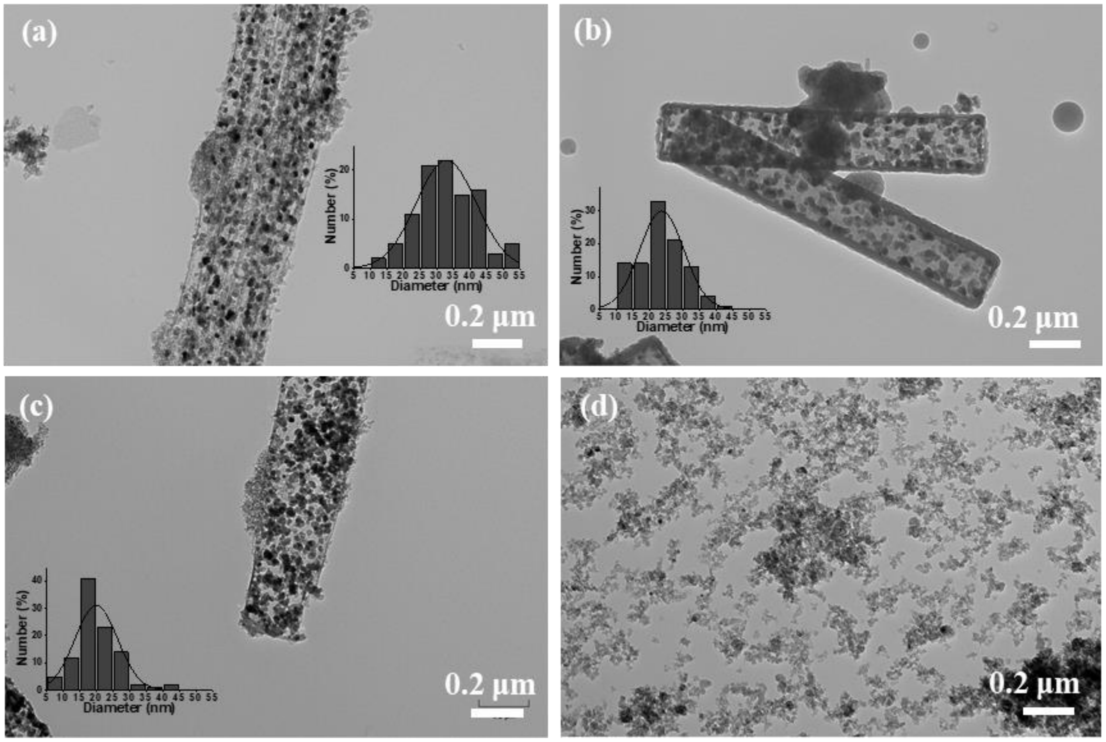

Figure 1.2. TEM images of nanotubular multi–yolk–shell catalysts synthesized in different water to CTAB ratios of (a) 12.6 (NiCe@SiO_2^A), (b) 15.8 (NiCe@SiO_2^B), and (c) 18.9 (NiCe@SiO_2^C) solution. The inset graph shows yolk size distribution. (d) TEM image of NiCe/SiO_2^{WI} synthesized by wet impregnation.

i.e. NiCe@SiO_2^C, has smaller yolks within a larger diameter tube. Compared to the nanotubular multi–yolk–shell structured catalysts, conventional NiCe/SiO_2^{WI} synthesized by wet impregnation method does not show any specific morphology (Figure 1.2d). It is important to note that Ce species are necessary to generate nanotube morphology. For instance, it is observed that Ni@SiO_2 without Ce forms a spherical yolk–shell structure rather than a nanotubular structure when similar amounts of Ni exist as in NiCe@SiO_2 (Figure 1.3). This is because the nanotube formation and elongation is limited by the amount of gas released during the synthesis, in which Ce ions produce double amount of N_2 in comparison to Ni ions during reduction with hydrazine in the synthesis step.[63]

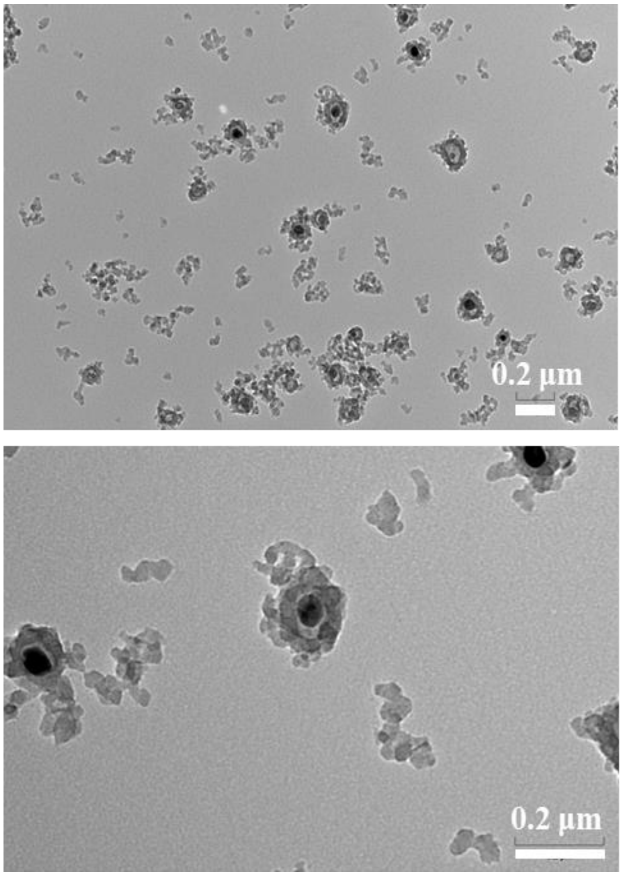

Figure 1.3. TEM images of Ni@SiO_2 synthesized without Ce promoter.

As shown in Figure 1.4, the elemental mapping of STEM images of the NiCe@SiO_2^A and NiCe@SiO_2^C confirm that the yolks are composed of Ni species surrounded by an outer shell consisting of only SiO_2. As shown in Figure 1.4a, accumulation of Ce on larger Ni yolks in NiCe@SiO_2^A is more pronounced than that in NiCe@SiO_2^C with smaller yolks. Ce is found to be more dispersed throughout the catalysts, yet it is mostly accumulated on the Ni yolks indicating the possible Ni–Ce interaction. It is important to note that characteristic X-ray signals detected for Ce in the energy dispersive X-ray (EDX) spectra is low compared to Ni and Si. Although most of the Ce components are inside the nanotube structures, Ce pixels observed outside the nanotubes are possibly due to the low signal-to-noise ratio. The contrast change of Si between the edges and inner parts of the nanotube indicates that the SiO_2 shell has a cylindrical tube

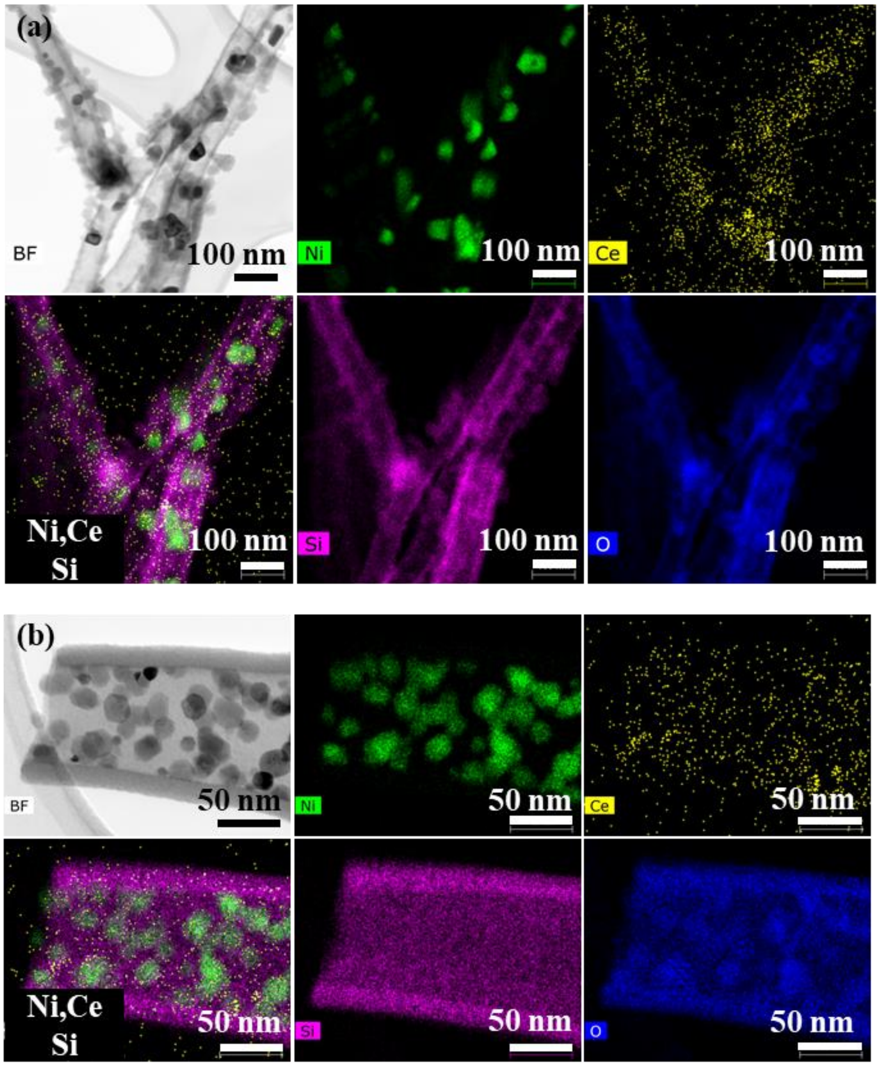

Figure 1.4. EDX elemental mapping images of (a) NiCe@SiO_2^A and (b) NiCe@SiO_2^C (Ni: green, Ce: yellow, Si: magenta, and O: blue).

morphology with the presence of interstitial voids. Both the TEM and STEM images cannot definitively confirm whether the nanotubes are capped at each end. However, the overview SEM images of NiCe@SiO_2^C, shown in Figure 1.5, confirm that the tube structure is hollow on the inside, and both Ni and Ce particles are attached to the inner walls of the hollow tube.

The XRD measurements of the synthesized NiCe@SiO_2^A, NiCe@SiO_2^C, and NiCe/SiO_2^{WI} are shown in Figure 1.6. All three catalysts show NiO and CeO_2 diffraction patterns with an amorphous SiO_2 structure. The peaks at 2-theta of 37.66°, 43.69°, and 63.24° are

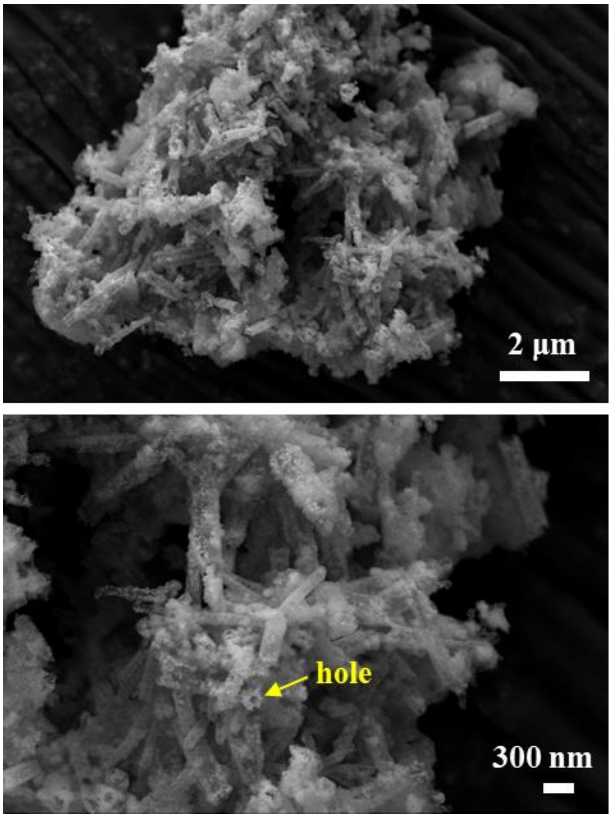

Figure 1.5. SEM images of NiCe@SiO_2^C.

identified as NiO, and the other peaks at 29.20°, 33.74°, 48.10°, 56.92°, and 75.74° belong to the cubic CeO_2 structure. The broad peak at 21.26° indicates the formation of amorphous SiO_2

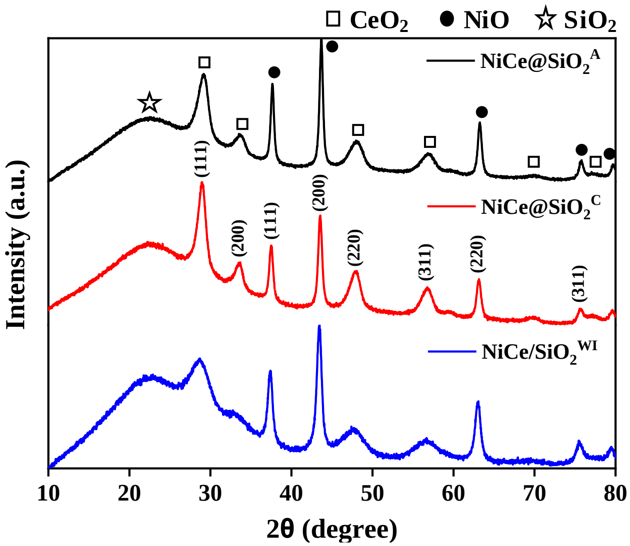

Figure 1.6. XRD patterns of NiCe@SiO_2^A, NiCe@SiO_2^C, and NiCe/SiO_2^{WI}.

shells. Based on the XRD patterns, the NiCe@SiO$_2$^{A} catalyst shows the largest NiO crystallite size of 18.3 nm, followed by 16.2 nm for NiCe@SiO$_2$^{C} and 14.3 nm for NiCe/SiO$_2$^{WI} (Table 1.1).

Table 1.1. Textural properties of NiCe@SiO$_2$^{A}, NiCe@SiO$_2$^{C}, and NiCe/SiO$_2$^{WI}.

Catalysts	Crystallite size (nm)[a]		Surface area ($m^2\ g^{-1}$)[b]	Metal loading (wt%)[c]	
	NiO	CeO$_2$		Ni	Ce
NiCe@SiO$_2$^{A}	18.3 ± 0.2	6.7 ± 1.3	400.3	8.2	5.2
NiCe@SiO$_2$^{C}	16.2 ± 0.8	8.5 ± 1.1	366.9	7.5	5.3
NiCe@SiO$_2$^{WI}	14.3 ± 0.5	4.3 ± 0.3	486.0	7.2	4.6

[a] Calculated according to the Scherrer equation applied to (111) phase. [b] BET surface area. [c] Measured by ICP-OES analysis.

The crystallite sizes of CeO$_2$ for the NiCe@SiO$_2$^{A}, NiCe@SiO$_2$^{C} and NiCe/SiO$_2$^{WI} catalysts are found to be 6.7 nm, 8.5 nm, and 4.3 nm, respectively. NiCe/SiO$_2$^{WI} has the lowest CeO$_2$ crystallite size suggesting that ceria has higher dispersion and larger amount of oxygen vacancies than NiCe@SiO$_2$^{A} followed by NiCe@SiO$_2$^{C}.[64] The average yolk size of NiCe@SiO$_2$^{A} measured by TEM (32.9 nm) is much larger than the NiO crystallite size calculated by XRD (18.3 nm) indicating that the yolks in NiCe@SiO$_2$^{A} are possibly formed with grain. On the other hand, the average yolk size of NiCe@SiO$_2$^{C} by TEM (20.0 nm) matches reasonably well with the NiO crystallite size (16.2 nm). Figure 1.7 represents the XRD diffraction patterns of NiCe@SiO$_2$^{A}, NiCe@SiO$_2$^{C}, and NiCe/SiO$_2$^{WI} after one hour of H_2 reduction at 600 °C. The peaks at 2-theta of 45.08°, 52.4°, and 76.84 correspond to metallic Ni phase. The NiO phase is not detected, indicating that NiO was fully reduced to metallic Ni in all catalysts. The Ni crystallite size of NiCe/SiO$_2$^{WI} has the smallest value of 10.4 nm followed by 12.2 nm for NiCe@SiO$_2$^{A} and 14.9 nm for NiCe@SiO$_2$^{C}. The crystalline CeO$_2$ peaks get broader after the reduction, suggesting that

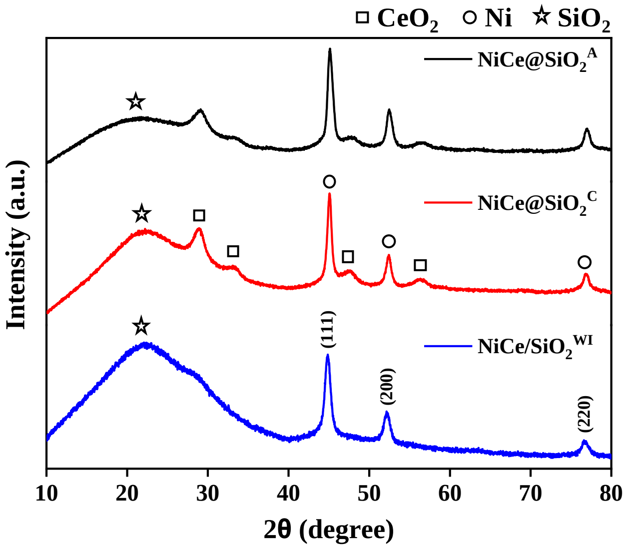

Figure 1.7. XRD patterns of NiCe@SiO$_2^A$, NiCe@SiO$_2^C$, and NiCe/SiO$_2^{WI}$ after H_2 reduction at 600 °C for 1 h.

the phase transition of crystalline CeO_2 into Ce_2O_3 has been initiated. For NiCe/SiO$_2^{WI}$, no CeO_2 peaks are observed due to the formation of highly dispersed CeO_x particles.[65]

The textural properties of the catalysts such as specific surface area and metal weight percentages are presented in Table 1.1. The NiCe@SiO$_2^A$ catalyst with smaller tube diameter provides larger surface area than the NiCe@SiO$_2^C$ catalyst, while the NiCe/SiO$_2^{WI}$ catalyst has the highest surface area of 486.0 m^2 g^{-1} among three catalysts. The weight percentages of Ni and Ce are measured to be in between 7.2–8. 2 wt% and 4.6–5.3 wt% by ICP-OES in all three catalysts, respectively. The nitrogen adsorption-desorption isotherms of the NiCe@SiO$_2^A$, NiCe@SiO$_2^C$, and NiCe/SiO$_2^{WI}$ catalysts are shown in Figure 1.8. The isotherms of NiCe@SiO$_2^A$ and NiCe@SiO$_2^C$ show type IV isotherm with H3 hysteresis, while NiCe/SiO$_2^{WI}$ has a type IV isotherm with H2 hysteresis. Both H2 and H3 hysteresis indicate that all three catalysts have a porous structure. However, isotherms of type IV with H3 hysteresis can be

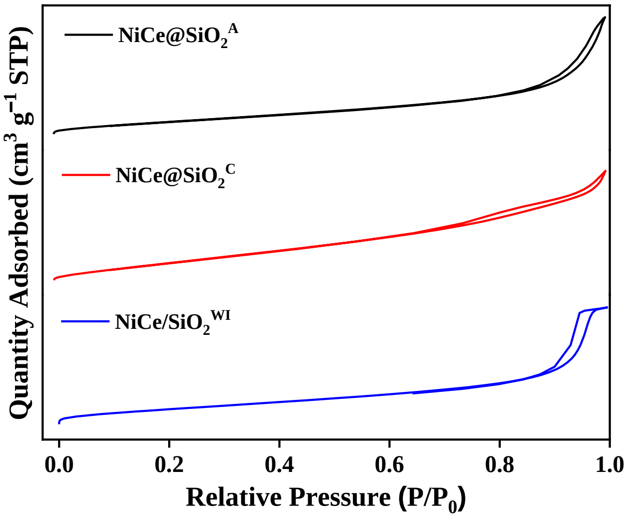

Figure 1.8. N_2 adsorption-desorption isotherms of NiCe@SiO$_2^A$, NiCe@SiO$_2^C$, and NiCe/SiO$_2^{WI}$.

found in a hierarchical porous structure consisting of mesopores and macropores, which is consistent with the morphology of the nanotubular multi–yolk–shell structure.[66]

H_2-TPR experiments are conducted to determine the reducibility of the synthesized catalysts and interaction between the active sites and support. The H_2-TPR profiles of the Ni@SiO$_2$, Ni/SiO$_2^{WI}$, and Ce/SiO$_2^{WI}$ catalysts were also analyzed to elucidate the effect of the Ce promoter (Figure 1.9). As shown in Figure 1.10, three temperature regions are found to exist for the NiCe@SiO$_2^A$, NiCe@SiO$_2^C$, and NiCe/SiO$_2^{WI}$ catalysts. The first H_2 consumption peak of α at temperatures between 215 °C and 400 °C is attributed to the combination of two reduction peaks of bulk NiO and aggregated NiO particles interacting more with the oxygen vacancies of CeO_2, in which the latter is expected to be at lower temperatures as oxygen vacancies improve the reducibility of NiO.[36,49,67] Compared to Ni@SiO$_2$ (Figure 1.9), the α peak in the Ce promoted catalysts shifts to a lower temperature (311 °C) for NiCe@SiO$_2^A$ and a higher temperature (333 °C) for NiCe@SiO$_2^C$. This can be explained by the yolk size effect and the formation of oxygen vacancies in the CeO_2 lattice, as smaller yolks have less Ni–Ce

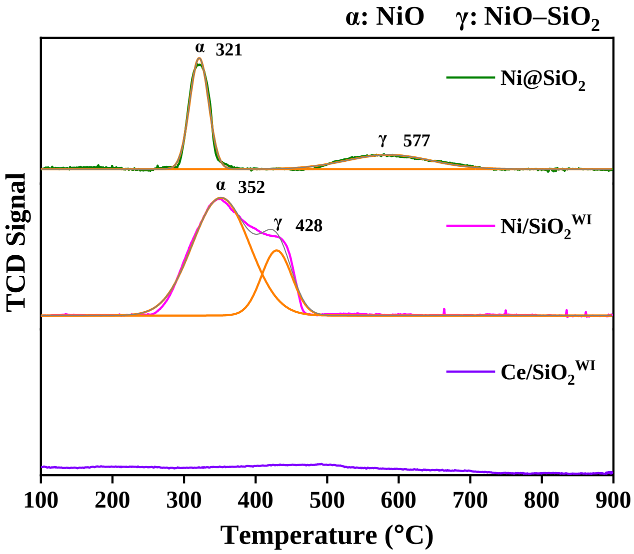

Figure 1.9. H_2-TPR profiles of Ni@SiO$_2$, Ni/SiO$_2^{WI}$, and Ce/SiO$_2^{WI}$.

interaction and are harder to be reduced than the catalyst with larger yolks.[68] The H_2 consumption peak of β in the medium temperature region is associated with the dispersed Ni species interacting with CeO_2.[69] Formation of the β peak at slightly higher temperatures than the bulk NiO one has been observed by several other researchers.[36,68] It is possible that dispersed Ni particles might have stronger interaction with SiO_2 support, which can shift the Ni–Ce reduction

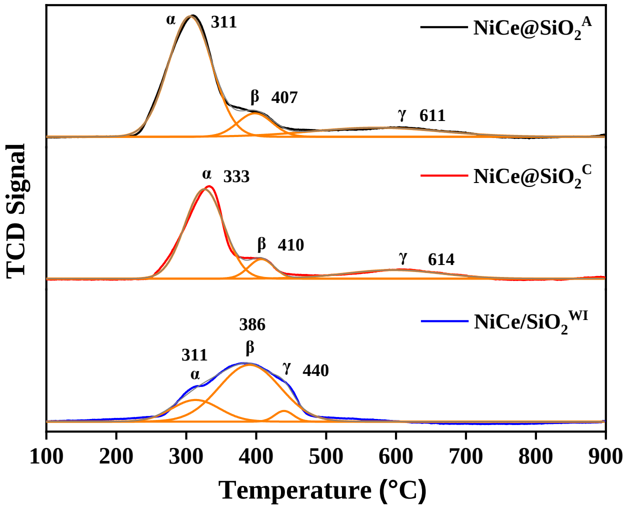

Figure 1.10. H_2-TPR profiles of NiCe@SiO$_2^A$, NiCe@SiO$_2^C$, and NiCe/SiO$_2^{WI}$.

peaks to a higher temperature than the bulk NiO one.[52,68] In the case of NiCe/SiO_2^{WI}, the α peak consists of NiO particles interacting more with the surface oxygen vacancies of CeO_2, and the NiO reduction peak observed at 352 °C on Ni/SiO_2^{WI} (Figure 1.9) shifts to 386 °C after Ce promotion due to an enhanced NiO–SiO_2 interaction. The H_2 consumption peak of γ at temperatures above 400 °C is assigned to the NiO particles strongly bonded to the SiO_2 support. The broad γ peak for nanotubular multi–yolk–shell catalysts is located in a higher temperature region compared to the impregnated catalyst. This indicates that NiO–SiO_2 interaction in NiCe@SiO_2 is stronger than that in NiCe/SiO_2^{WI} due to the encapsulation of Ni and Ce yolks by mesoporous SiO_2.[44,70] The H_2 uptake of the nanotubular multi–yolk–shell and impregnated catalysts are compared with the actual Ni amount loaded on the catalyst, as shown in Table 1.2.

Table 1.2. H_2 uptake during H_2-TPR experiments for NiCe@SiO_2^{A}, NiCe@SiO_2^{C}, and NiCe/SiO_2^{WI}.

Catalyst	Overall Ni (mmol)[a]	H_2 uptake (mmol)			α/β
		α	β	γ	
NiCe@SiO_2^{A}	0.070	0.084	0.013	0.019	6.5
NiCe@SiO_2^{C}	0.064	0.056	0.008	0.013	7.0
NiCe@SiO_2^{WI}	0.053	0.017	0.055	0.003	0.3

[a] Measured by ICP-OES analysis.

The overall H_2 consumption is much larger than the theoretical amount of Ni on all three catalysts due to the lattice oxygen reduction of CeO_2 by hydrogen spillover on Ni.[36,69] The H_2 uptake ratio of α/β for the nanotubular NiCe@SiO_2 multi–yolk–shell catalyst is approximately 20 times higher than that of NiCe/SiO_2^{WI} indicating that most of H_2 is consumed by the bulk NiO and aggregated NiO particles interacting with CeO_2. Compared to NiCe@SiO_2^{C}, the higher overall H_2 consumption observed on NiCe@SiO_2^{A} indicates that larger yolks are easily reduced due to the formation of more oxygen vacancies in the CeO_2 lattice.

The Ni particle size and dispersion estimated from the H_2 chemisorption measurements is presented in Table 1.3. For nanotubular NiCe@SiO_2 multi–yolk–shell catalysts, Ni particle size is over 290 nm and much larger than the Ni size observed in TEM and XRD. The large particle size obtained for all catalysts from H_2 chemisorption does not represent the actual Ni particle size, indicating that Ni sites are not available to react with H_2. This difference can be explained by the lack of Ni sites for H_2 chemisorption due to the strong Ni–Ce interaction and partially embedded Ni particles in the SiO_2 support.[55,56,59] The effect of latter on Ni particle size has more pronounced in the nanotubular multi–yolk–shell catalysts compared to the impregnated catalyst, leading to a much larger Ni particle size. As shown in the H_2-TPR experiments (Figure 1.10), the γ reduction peak is located at a high temperature for the nanotubular multi–yolk–shell catalysts indicating a strong NiO–SiO_2 interaction. Ni dispersion has also been calculated through H_2 chemisorption measurements. As shown in Table 1.3, The NiCe/SiO_2^{WI} exhibits the highest Ni dispersion of 1.71%, followed by 0.35% and 0.31% for NiCe@SiO_2^{C} and NiCe@SiO_2^{A}, respectively. Ni dispersions have previously been reported in the range of 0.12–0.27% for Ni based core/yolk–shell structures, which are in consistent with our work.[59,71] The higher Ni dispersion observed on NiCe/SiO_2^{WI} compared to the nanotubular multi–yolk–shell catalysts is consistent with the smaller Ni particle size and higher surface area measured on the NiCe/SiO_2^{WI} catalyst. It is important to note that Ni dispersion on the core/yolk–shell structure in which the

Table 1.3. Physicochemical properties of NiCe@SiO_2^{A}, NiCe@SiO_2^{C}, and NiCe/SiO_2^{WI}.

Catalysts	$Ce^{3+}/(Ce^{3+}+Ce^{4+})$ (%)[a]	Ni particle size (nm)[b]	Ni dispersion (%)[b]
NiCe@SiO_2^{A}	61.6	327.3	0.31
NiCe@SiO_2^{C}	36.1	292.4	0.35
NiCe@SiO_2^{WI}	62.9	59.1	1.71

[a]Obtained from XPS deconvolution. [b]Calculated based on H_2 chemisorption.

active metal is encapsulated by a support can be influenced by the shell material and strong metal–support interaction.[59]

Analysis of the core level XPS spectra of Ni and Ce species shows consistent results with the H_2-TPR measurement. As shown in Figure 1.11a, the Ni 2p core level spectra of the reduced NiCe@SiO_2^A, NiCe@SiO_2^C, and NiCe/SiO_2^{WI} catalysts have characteristic metallic Ni peaks of Ni $2p_{3/2}$ (852.2 eV) and Ni $2p_{1/2}$ (869.5 eV) accompanied by shake-up structures.[41,52] Figure 1.11b shows the Ce 3d core level XPS spectra of the reduced samples. The Ce core level spectra can be deconvoluted into multiple peaks for Ce $3d_{5/2}$ (v) and Ce $3d_{3/2}$ (u). The v and v'' bands are attributed to Ce^{4+}, whereas v_0 and v' bands are assigned to Ce^{3+}. The other bands (v''' and u''') available for Ce could not be detected due to the low signal-to-noise ratio. The relative Ce^{3+} concentration on the catalyst is calculated by the ratio of integrated Ce^{3+} peaks to the total Ce^{3+} and Ce^{4+} peaks ($Ce^{3+}/(Ce^{3+}+Ce^{4+})$). It has been found that NiCe/SiO_2^{WI} has the highest Ce^{3+} concentration of 62.9% followed by 61.6% and 36.1% for NiCe@SiO_2^A and NiCe@SiO_2^C, respectively (Table 1.3). This shows that more oxygen vacancies formed in the CeO_2 lattice by the dispersed NiO particles in NiCe/SiO_2^{WI} and aggregated NiO yolks in NiCe@SiO_2^A.

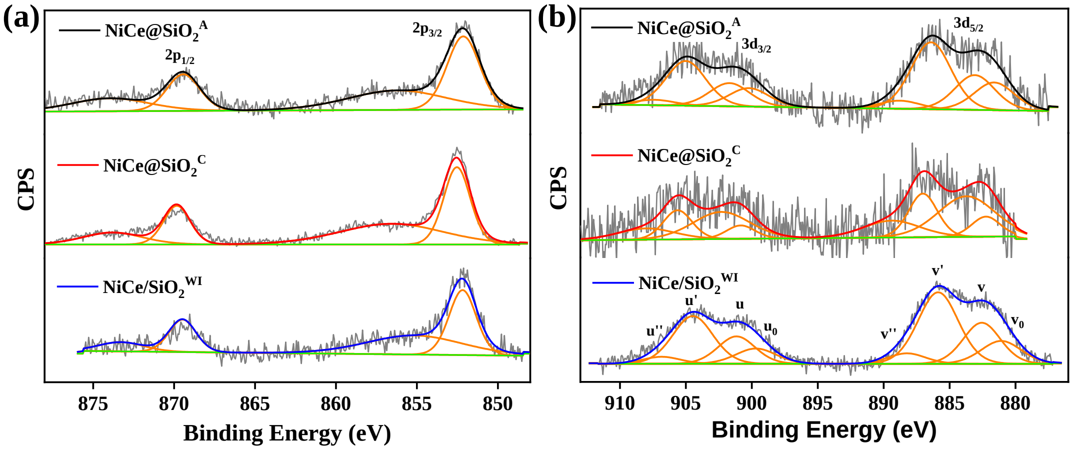

Figure 1.11. (a) Ni 2p and (b) Ce 3d XPS spectra of reduced NiCe@SiO_2^A, NiCe@SiO_2^C, and NiCe/SiO_2^{WI}.

1.3.2 TRM activity

The experiments for TRM were carried out at different O/M feed ratios to determine the activity and stability of the nanotubular multi–yolk–shell and impregnated catalysts. Figure 1.12a,b illustrate CO_2 and CH_4 conversions at 750 °C at O/M feed ratios of 1.1 and 1.0, respectively. As shown in Figure 1.12a, NiCe@SiO_2^A and NiCe/SiO_2^{WI} have comparable CO_2 conversions of 75% and 72%, and CH_4 conversions of 79% and 78% at O/M ratio of 1.1, respectively. NiCe@SiO_2^A and NiCe/SiO_2^{WI} present H_2 and CO yields of 75% and 77%, and 79% and 72% with the same H_2/CO ratio of 1.7, respectively (Figure 1.13). Both catalysts keep their activities stable over the 20 h period of reaction. In contrast, NiCe@SiO_2^C shows an initial CO_2 and CH_4 conversions of 69% and 71%, respectively, yet both CO_2 and CH_4 conversions drop to below 5% within about 5 h. TRM activity of NiCe@SiO_2^A with larger yolks was further tested at a higher O/M feed ratio of 1.25 to examine the catalytic activity and potential deactivation of the catalyst (Figure 1.14). The result shows that the NiCe@SiO_2^A catalyst still presents a stable activity with conversions of 67% and 84% for CO_2 and CH_4, respectively. As the O/M feed ratio decreases to 1.0, the catalysts show distinctive behavior compared to those

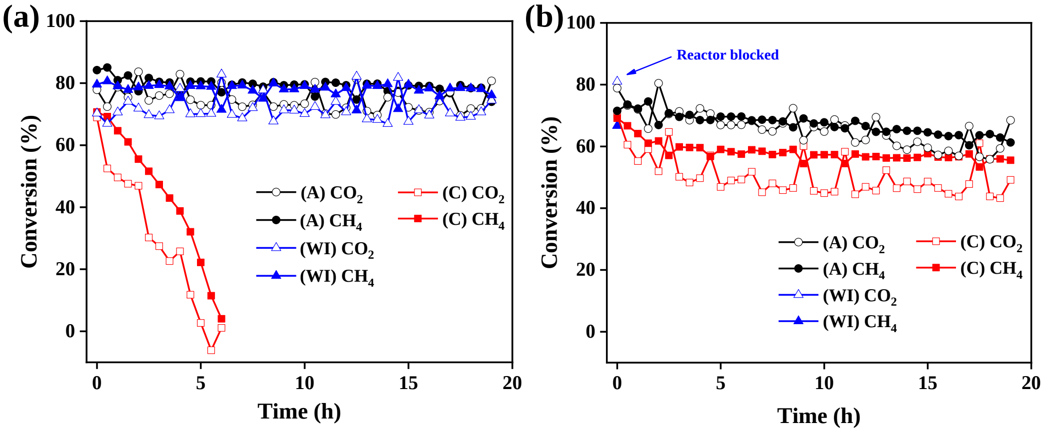

Figure 1.12. CO_2 and CH_4 conversions of (A) NiCe@SiO_2^A, (C) NiCe@SiO_2^C, and (WI) NiCe/SiO_2^{WI} catalysts in O/M ratios of (a) 1.1 and (b) 1.0 feed stream at 750 ºC.

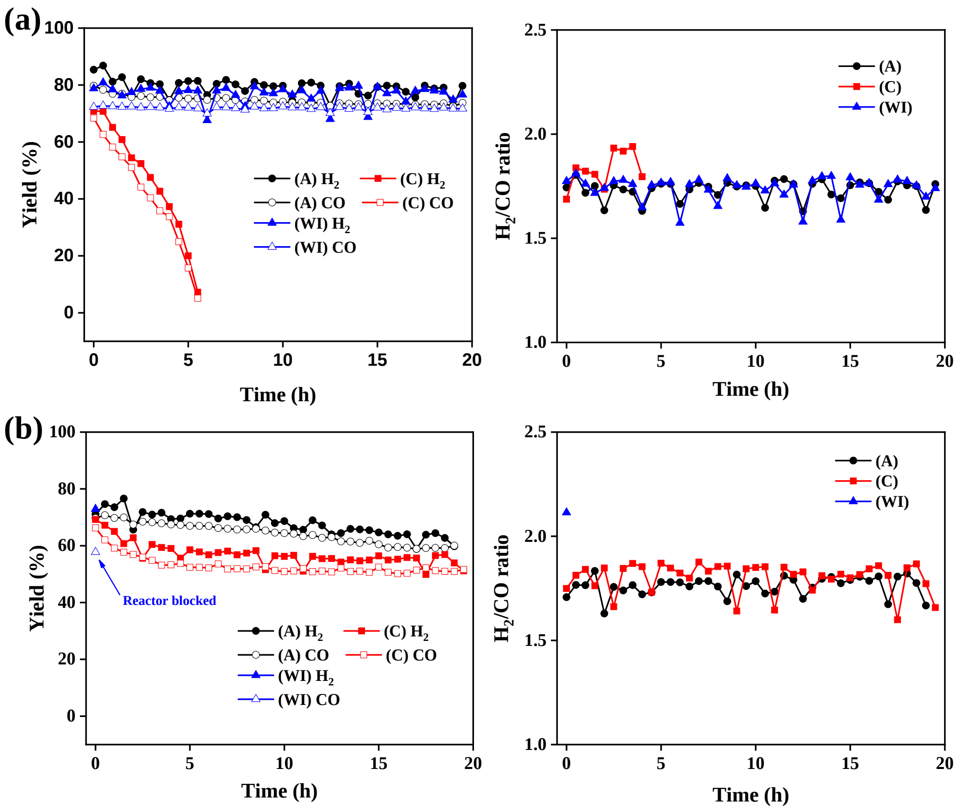

Figure 1.13. H_2 and CO yields and H_2/CO ratio of (A) NiCe@SiO$_2^A$, (C) NiCe@SiO$_2^C$, (WI) NiCe/SiO$_2^{WI}$ in O/M ratios of (a) 1.1 and (b) 1.0 feed stream at 750 ºC.

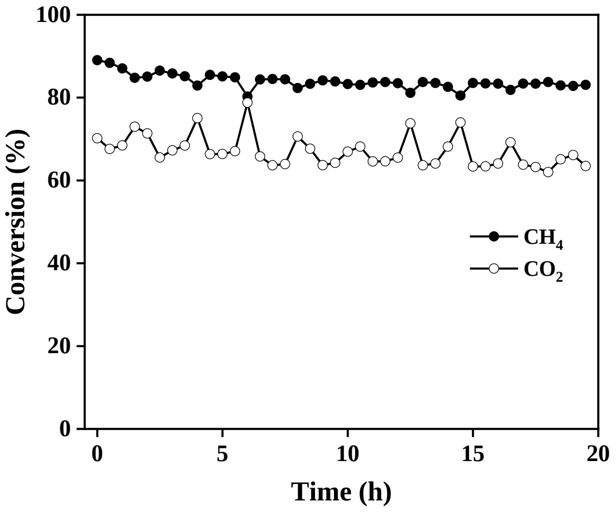

Figure 1.14. CO_2 and CH_4 conversions of NiCe@SiO$_2^A$ in O/M ratio of 1.25 feed stream at 750 ºC.

tested at the O/M feed ratio of 1.1. As shown in Figure 1.12b, NiCe@SiO$_2^A$ and NiCe@SiO$_2^C$

have CO_2 conversions of 66% and 50%, and CH_4 conversions of 67% and 58%, respectively. For NiCe@SiO_2^A, these conversions correspond to the H_2 and CO yields of 68% and 64% with a H_2/CO ratio of 1.8 (Figure 1.13). The conventional NiCe/SiO_2^{WI} starts with similar conversion as the nanotubular multi–yolk–shell catalysts, however, the conversions plummet after about 1 h (Figure 1.12b). The fast deactivation of NiCe/SiO_2^{WI} can be attributed to severe carbon formation, which has blocked the catalyst bed. The higher resistance to carbon deposition for the nanotubular multi–yolk–shell catalyst than impregnated catalyst might come from the strong metal–support interaction due to confinement effect.[72] Both lower conversion and yield measured under reducing condition (O/M = 1.0) than oxidizing condition (O/M = 1.1) can be explained by the side reactions (reactions (8–10) and (12)) which facilitate carbon deposition.[73] Most of the carbon can be deposited on the catalyst by methane cracking reaction (8) at 750 °C, leading to the increase in H_2/CO ratio.[61]

1.3.3 Characterization of spent catalysts

Figure 1.15a,b show the XRD spectra of the spent catalysts after TRM at the O/M feed ratio of 1.1 and 1.0, respectively. The XRD measurements performed on the spent catalysts after

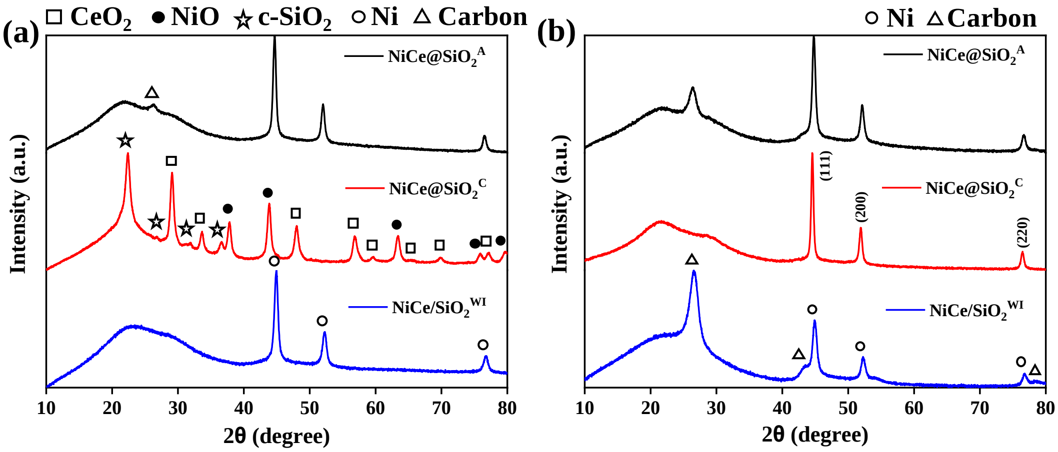

Figure 1.15. XRD patterns of spent NiCe@SiO_2^A, NiCe@SiO_2^C, and NiCe/SiO_2^{WI} after 20 h of TRM in O/M ratios of (a) 1.1 and (b) 1.0 feed stream at 750 °C.

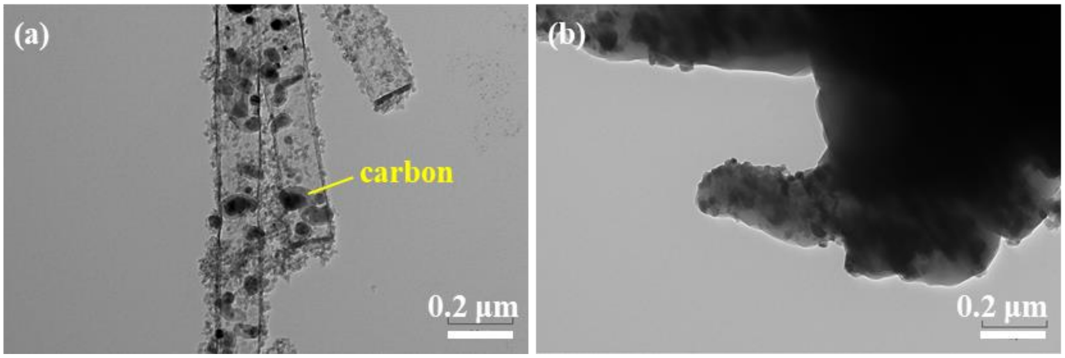

Figure 1.16. TEM images of spent (a) NiCe@SiO$_2$^{A} and (b) NiCe@SiO$_2$^{C} after 20 h of TRM in O/M ratio of 1.1 feed stream at 750 ºC.

the TRM at the O/M feed ratio of 1.1 indicate that the reduced metallic Ni (2θ = 44.7°, 52.0°, and 76.6°) and amorphous SiO$_2$ shell maintained its phase in the NiCe@SiO$_2$^{A} and NiCe/SiO$_2$^{WI} catalysts (Figure 1.15a). No CeO$_2$ peaks are observed on NiCe@SiO$_2$^{A} and NiCe/SiO$_2$^{WI} after the reaction because crystalline CeO$_2$ phase turned into the amorphous phase in the presence of H$_2$ at temperatures above 600 °C.[65,74,75] Despite the change of Ni and Ce phases during the reaction, the TEM image of the spent NiCe@SiO$_2$^{A} shows that the morphology of the nanotubular multi–yolk–shell is preserved without collapsing, as shown in Figure 1.16a. Further testing of NiCe@SiO$_2$^{A} at a higher O/M feed ratio of 1.25 also shows that higher oxidizer concentration in the feed stream does not influence the NiCe@SiO$_2$^{A} catalyst morphology (Figure 1.17). The mean yolk size of the spent catalyst (32.7 nm) is similar to the size of the fresh catalyst (32.9

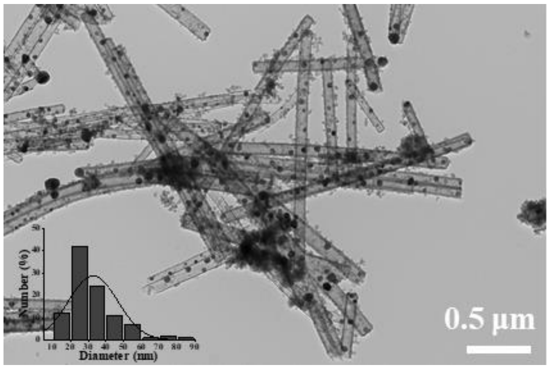

Figure 1.17. TEM image of spent NiCe@SiO$_2$^{A} after 20 h of TRM in O/M ratio of 1.25 feed stream at 750 ºC. Inset graph shows yolk size distribution.

nm). These results show that yolks are not likely to sinter during the reaction due to the strong interaction between the metal yolk and the silica shell.[76,77] However, in the case of NiCe@SiO_2^{C}, crystalline phases of NiO, CeO_2 and SiO_2 are observed for the spent catalyst due to re-oxidation at O/M ratio of 1.1 during the TRM (Figure 1.15a). The deactivation of NiCe@SiO_2^{C} is likely caused by oxidation of the active metallic Ni, followed by destruction of the nanotubular multi–yolk–shell structure (Figure 1.16b). Figure 1.18 shows the diffraction pattern of NiCe@SiO_2^{C} analyzed during the deactivation process. Both metallic Ni and Ni^{2+} phases are detected after 3 h of TRM, indicating that fully reduced Ni phase starts to be oxidized to the NiO phase at high O/M feed ratio, leading to the deactivation of the catalyst. It is important to note that a high amount of oxidizing species in the feed stream can still lead to the formation of carbon on the NiCe@SiO_2^{A} catalyst. As shown in the diffraction pattern of the spent NiCe@SiO_2^{A} (Figure 1.15a), carbon is detected at a 2θ of 26.6°.[23,24] The carbon deposition can also be observed in the TEM image of the spent catalyst (Figure 1.16a). Our results suggest that carbon deposition on the spent NiCe@SiO_2^{A} is not high enough to affect the stability of the catalyst.

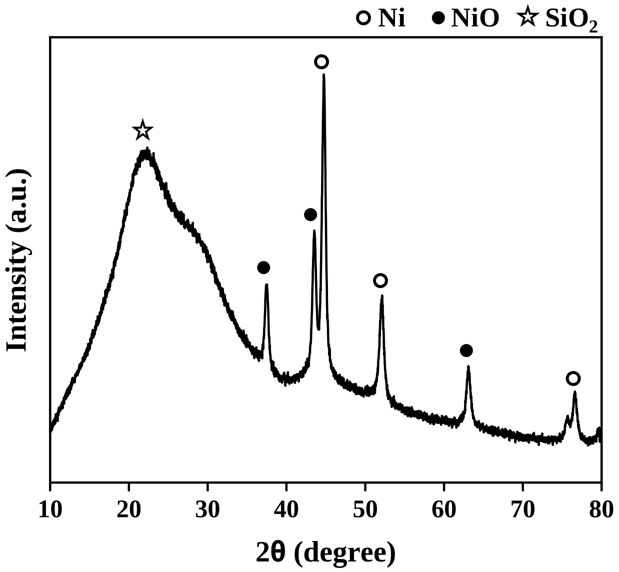

Figure 1.18. XRD pattern of NiCe@SiO_2^{C} during the deactivation process at O/M ratio of 1.1 at 750 °C.

The XRD spectra of the spent catalysts after TRM at the O/M feed ratio of 1.0 show that all three catalysts have metallic Ni peaks along with wide amorphous SiO_2 peak, as shown in Figure 1.15b. Similarly, CeO_2 turns to the amorphous phase and its diffraction peaks are not observed on all three spent catalysts after the reaction. The spent NiCe/SiO_2^{WI} catalyst has much stronger intensity for carbon peak at 26.6° than NiCe@SiO_2^{A}, while no carbon peak is detected for NiCe@SiO_2^{C} after 20 h of the TRM reaction. These results suggest that the nanotubular multi–yolk–shell catalyst with smaller yolks presents high resistance to carbon deposition providing longer stability for TRM at the O/M feed ratio of 1.0. Raman spectra of the spent NiCe@SiO_2^{A}, NiCe@SiO_2^{C}, and NiCe/SiO_2^{WI} catalysts after the reaction at O/M feed ratio of 1.0 were collected to determine the nature of carbon formed on the spent catalyst. As shown in Figure 1.19a, both the spent NiCe@SiO_2^{A} and NiCe/SiO_2^{WI} catalysts have carbon formations, in agreement with the XRD measurement, while carbon peaks are barely seen for NiCe@SiO_2^{C} after 20 h of TRM. The two bands observed at 1331.8 cm^{-1} and 1581.9 cm^{-1} on the spent NiCe@SiO_2^{A} and NiCe/SiO_2^{WI} catalysts can be ascribed to carbon sp^2 bonds in which the first peak is assigned to the D band with defects or amorphous carbon, while the second peak belongs

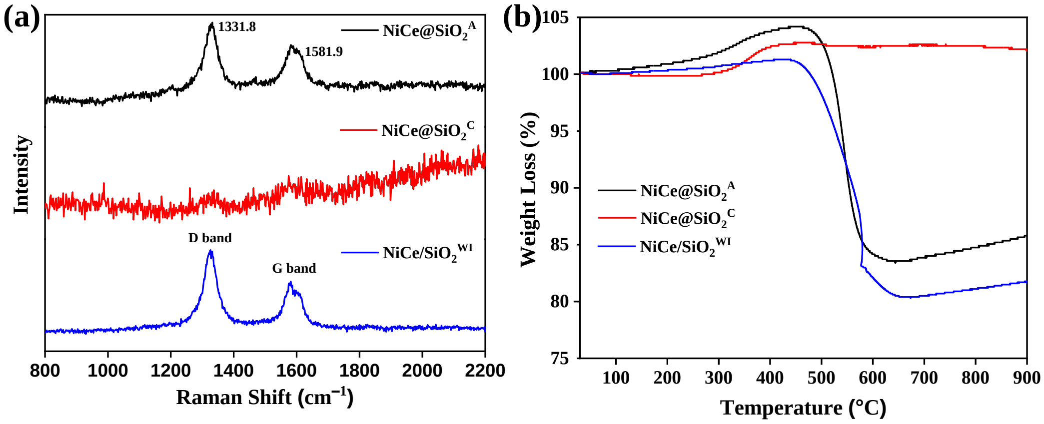

Figure 1.19. (a) Raman spectra and (b) TGA profiles of spent NiCe@SiO_2^{A}, NiCe@SiO_2^{C}, and NiCe/SiO_2^{WI} after the TRM reaction in O/M ratio of 1.0 feed stream at 750 °C.

to the G band with ordered graphite structure [52]. TGA was performed to quantify the amount of carbon deposited on the spent catalysts after the reaction. As shown in Figure 1.19b, the weight of the spent nanotubular multi–yolk–shell catalysts slightly increases starting from 260 °C due to oxidation of the catalyst. The sample weight loss occurs at temperatures between 450 °C and 650 °C for NiCe@SiO_2^A and NiCe/SiO_2^{WI} due to the gasification of the carbon formed during the TRM reaction. The deposited carbon amount is calculated to be 0.16 mg g_{cat}^{-1} and 0.20 mg g_{cat}^{-1} for NiCe@SiO_2^A and NiCe/SiO_2^{WI}, respectively. In consistent with the XRD and Raman analysis, the weight of NiCe@SiO_2^C remains constant at temperatures between 450 °C and 900 °C, indicating that carbon species are not likely to form on the catalyst during 20 h of TRM. The high resistance to carbon deposition of nanotubular NiCe@SiO_2 multi–yolk–shell catalysts can be possibly due to the strong binding of active Ni species to SiO_2, as illustrated in the H_2-TPR data. It is also possible that the unique morphology of the nanotubular multi–yolk–shell structures does not allow carbon to be deposited on the active sites due to the confinement effect. Despite the unique morphology of the nanotubular multi–yolk–shell catalysts, the XRD, Raman, and TGA results confirm that carbon can still form on larger yolks (NiCe@SiO_2^A), while smaller yolks (NiCe@SiO_2^C) exhibit higher resistance to carbon deposition at the O/M ratio of 1.0 feed stream.

1.3.4 Effect of yolk size under reducing conditions

To understand the effect of yolk size on TRM activity, NiCe@SiO_2^B with a mean yolk size between NiCe@SiO_2^A and NiCe@SiO_2^C was synthesized, and three nanotubular multi–yolk–shell catalysts were evaluated at much higher methane concentration with an O/M feed ratio of 0.85. As shown in Figure 1.20, NiCe@SiO_2^C with a mean yolk size of 20.0 nm still presents a stable activity with CO_2 and CH_4 conversions of 73% and 61%, respectively.

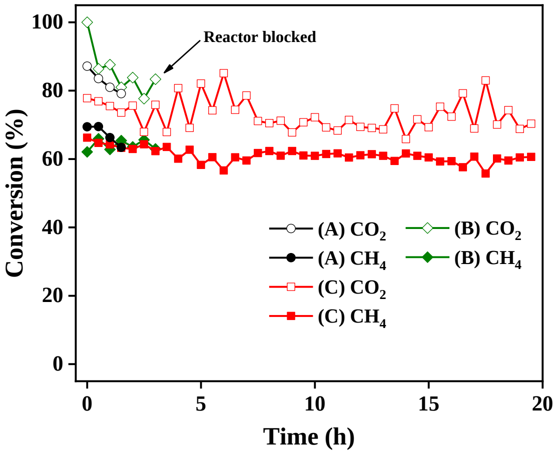

Figure 1.20. CO_2 and CH_4 conversions of (A) NiCe@SiO_2^A, (B) NiCe@SiO_2^B, and (C) NiCe@SiO_2^C in O/M ratio of 0.85 feed stream at 750 °C.

However, the NiCe@SiO_2^A catalyst with the largest yolks deactivates within 2 h by carbon formation. NiCe@SiO_2^B with a mean yolk size of 23.7 nm shows slightly longer stability than NiCe@SiO_2^A, but the catalyst also loses its activity in 4 h due to the blockage of the catalyst bed by carbon formation. As shown in Figure 1.21, carbon peaks in XRD are detected for both of the

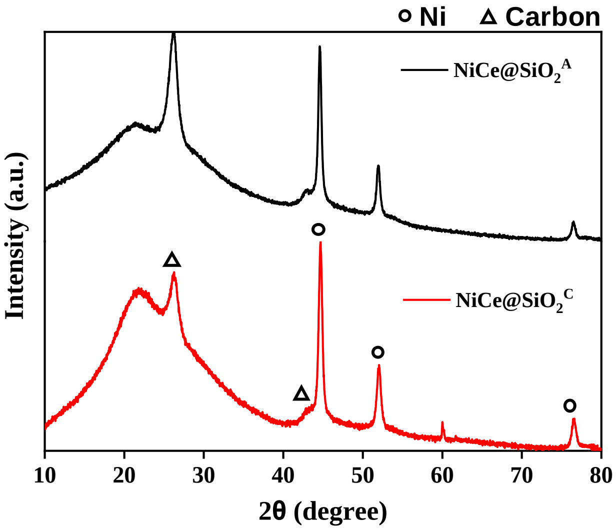

Figure 1.21. XRD patterns of spent NiCe@SiO_2^A and NiCe@SiO_2^C after TRM reaction in O/M ratio of 0.85 feed stream at 750 °C.

spent NiCe@SiO$_2^A$ and NiCe@SiO$_2^C$ catalysts, but NiCe@SiO$_2^A$ with larger yolks have stronger carbon peak intensity than NiCe@SiO$_2^C$ with smaller yolks after the reaction with the O/M feed ratio of 0.85. Throughout the three nanotubular multi–yolk–shell catalysts tested, NiCe@SiO$_2^C$ exhibits the most stable activity at both O/M ratio of 1.0 and 0.85 due to the fast carbon removal reaction, whereas the other catalysts with mean yolk size larger than 20.0 nm (NiCe@SiO$_2^A$ and NiCe@SiO$_2^B$) deactivate at high CH_4 concentration feed streams.

$$CH_4 \rightarrow C + 2H_2 \qquad \Delta H^o = +74.9\ kJ\cdot mol^{-1} \qquad (1.8)$$

$$CO + H_2 \leftrightarrow C + H_2O \qquad \Delta H^o = -131.3\ kJ\cdot mol^{-1} \qquad (1.9)$$

$$2CO \leftrightarrow C + CO_2 \qquad \Delta H^o = -172.5\ kJ\cdot mol^{-1} \qquad (1.10)$$

$$C + O_2 \rightarrow CO_2 \qquad \Delta H^o = -394\ kJ\cdot mol^{-1} \qquad (1.11)$$

$$2CeO_2 + C \leftrightarrow Ce_2O_3 + CO \qquad (1.12)$$

$$2CeO_2 + Ni \leftrightarrow Ce_2O_3 + NiO \qquad (1.13)$$

During the TRM reaction, carbon formation can occur via the following reactions: methane cracking (1.8), reduction of CO (1.9), and the Boudouard reaction (1.10). At the same time, the deposited carbon can be removed by the reverse reactions of (1.9) and (1.10), and the forward reaction of (1.11), in which carbon reacts with H_2O, CO_2 and O_2, respectively. While these reactions occur simultaneously on the catalyst, carbon formation and removal reaction rates can be influenced by the Ni particle size. Different Ni particle sizes ranging in between 6 nm and 26 nm have been reported for the net formation of carbon on Ni-based catalyst.[78–80] It has been shown that the removal rate of carbon is faster than the formation rate of carbon on catalysts containing smaller Ni particles, indicating that large Ni particles are more susceptible to carbon formation.[79,81] In particular, the carbon formation rate in SRM is found to be directly related to the Ni particle size with smaller Ni particles resulting in a lower coking rate due to the low driving force for carbon diffusion through the Ni.[82] In addition to the carbon formation rates, smaller Ni particles are shown to yield carbon filaments with smaller diameters in DRM compared to filaments formed on larger Ni particles.[83] Growth of smaller diameter carbon filaments is not thermodynamically favorable, resulting in less carbon deposition compared to larger diameter carbon filaments. Carbon filament growth can be related to the equilibrium Gibbs free energy growth of graphite. Deviations from graphite's equilibrium Gibbs free energy are inversely proportional to particle diameter. The deviations from the graphite equilibrium value represent extra energy needed by the system to form filamentous carbon, therefore smaller Ni particles lead to larger deviations resulting in less carbon filament growth.[84] In POM, smaller Ni particles result in the formation of more hydrogen containing carbon species than graphitic or nanotube structure carbon.[85] Carbon species containing hydrogen are easily gasified and therefore do not cause catalyst deactivation, meaning that smaller particles are not as easily deactivated by carbon as larger particles. It stands to reason that the catalyst containing smaller yolks might form less and more easily removable carbon than the catalyst containing larger yolks. However, no distinctive conclusion can be made in terms of what Ni particle size is more beneficial to prevent carbon formation, as it highly depends on the chemistry and morphology of the catalyst. In addition to the Ni yolk size, Ni–Ce interaction can play a major role on the stability of the catalyst. Under reducing conditions i.e., O/M feed ratios of 0.85 and 1.0, NiCe@SiO_2^C has high resistance to carbon deposition possibly due to the high amount of Ce^{4+} concentration. The first step in methane reforming reactions is believed to start with CH_4 dissociation to generate hydrocarbon species and carbon atoms.[86] Carbon atoms can be oxidized by reacting with CO_2 (reaction (1.10)) and Ce^{4+} (reaction (1.12)). The reverse reaction of (1.12) could be observed for the $NiCe@SiO_2^{A}$ and $NiCe/SiO_2^{Imp}$ catalysts as they have high Ce^{3+} concentration, thereby can produce more carbon deposits compared to $NiCe@SiO_2^{C}$.[86]

1.3.5 Effect of yolk size under oxidizing conditions

The active metallic Ni phase in small yolks can be re-oxidized by adsorbing oxygen species from the feed gases or interaction with CeO_2 at O/M feed ratios higher than 1.0. Large Ni yolks can have slower carbon removal rate leading to carbon deposition even at higher O/M ratios feed stream, as shown in Figure 1.15a and Figure 1.16a. However, it has been hypothesized that the carbon formation on large Ni particles can prevent Ni metal from being oxidized in the high oxygen-containing feed stream (O/M ratio > 1.0).[87] On the other hand, carbon formation rate is slower than the carbon oxidation rate on the small yolks ($NiCe@SiO_2^{C}$), therefore, the amount of deposited carbon may not be sufficient enough to prevent the oxidation of metallic Ni to NiO, leading to deactivation of the catalyst. In contrast to the nanotubular $NiCe@SiO_2$ multi–yolk–shell catalyst, the conventional $NiCe/SiO_2^{WI}$ catalyst exhibits stable activity without both Ni oxidation and carbon formation confirmed by XRD at the O/M feed ratio of 1.1 (Figure 1.15a). This can be explained by the fact that $NiCe/SiO_2^{WI}$ has stronger interaction between dispersed Ni and Ce species confirmed by H_2-TPR and XPS. The Ce^{3+}/Ce^{4+} redox property on CeO_2 provides high surface and bulk oxygen vacancies.[38] Therefore, it is possible that the oxygen species migrate to the oxygen vacancies on CeO_2, which hinders Ni species from being oxidized. The stable activity of $NiCe@SiO_2^{A}$ and $NiCe/SiO_2^{WI}$ at O/M ratio of 1.1 can also be explained by Ce effect as aggregated Ni yolks and dispersed Ni particles in interaction with Ce lead to the formation of more Ce^{3+} species evidenced by H_2-TPR and XPS. Availability of Ce^{3+} and Ce^{4+} species can shift the equilibrium of the reaction (1.13) and facilitate Ni oxidation [86]. Both NiCe@SiO_2^A and NiCe/SiO_2^{WI} have higher Ce^{3+} concentration compared to NiCe@SiO_2^C and show stable activity without Ni oxidation. On the contrary, the forward reaction of (1.13) can be observed for the NiCe@SiO_2^C as it has high Ce^{4+} concentration, thereby can oxidize active Ni yolks.

In summary, our results indicate that carbon formation and removal rates need to be balanced to obtain stable performance under the TRM by controlling the Ni yolk size and Ni–Ce interaction. If the carbon formation is faster than carbon removal process, the carbon will deposit onto the catalyst, whereas if the carbon removal reaction rate is faster than carbon formation rate, the metallic Ni species can be oxidized to NiO by exposing to oxygen species, which both cases can deactivate the catalyst.[88,89] While the effect of yolk size and Ce effect on the TRM activity can be pronounced, other structural parameters, such as shell thickness and tube diameter of the nanotubular multi–yolk–shell catalysts, should be systematically analyzed in future studies.

1.4 Conclusions

Different morphologies of nanotubular NiCe@SiO_2 multi–yolk–shell catalysts were synthesized by controlling the water to surfactant ratio in the reverse microemulsion method. The nanotubular multi–yolk–shell catalyst prepared at the high water/surfactant ratio forms smaller yolks surrounded by a longer diameter silica tube shell, whereas a low water/surfactant ratio produces larger yolks with a shorter diameter tube shell. Catalysts prepared with small and large yolks show distinct characteristic behavior at various feed gas ratios under TRM. At a low O/M feed ratio, the nanotubular NiCe@SiO_2 multi–yolk–shell catalysts exhibit higher resistance to carbon deposition due to its confinement effect. In contrast, the conventional impregnated

$NiCe/SiO_2^{WI}$ catalyst produces a high amount of carbon deposition on the catalyst, which deactivates the catalyst fast. The nanotubular $NiCe@SiO_2$ multi–yolk–shell catalyst with smaller yolks forms less carbon compared to the catalyst with larger yolk sizes (> 20 nm) possibly due to the facile oxidation of carbon on the smaller Ni yolks and low Ce^{3+} concentration. On the other hand, at a high O/M feed ratio, the $NiCe@SiO_2$ catalyst containing smaller yolks tends to be easily re-oxidized by oxygen species leading to the catalyst deactivation followed by destruction of nanotubular multi–yolk–shell morphology. However, the $NiCe@SiO_2$ with larger yolks shows stable activity without oxidation possibly due to the slower carbon removal reaction rate and high Ce^{3+} concentration. Our results show that the morphology of the nanotubular $NiCe@SiO_2$ multi–yolk–shell catalysts will influence the TRM activity at different O/M feed ratios, and this tunable morphology can be engineered for obtaining high TRM activity and stability.

CHAPTER 2

Yolk–Shell Single-Atom Alloy Catalysts for Low-Temperature Dry Reforming of Methane

2.1 Introduction

One engineering approach to reduce CO_2 emissions is to develop chemical processes for the synthesis of value-added chemicals or liquid fuels directly from the CO_2 source. Dry reforming of methane (DRM, $CH_4 + CO_2 \rightarrow 2CO + 2H_2$, $\Delta H^o = +247.3$ kJ mol^{-1}) is considered as a promising reaction to utilize streams with a high content of CO_2 from ammonia plants, oxy-fuel combustion, or biogas generated from anaerobic digestion of sewage, sludge, and landfill.[90,91] DRM can convert CO_2 and CH_4 to syngas, which can be converted further to high value-added products, such as C_{2+} hydrocarbons and oxygenated chemicals, while avoiding costly CO_2 and CH_4 separation in the biogas stream.[9]

DRM has strong endothermicity and requires high operating cost and energy. Therefore, developing a catalyst with high DRM activity and stability at relatively low reaction temperatures (e.g., 500 °C) is of interest.[47,92,93] To date, Ni-based catalysts have been extensively studied for DRM due to their high activity and low cost compared to the noble metals.[93–95] Despite their high activity, carbon formation and/or metal sintering can reduce the stability of Ni-based catalysts leading to fast deactivation.[96–98] Particularly, the carbon formation rate is substantially enhanced on the catalyst through the favorable Boudouard reaction ($2CO \leftrightarrow C + CO_2$, $\Delta H^\circ = -171.5$ kJ mol^{-1}) at low reaction temperatures under DRM.[47] Further research is required to stabilize the active Ni metal and minimize the effect of the Boudouard reaction at low reaction temperatures. Our recent work has shown that nanotubular NiCe@SiO_2 multi–yolk–

shell catalysts can maintain a stable catalytic activity and decrease carbon deposition at 750 °C under tri-reforming of methane (TRM).[99] The confined morphology of NiCe@SiO_2 provides strong interaction between active Ni and SiO_2 support, which can improve the catalytic activity and provide high resistance to carbon deposition compared to conventional catalysts synthesized by wet impregnation. The confined morphology of core/yolk–shell have shown to have high resistance to coking and sintering during methane reforming due to the confinement effect and strong metal–support interaction.[59,100–102] The addition of CeO_2 to the Ni-based catalysts can enhance the Ni dispersion and decrease carbon content on the catalyst due to its oxygen vacancies and reversible redox property.[36,38,99]

Unlike TRM, DRM does not involve oxidizing reactants, i.e. H_2O and O_2, which can facilitate carbon removal during the reaction. Therefore, it is challenging to prevent deactivation of Ni species, specifically at low DRM reaction temperatures without carbon accumulation. Dopants added to the Ni-based catalyst has shown promising activity and stability under DRM conditions. A suitable dopant should have a moderate adsorption energy for carbon to improve the carbon resistance as well as low dissociation barriers for CH_4 and CO_2 activation to obtain a high DRM activity.[103] Several studies have shown that adding a small amount of Pt to Ni-based catalysts can increase the activity and stability of the catalysts for DRM.[92,104–106] Pt can improve the metal dispersion on the support and reducibility of Ni species due to H_2 spillover effect.[92,104,105] Formation of Pt–Ni alloy can produce reactive carbonaceous species, which can be removed more efficiently compared to monometallic Ni.[107] Promotion of Ni catalysts with low Pt concentrations can lead to the formation of single-site catalysts (SSCs), including single-atom catalysts (SACs), and single-atom alloys (SAAs) with unique electronic and geometric structures.[108–110] Compared to the catalysts with nanoparticles, SSCs has isolated metals, which can enhance metal–support interaction providing good thermal stability in catalytic reactions and lower the activation barrier by shifting the reaction pathway.[111–114]

In the present work, we report the DRM performance of the carbon-resistant nanotubular yolk–shell Pt-NiCe@SiO_2 SAA catalyst at 500 °C. Effects of the confined morphology and Pt promotion are investigated to overcome the challenges associated with catalyst deactivation. The activity and stability of the yolk–shell catalysts are compared with the conventional catalysts synthesized by wet impregnation to elucidate the structural differences. Our results show that a 0.25 wt% of Pt-promoted yolk–shell SAA catalyst ($Pt^{0.25}$-NiCe@SiO_2) exhibits excellent resistance to carbon deposition for DRM. The improved performance of $Pt^{0.25}$-NiCe@SiO_2 is attributed to the atomically dispersed Pt on the yolks with the formation of Pt–Ni SAA in the confined nanotubular SiO_2 structure.

2.2 Experimental Methods

2.2.1 Catalyst preparation

The yolk–shell catalysts were synthesized by a reverse microemulsion method. The solution containing 0.0006–0.006 M of platinum tetrachloride ($PtCl_4$, 99.9%, Sigma Aldrich), 0.2 M of nickel nitrate hexahydrate ($Ni(NO_3)_2{\cdot}6H_2O$, 98%, Alfa Aesar), and 0.05 M of cerium nitrate hexahydrate ($Ce(NO_3)_3{\cdot}6H_2O$, 99%, Sigma Aldrich) in 4 ml of deionized (DI) water as yolk precursors was added dropwise to the microemulsion of 0.17 M of 1-hexadecyl trimethyl ammonium bromide (CTAB) ($CH_3(CH_2)_{15}N(CH_3)_3Br$, 98%, Alfa Aesar) dissolved in a 15 ml of 1-butanol ($CH_3(CH_2)_3OH$, anhydrous, 99.8%, Sigma Aldrich) and 80 ml of cyclohexane (C_6H_{12}, 99%, Alfa Aesar) mixture. After stirring the solution for 1 h, the transparent microemulsion solution was heated to 70 °C in an oil bath, and 0.7 ml of hydrazine (N_2H_4, anhydrous, 98%, Sigma Aldrich) as a reducing agent with 0.5 M of sodium hydroxide (NaOH, Fisher Chemical) in 1.5 ml DI was added to the solution dropwise, followed by further stirring for 40 min. The solution was cooled down to room temperature and aged for another 2 h under stirring. Finally, 1.5 ml of tetraethyl orthosilicate (TEOS) ($Si(OC_2H_5)_4$, 99% Sigma Aldrich) as a silica shell precursor and 1.5 ml of ammonium hydroxide solution (NH_4OH, 28% NH_3, Alfa Aesar) were added to the solution dropwise. The final solution was aged for 20 h for hydrolysis and condensation of the silica precursor. The solution was washed with ethanol (C_2H_6O, anhydrous, Fisher Chemical) and separated by centrifuging. The washed sample was dried at 100 °C overnight and calcined in static air at 500 °C for 4 h with a ramping rate of 5 °C min^{-1}. Pt^x-$NiCe@SiO_2$ (where x = 0.1, 0.25, 0.5, and 1 corresponding to the wt% of Pt) was synthesized by controlling the $PtCl_4$ concentration, while the weight percentages of Ni and Ce were fixed at 9.23 wt% and 5.82 wt%, respectively. A conventional Pt^x-$NiCe/SiO_2^{WI}$ catalyst was synthesized by the wet impregnation method. Fumed silica (SiO_2, Sigma Aldrich) was added to the aqueous solution of $PtCl_4$, $Ni(NO_3)_2\cdot 6H_2O$, and $Ce(NO_3)_3\cdot 6H_2O$ with the same weight percentages of Pt, Ni, and Ce as the yolk–shell catalysts. The mixture was stirred for 15 h at 70 °C. The sample was dried at 100 °C overnight and calcined in static air at 500 °C for 4 h with a ramping rate of 5 °C min^{-1}.

2.2.2 Characterization

Transmission electron microscopy (TEM) images were obtained using Hitachi H8000. High-resolution TEM (HRTEM) and aberration-corrected high-angle annular dark field scanning TEM (AC-HAADF-STEM) images with energy dispersive X-ray spectroscopy (EDX) were collected using JEOL Grand ARM. The samples were ultrasonically dispersed in ethanol and loaded on a carbon-coated Cu grid. The particle size distribution of yolks was calculated using 100 yolk particles and normalized by the total of measurements to obtain the fraction. The total metal loading (wt%) of the samples was analyzed by inductively coupled plasma optical emission spectroscopy (ICP-OES, PerkinElmer Avio 200) after dissolving the samples completely in a mixture of hydrochloric acid and nitric acid. Powder X-ray diffraction (XRD) patterns were recorded with Rigaku MiniFlex II using Cu Kα source radiation ($\lambda = 1.5406$ Å) in a 2θ range of 10°–80° with a step rate of 2° min^{-1}, and the crystallite size of the samples was calculated by the Scherrer equation. X-ray photoelectron spectroscopy (XPS) was conducted on a Kratos Axis Ultra DLD using Al K_α radiation. The spectra were obtained after the catalysts were reduced in H_2 at 500 °C for 1 h, followed by Ar^+ etching for 9 min to analyze yolks inside the SiO_2 shell. The binding energy was calibrated to the signal of C 1s at 284.8 eV. N_2 adsorption and desorption isotherms were collected by Micromeritics ASAP 2020 at −196 °C. Prior to the measurements, the samples were degassed at 300 °C for 7 h. Hydrogen temperature-programmed reduction (H_2-TPR) was performed on Micromeritics AutoChem II equipped with a thermal conductivity detector (TCD). First, 50 mg of catalyst was heated at 300 °C for 1 h under He flow to eliminate any moisture and contamination, and then cooled down to 30 °C. After this preparation step, the temperature was ramped from 30 °C to 900 °C at a rate of 10 °C min^{-1} in a 10% H_2/Ar mixture. H_2 chemisorption experiments were performed on the same Micromeritics AutoChem II to determine Ni dispersion. 100 mg of catalyst was reduced in a 10% H_2/Ar mixture at 500 °C for 3 h, and then the catalyst was purged at 500 °C for 1 h under He. H_2 pulse chemisorption was carried out at 35 °C in 10% H_2/Ar with 8 min intervals. The active Ni sites were obtained from the adsorbed H_2 volume by assuming the H/Ni stoichiometry of 1. Thermogravimetric analysis (TGA) was employed on TGA-50 Shimadzu to determine carbon deposition on the spent catalyst. The samples were heated from 30 °C to 900 °C with a ramping temperature of 10 °C min^{-1} under airflow. The nature of carbon deposited on the spent catalyst was determined by Raman spectroscopy using XploRA PLUS, Horiba in the backscattering configuration using 638 nm wavelength. The time-resolved *in situ* and *operando* diffuse reflectance infrared Fourier transform spectroscopy (DRIFTS) experiments were performed on Bruker infrared spectrometer (VERTEX 70) using the Harrick Praying Mantis DRIFTS gas cell equipped with ZnSe windows and mercury cadmium telluride (MCT) detector. Prior to the tests, catalysts were reduced at 500 °C in 25% H_2/N_2 mixture for 1 h and purged with N_2 for an additional 1 h at 500 °C. CO_2 injection experiments (CO_2:N_2=1:6) were performed on the reduced catalyst for 20 min followed by N_2 purge for 1 h at 500 °C. After N_2 purge, CH_4 (CH_4:N_2=1:6) was fed to the cell for 20 min. The DRM experiments were performed with a reactant mixture of CO_2:CH_4:N_2=1:1:6 on the reduced catalysts at 500 °C for 15 min. The background spectra were collected after the H_2 reduction. The background and sample spectra were collected 64 scans with a resolution of 4 cm^{-1}. The X-ray absorption spectroscopy (XAS) measurements of the samples at Pt L_3-edge, Ni K-edge, and Ce L_3-edge were conducted at the 10-BM beamline of the Advanced Photon Source (APS), Argonne National Laboratory. The fluorescence yield mode of the samples was collected using a 4 element Vortex detector. Pt metal foil and Ni metal foil were analyzed in transmission mode as a reference and for monochromatic energy calibration. The extended X-ray absorption fine structure (EXAFS) data at Pt L_3-edge was weighted by k^2 to gain the magnitude plots in radial space fitted by Artemis software.[115] Fourier transformation was performed over the k-range of 3–10 Å^{-1}, and the amplitude reduction factor was set to 0.76 calculated from the Pt foil.

2.2.3 DRM activity

The DRM performance of the catalyst was tested in a fixed-bed reactor at atmospheric pressure. The prepared catalysts were pressed, crushed, and sieved to granules in the range of 40–60 mesh (250–420 μm). The catalyst (75 mg) was placed between quartz wool in a quartz reactor with an inner diameter of 7 mm. The reactor was placed in a furnace and the temperature of the catalyst was measured by a K-type thermocouple placed inside the catalyst bed. The reaction gases were introduced to the reactor via mass flow controllers. The effluent gases were passed through a condenser in which any residual water was removed, and their concentration was measured with a gas chromatograph (GC) using a TCD. Prior to the reaction, all catalysts were reduced at 500 °C for 3 h with 25% H_2 balanced with N_2. Following the reduction, the DRM activity and stability of the catalysts were evaluated at 500 °C under atmospheric pressure in a reaction stream of CO_2:CH_4:N_2=1:1:1 for 20 h time-on-stream (TOS). All activity and kinetic studies were conducted at a gas hourly space velocity (GHSV) of 60,000 ml g^{-1} h^{-1}, and the catalytic activity was calculated using the following equations:

$$\text{Conversion, X (\%)} = \frac{F_{\text{react,in}} - F_{\text{react,out}}}{F_{\text{react,in}}} \times 100 \qquad (2.1)$$

$$H_2 \text{ yield (\%)} = \frac{F_{\text{H2,out}}}{2F_{\text{CH4,in}}} \times 100 \qquad (2.2)$$

$$\text{CO yield (\%)} = \frac{F_{\text{CO,out}}}{F_{\text{CO2,in}} + F_{\text{CH4,in}}} \times 100 \qquad (2.3)$$

$$H_2/\text{CO ratio} = \frac{F_{\text{H2,out}}}{F_{\text{CO,out}}} \qquad (2.4)$$

$$\text{Conversion rate (mmol } g_{\text{Ni+Pt}}^{-1}\, s^{-1}) = \frac{\text{GHSV} \cdot F_{\text{react,in}} \cdot X_{\text{react}}}{W_{\text{Ni+Pt}}} \qquad (2.5)$$

where F represents the mole fractions of the reagent species measured at the inlet or outlet of the reactor, and $W_{\text{Ni+Pt}}$ denotes the sum of the Ni and Pt metal loadings. In all experiments, the carbon balance was close to 100%, and the reproducibility of the catalytic activity is within ±5%.

2.3 Results

2.3.1 Catalysts characterization

Figure 2.1a shows the TEM image of the reduced nanotubular yolk–shell $Pt^{0.25}$-NiCe@SiO_2 SAA catalyst prepared by the reverse microemulsion synthesis. The yolks are well distributed inside the nanotubular SiO_2 shell with an average cavity diameter of 106.5 nm and a wall thickness of 6.6 nm. The average length of the nanotubular SiO_2 is as high as 1.7 µm, and the yolk sizes inside the SiO_2 support vary from 5 nm to 65 nm with an average size of 20.5 nm. High-resolution AC-HAADF-STEM images of the reduced yolks reveal that Pt is atomically dispersed on the yolks (Figure 2.1b and Figure 2.2). The isolated Pt atoms are presented as bright dots (some of them are highlighted by yellow circles) with higher contrast than the surrounding Ni and CeO_2 lattice, confirming the SAA structure. The HRTEM images in Figure 2.1c,d show the lattice fringes with interplanar spacings of 0.20 nm and 0.18 nm corresponding to the Ni

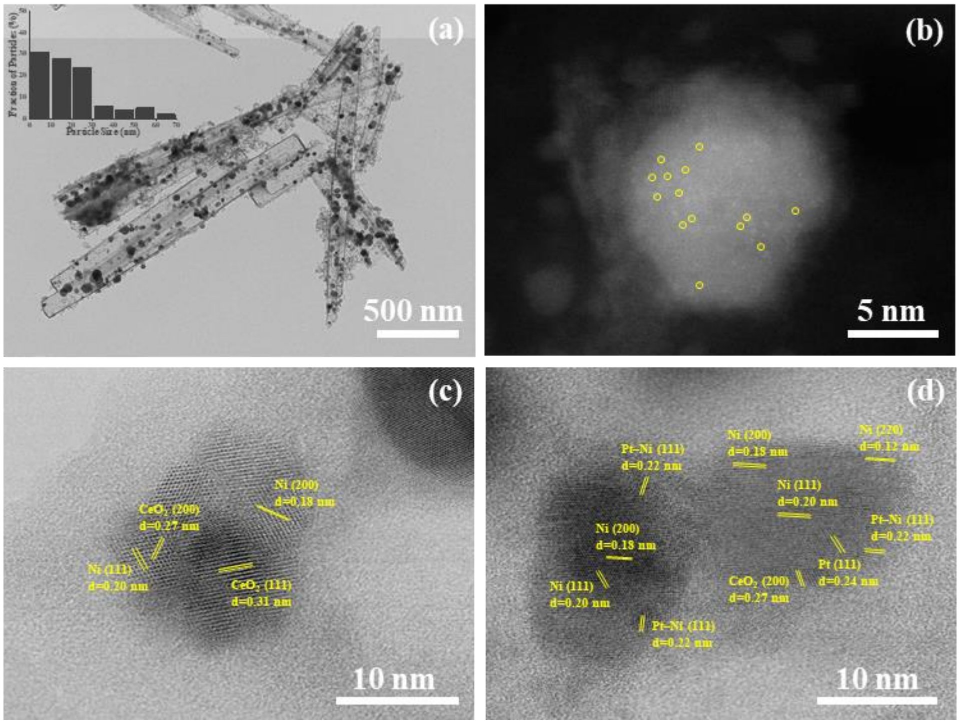

Figure 2.1. (a) TEM (b) HAADF-STEM, and (c,d) HRTEM images of reduced nanotubular yolk–shell $Pt^{0.25}$-NiCe@SiO_2 SAA catalyst.

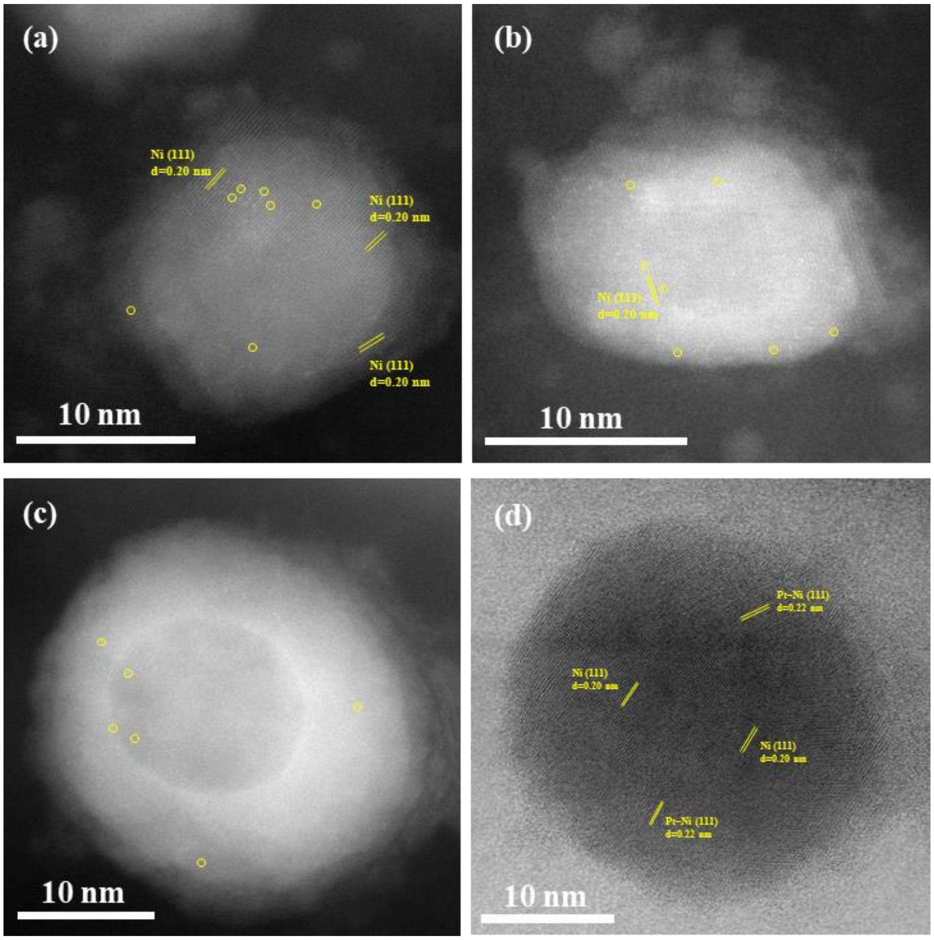

Figure 2.2. (a–c) HAADF-STEM and (d) HRTEM images of reduced Pt$^{0.25}$-NiCe@SiO$_2$ SAA catalyst.

(111) and Ni (200) planes, respectively. Next to the Ni lattice fringes, CeO$_2$ (111) and CeO$_2$ (200) planes are observable with interplanar spacings of 0.31 nm and 0.27 nm, respectively, indicating a possible Ni–CeO$_2$ interaction (Figure 2.1c). In addition, the lattice fringe of 0.22 nm shown in Figure 2.1d and Figure 2.2d) can be associated with the (111) plane of a Pt–Ni alloy.[116–118] The Pt–Ni alloys are observed mostly at the edges of the yolks rather than the core. It is possible that Pt-terminated supported Pt–Ni catalysts are thermodynamically stable under a reducing environment, where the reduced particles can form a core–shell type structure with Pt–rich shell.[119] Generally, Pt–Ni alloys can form thermodynamically by controlling the precipitation rate and concentration of precursor during the microemulsion synthesis. Pt has low

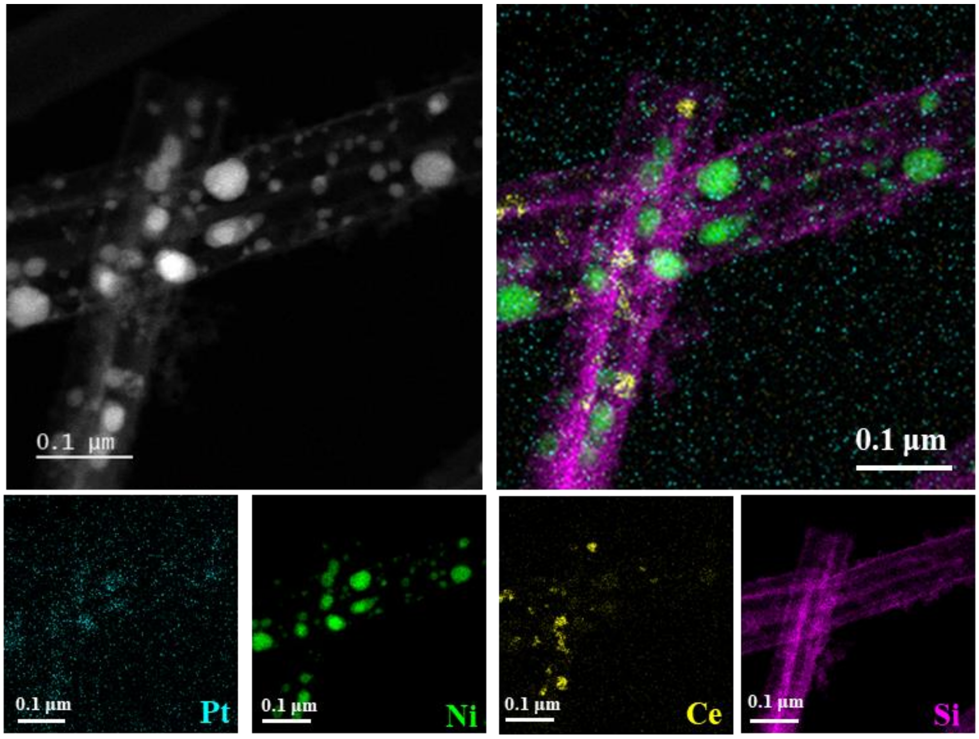

Figure 2.3. EDX elemental mapping images of reduced $Pt^{0.25}$-NiCe@SiO_2 (Pt: cyan, Ni: green, Ce: yellow, Si: magenta).

surface energy and can segregate to the surface when alloyed with Ni.[120] At low Pt loadings, the slow reduction rate of Pt can lead Pt to deposit on the Ni surface. However, the increase in the Pt precursor concentration can accelerate the reduction rate, resulting in a higher degree of Pt–Ni mixture in the core with Pt enriched nanoparticles.[121] In addition to the Pt–Ni interaction, Pt–CeO_2 interaction can be observed in Figure 2.1d. The lattice fringe size of 0.24 nm, which is slightly larger than 0.23 nm of Pt (111), can be observed near CeO_2 (200) planes. This result can be attributed to the Pt lattice expansion due to the interaction with CeO_2 species[122,123] or assigned to the Pt−Ce alloy formations, yet they are not identified in our XRD analysis. As shown in Figure 2.2, the formation of voids in the yolks can be seen due to the possible restructuring that occurred from oxygen loss under H_2 reduction.[124] Elemental mapping and EDX spectrum of the reduced $Pt^{0.25}$-NiCe@SiO_2 are shown in Figure 2.3 and Figure 2.4. The images confirm that the yolks are composed of Pt, Ni, and Ce species surrounded by the nanotubular SiO_2 shell. It is

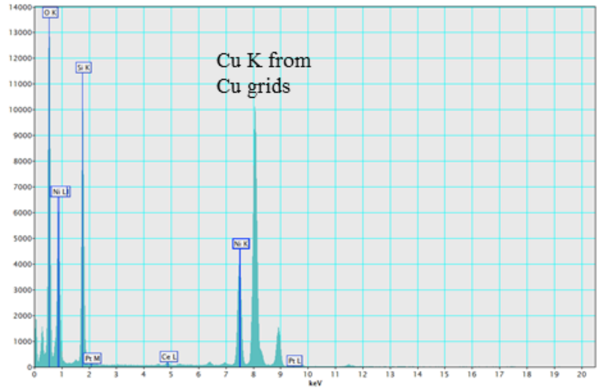

Figure 2.4. EDX spectrum for reduced $Pt^{0.25}$-NiCe@SiO_2.

important to note that Pt pixels are mostly observed on the yolks, yet they can also be detected outside of the shell at 0.25 wt% of Pt loading due to the low characteristic X-ray signals detected for Pt.

Lastly, the reduced $Pt^{0.25}$-NiCe/SiO_2^{WI} catalyst synthesized by wet impregnation is analyzed by HRTEM (Figure 2.5). Pt species are mostly distributed as Pt nanoclusters (some of them are highlighted by yellow circles) with an average size of 0.746 nm on both Ni and Ce species. As shown in Figure 2.6, the elemental mapping images of the same particle depicts that the nanoparticle located at the center is composed of Ni and Ce species. The EDX image of Pt

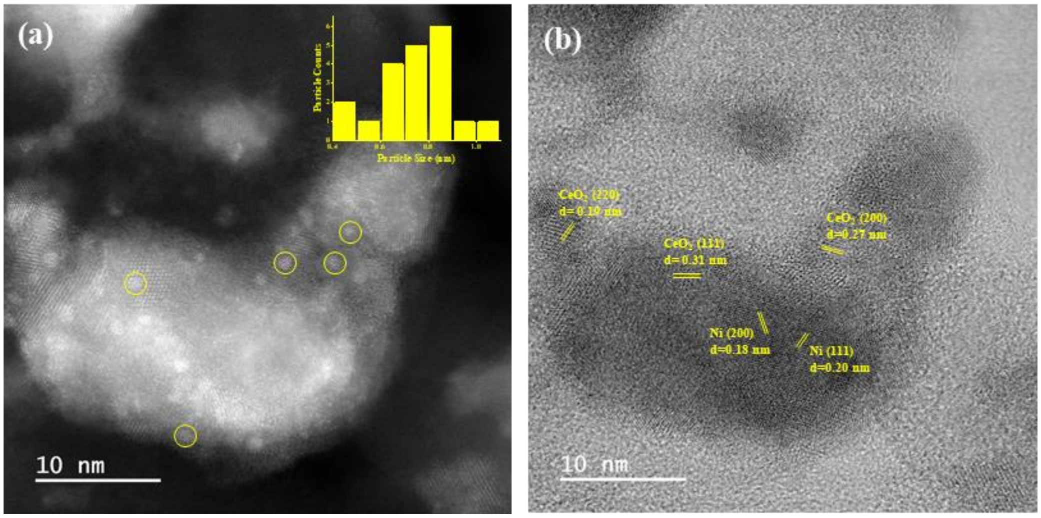

Figure 2.5. (a) HAADF-STEM and (b) HRTEM images of reduced $Pt^{0.25}$-NiCe/SiO_2^{WI}.

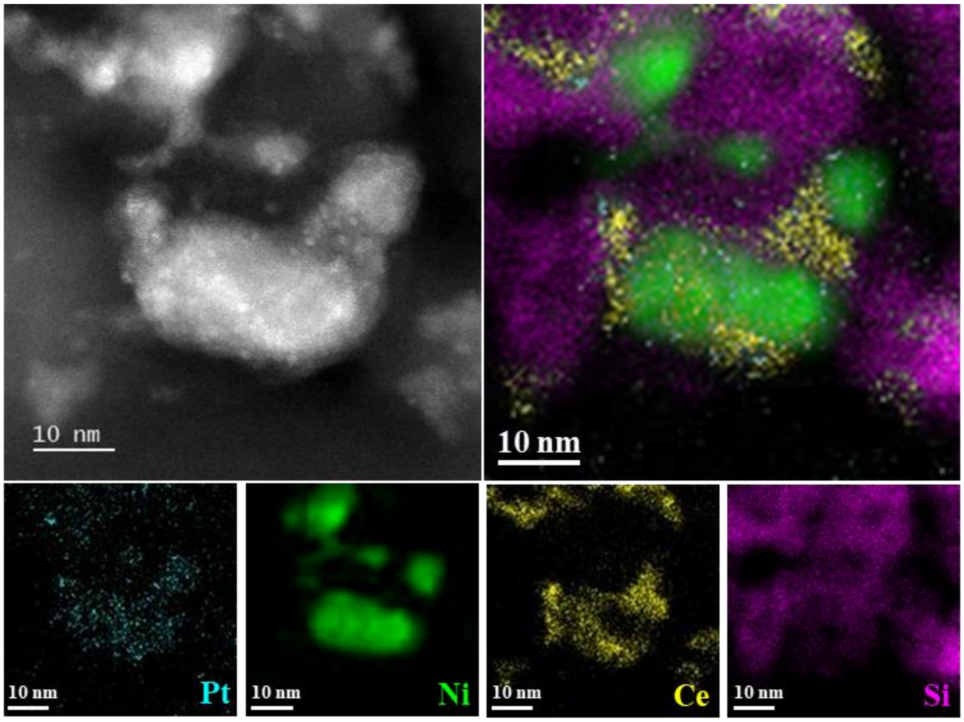

Figure 2.6. EDX elemental mapping images of reduced $Pt^{0.25}$-NiCe/SiO_2^{WI}.

species matches with the nanoclusters marked in Figure 2.5. As shown in Figure 2.7, single distributed Pt atoms (some of them are indicated by red circles) can also be detected on the Ni and Ce nanoparticles, suggesting the co-existence of Pt nanoclusters and Pt single-atoms in the reduced $Pt^{0.25}$-NiCe/SiO_2^{WI}. This observation implies that the impregnated catalysts with 0.25 wt% Pt can have less Pt–Ni interaction than the yolk−shell SAA catalysts. Pt and Pt–Ni alloy

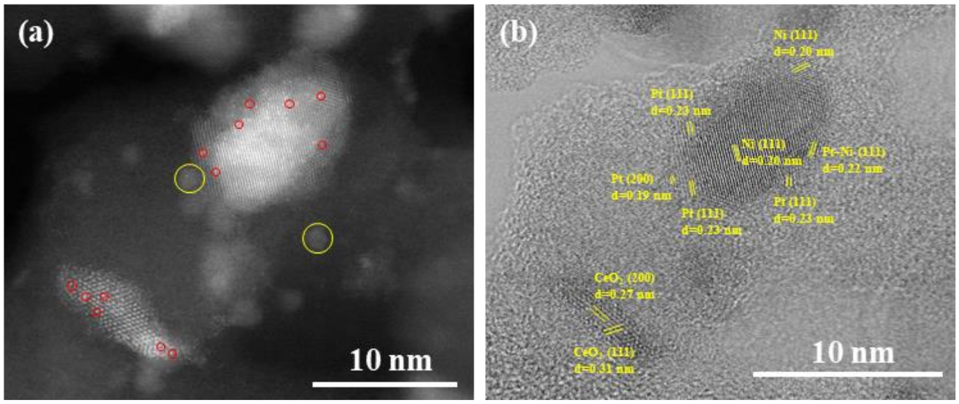

Figure 2.7. (a) HAADF-STEM and (b) HRTEM images of reduced $Pt^{0.25}$-NiCe/SiO_2^{WI}.

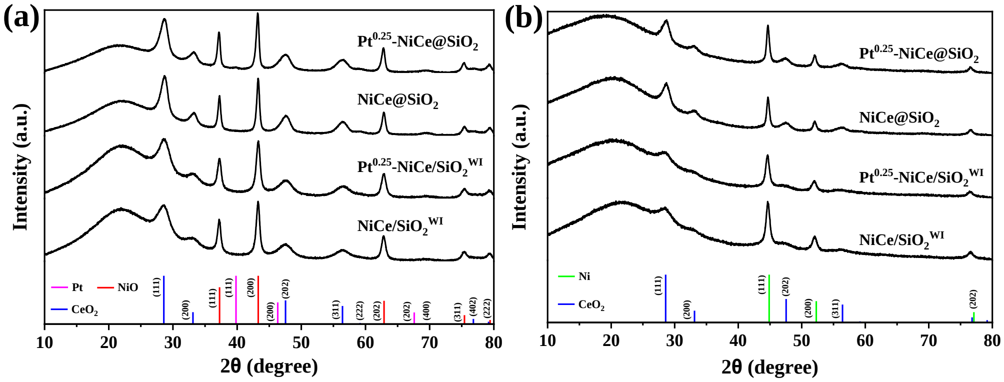

Figure 2.8. XRD patterns of (a) fresh and (b) reduced yolk–shell and impregnated catalysts with and without 0.25 wt% Pt promotion.

species are mostly observed at the edges of the Ni nanoparticles for the impregnated catalyst, which is consistent with the yolk–shell morphology (Figure 2.7b).

The XRD patterns of the fresh yolk–shell and impregnated catalysts with and without 0.25 wt% Pt promotion are shown in Figure 2.8a. All fresh catalysts show the NiO and CeO_2 diffraction patterns together with amorphous SiO_2. The peaks at 2θ of 37.3°, 43.3°, 62.9°, and 75.4° belong to the cubic rock salt structure of NiO, and the peaks at 2θ of 28.6°, 33.1°, 47.5°, and 56.4° correspond to the cubic fluorite structure of CeO_2. The broad peak observed at 2θ of 21.6° indicates amorphous SiO_2. Pt diffraction peaks could not be detected clearly on the 0.25 wt% of Pt-promoted catalysts for both yolk–shell SAA and impregnated catalysts due to the low

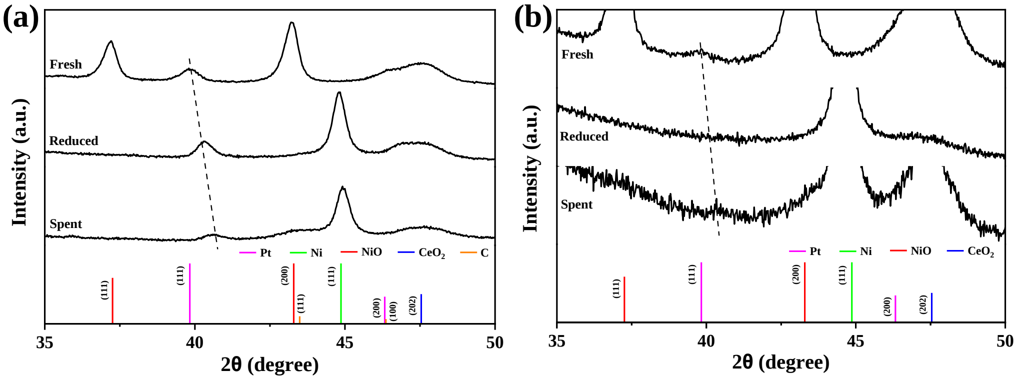

Figure 2.9. XRD patterns of fresh, reduced, and spent for (a) Pt^1-NiCe@SiO_2 and (b) $Pt^{0.25}$-NiCe@SiO_2.

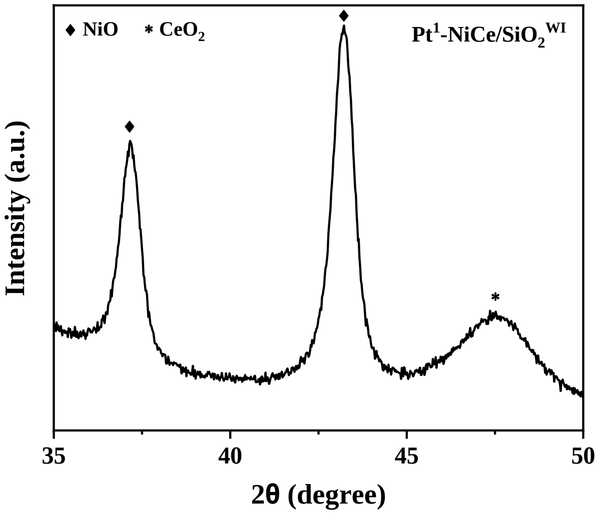

Figure 2.10. XRD pattern of fresh Pt^1-NiCe/SiO$_2$^{WI}.

concentration and high dispersion of the Pt species. Additionally, XRD patterns of the 1 wt% of Pt-promoted catalysts in the 2θ range of 35–50° are shown in Figure 2.9a. The result indicates that Pt peaks appear at 2θ of 39.8° and 46.3° for the fresh 1 wt% Pt-promoted yolk–shell catalysts, while Pt phases could not be identified for the impregnated catalysts, possibly due to the highly dispersed Pt on the support (Figure 2.10). Figure 2.8b represents the XRD patterns of the yolk–shell and impregnated catalysts with and without Pt promotion after 3 hours of H_2 reduction at 500 °C. The background noise in the XRD patterns is associated with the quartz wool used in the reactor. The peaks at 2θ of 44.7°, 52.0°, and 76.6° correspond to the metallic Ni phase. NiO phase is not identified in all samples indicating that NiO is fully reduced to metallic Ni, which is an active phase for the DRM.[9,125]

The Pt (111) peaks for the fresh, reduced, and spent Pt$^{0.25}$-NiCe@SiO$_2$ are compared in Figure 2.9b. It has been shown that the Pt (111) peak observed in the fresh sample is not detected in the reduced Pt$^{0.25}$-NiCe@SiO$_2$, suggesting the formation of the isolated Pt atoms after the reduction. The Pt (111) peak for the spent one is located at a higher 2θ of 40.3° than that of 39.8°

for the fresh one. This peak shift is more distinct when the same analysis is performed on Pt^1-NiCe@SiO$_2$ (Figure 2.9a). These results imply that Pt atoms might be incorporated into the Ni lattice leading to the formation of Pt–Ni SAA structures,[117,118,126,127] which is in good agreement with the HRTEM analysis. The lattice constants of the reduced catalysts are determined by Rietveld refinement, as shown in Table 2.1. It is found that the Ni lattice constant slightly increases after Pt promotion, suggesting the formation of Pt–Ni SAAs. The ceria lattice constant also increases for both yolk–shell SAA and impregnated catalysts after Pt promotion due to the partial reduction of Ce^{4+} to Ce^{3+}. Scherrer equation is implemented to calculate the crystallite size using the (111) plane of the species, as shown in Table 2.1. The fresh impregnated catalysts without Pt promotion have smaller crystallite sizes of 12.90 nm and 4.79 nm for NiO and CeO$_2$, respectively, compared to the fresh yolk–shell catalysts (15.99 nm and 6.58 nm for NiO and CeO$_2$) due to the higher metal dispersion on the SiO$_2$ support.[99] Addition of 0.25 wt% Pt slightly decreases the NiO crystallite size to 15.73 nm and 11.83 nm for the yolk–shell SAA and impregnated catalysts, respectively, which is in good agreement with the literature.[105,106] Similar to the fresh catalysts, the reduced NiCe/SiO$_2^{WI}$ has smaller crystallite sizes of 12.35 nm and 4.11 nm for Ni and CeO$_2$, respectively, compared to those in the reduced NiCe@SiO$_2$ (16.31 nm and

Table 2.1. Crystallite size and lattice constant for fresh and reduced yolk–shell and impregnated catalysts with and without 0.25 wt.% Pt promotion

Catalysts		NiO		Ni		CeO$_2$		Pt	
		Crystal size (nm)^a	Lattice constant (Å)^b	Crystal size (nm)^a	Lattice constant (Å)^b	Crystal size (nm)^a	Lattice constant (Å)^b	Crystal size (nm)^a	Lattice constant (Å)^b
Fresh	Pt$^{0.25}$-NiCe@SiO$_2$	15.73	4.188	-	-	5.71	5.401	5.44	3.932
	NiCe@SiO$_2$	15.99	4.179	-	-	6.58	5.392	-	-
	Pt$^{0.25}$-NiCe/SiO$_2^{WI}$	11.83	4.183	-	-	4.95	5.405	-	-
	NiCe/SiO$_2^{WI}$	12.90	4.179	-	-	4.79	5.388	-	-
Reduced	Pt$^{0.25}$-NiCe@SiO$_2$	-	-	16.25	3.523	6.66	5.411	-	-
	NiCe@SiO$_2$	-	-	16.31	3.521	6.15	5.399	-	-
	Pt$^{0.25}$-NiCe/SiO$_2^{WI}$	-	-	12.06	3.522	5.14	5.410	-	-
	NiCe/SiO$_2^{WI}$	-	-	12.35	3.521	4.11	5.391	-	-

^{a}Calculated by Scherrer equation for (111) plane. ^{b}Measured by Rietveld refinement.

6.15 nm for Ni and CeO_2). With the addition of 0.25 wt% Pt, the crystallite size of Ni in both reduced yolk–shell SAA and impregnated catalysts decrease to 16.25 nm and 12.06 nm, respectively. The crystallite sizes of the reduced Ni and CeO_2 calculated by the XRD measurement are smaller than the yolk sizes determined by the TEM analysis, indicating that the yolks are in polycrystalline form. For the high loading of Pt (1 wt%), the reduced yolk–shell catalyst shows a large Pt crystallite size of 15.00 nm by XRD (not shown here).

The XPS spectra of Ni and Ce species in $Pt^{0.25}$-NiCe@SiO_2 and NiCe@SiO_2 after 1 h of *in situ* H_2 reduction are shown in Figure 2.11. The Ni 2p core-level spectra of both catalysts show characteristic Ni^0 and Ni^{2+} peaks of Ni $2p_{3/2}$ and Ni $2p_{1/2}$ with shake-up satellites. For the Pt-promoted catalysts, the Ni $2p_{3/2}$ core level energies located at 852.4 eV and 853.5 eV are assigned to Ni^0 and Ni^{2+}, respectively. These Ni $2p_{3/2}$ core level energies are similar to the non-promoted catalysts (852.3 eV and 853.4 eV). Although non- and Pt-promoted catalysts show similar Ni binding energies, Pt promotion increases the reducibility of Ni species, such that $Pt^{0.25}$-NiCe@SiO_2 has a higher Ni^0 concentration of 62.6% compared to that of NiCe@SiO_2 (57.5%). The Ce 3d core-level spectra can be deconvoluted into multiple peaks for Ce $3d_{5/2}$ (v) and Ce $3d_{3/2}$ (u), where v and v'' peaks and v_0 and v' peaks are associated with Ce^{4+} and Ce^{3+},

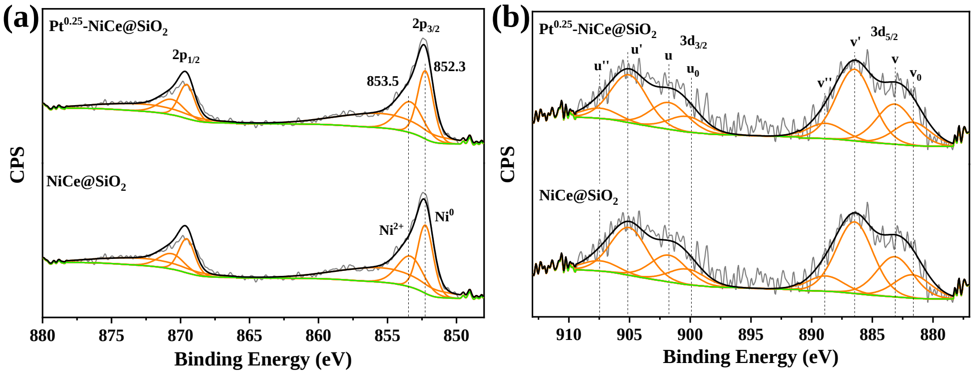

Figure 2.11. (a) Ni 2p and (b) Ce 3d XPS spectra of reduced $Pt^{0.25}$-NiCe@SiO_2 and NiCe@SiO_2.

respectively. Similar to the Ni species, the reducibility of Ce species increases after Pt promotion. Our results show that the Ce^{3+} concentration of $Pt^{0.25}$-NiCe@SiO_2 (63.1%) is higher than that of NiCe@SiO_2 (59.4%), indicating that more oxygen vacancies are formed in the ceria lattice after Pt promotion. The interaction between Pt and CeO_2 is observed in the HRTEM analysis in which a slight lattice expansion of Pt (111) has been detected (Figure 2.1d). It is possible that Pt can be incorporated into the Ce lattice leading to a partial reduction of Ce^{4+} to Ce^{3+} and an increase in the Ce–O bond length.[105,128,129] This increase is consistent with the small change of the CeO_2 lattice constant calculated in the XRD analysis (Table 2.1). High Ce^{3+} concentration observed after Pt promotion refers to an increased oxygen storage capacity of CeO_2, which can enhance the carbon removal efficiency if Ce is located in close proximity to Pt and Ni.[130] It is important to note that Pt peaks for $Pt^{0.25}$-NiCe@SiO_2 could not be observed in XPS due to the low Pt loading (Figure 2.12).

H_2-TPR analysis is performed to investigate the catalyst reducibility and metal-support interaction. Figure 2.13 shows the H_2-TPR profiles of the yolk–shell and impregnated catalysts with and without 0.25 wt% Pt promotion. In addition to these samples, $Pt^{0.25}$-Ni/SiO_2^{WI}, $Pt^{0.25}$-

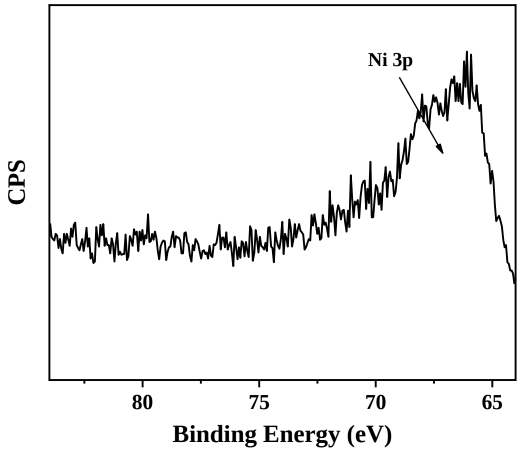

Figure 2.12. XPS spectrum of $Pt^{0.25}$-NiCe@SiO_2 in the Pt 4f region.

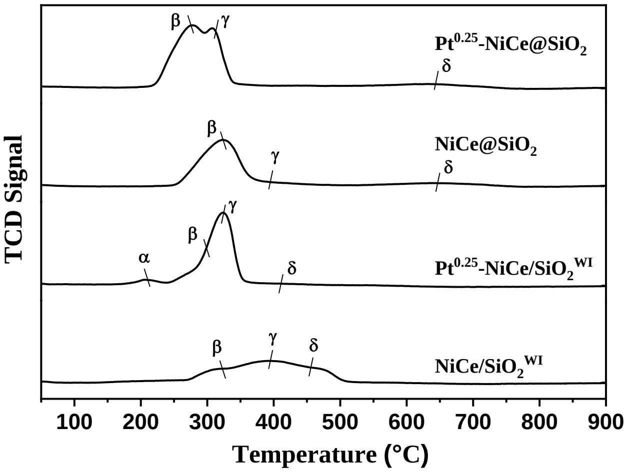

Figure 2.13. H_2-TPR profiles for yolk–shell and impregnated catalysts with and without 0.25 wt% Pt promotion.

Ce/SiO_2^{WI}, and $Pt^{0.2\,5}$/SiO_2^{WI} with the same nominal loading of Ni or Ce are synthesized by wet impregnation and evaluated for their reducibility to identify the Ni reduction peaks (Figure 2.14). No H_2 consumption peaks are detected when Ni is not present, indicating that all major reduction peaks observed in Figure 2.13 are associated with the Ni species. The H_2 consumption peak of β observed at temperatures from 240 °C to 350 °C is attributed to the reduction of bulk and aggregated NiO interacting with CeO_2. The γ peak shown in the medium temperature region

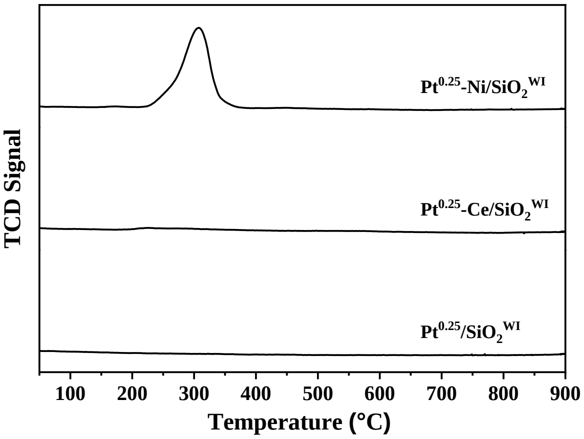

Figure 2.14. H_2-TPR profiles for $Pt^{0.25}$-Ni/SiO_2^{WI}, $Pt^{0.25}$-Ce/SiO_2^{WI}, and $Pt^{0.25}$/SiO_2^{WI}.

from 270 °C to 400 °C is associated with the dispersed NiO interacting with CeO_2. Observation of the γ peak at higher temperatures than the β peak can be attributed to the dispersed Ni species strongly coordinated with CeO_2.[52,131] In the case of $Pt^{0.25}$-Ni/SiO_2^{WI}, the major reduction peak for NiO located at 307.2 °C (Figure 2.14) shifts to a higher temperature (323.5 °C) after Ce promotion (Figure 2.13) due to the enhanced Ni–support interaction. Since impregnated catalysts have more dispersed Ni species on the support evidenced by the XRD and H_2 chemisorption analysis (Table 2.2), it has a low β/γ peak ratio compared to the yolk–shell catalysts. The broad δ peak located at temperatures above 400 °C is assigned to the reduction of NiO interacting with SiO_2 support.[99] The δ peak for NiCe@SiO_2 is located at a much higher temperature (648 °C) than that for NiCe/SiO_2^{WI} (456 °C), indicating that the yolk–shell catalyst exhibits stronger metal-support interaction than the impregnated catalyst. The strong metal-support interaction in a confined morphology, especially in the two-dimensional yolk–shell structure, can inhibit the carbon deposition and metal sintering leading to improved catalyst stability.[132] Compared to the H_2-TPR of the catalysts without Pt promotion, the addition of 0.25 wt% Pt to both yolk–shell SAA and impregnated catalysts shifts β, γ, and δ peaks to the lower reduction temperatures while providing higher reduction intensity and narrower reduction peaks. This can be attributed to H_2 spillover from Pt to Ni as Pt can facilitate H_2 dissociation and promote NiO reduction. In addition, a small peak of α located at around 200 °C is observed for impregnated

Table 2.2. H_2 uptake and Ni dispersion measured by H_2 chemisorption for yolk–shell and impregnated catalysts with and without Pt promotion.

Catalysts	H_2 uptake (mmol g^{-1})	Ni dispersion (%)
Pt^1-NiCe@SiO_2	0.0046	0.31%
$Pt^{0.25}$-NiCe@SiO_2	0.0050	0.30%
Pt^1-NiCe/SiO_2^{WI}	0.0231	1.46%
$Pt^{0.25}$-NiCe/SiO_2^{WI}	0.0143	0.92%

$Pt^{0.25}$-NiCe/SiO_2^{WI}, which pertains to the reduction of PtO_x nanoclusters.[107] This is consistent with the HRTEM analysis as the impregnated catalysts are shown to contain Pt nanoclusters. The appearance of the α peak can suggest that the impregnated catalysts have more pronounced Pt–CeO_2 interaction compared to the yolk–shell SAA catalysts. The absence of the α peak in the yolk–shell catalysts may suggest that the Pt species is highly distributed mainly on the Ni species as SAA structure rather than presented as PtO_x nanoclusters on the yolks or support.

Generally, the hydrogen reduction peaks for the yolk–shell catalyst after 0.25 wt% Pt promotion are located at lower reduction temperatures than those for the impregnated catalysts, which might imply that Pt is dispersed as single-atoms on the active Ni species forming the yolk–shell SAA structures. To elucidate Pt effect on the reduction, H_2-TPR of the 1 wt% Pt-promoted catalysts are analyzed along with the 0.25 wt% Pt-promoted catalysts (Figure 2.15 and Table 2.3). In most cases, the overall hydrogen uptakes are almost identical or slightly higher than the total amount of metals, considering two moles and one mole of H_2 consumed per one mole of Pt and Ni, respectively. However, the H_2 uptake for the α peak in the impregnated

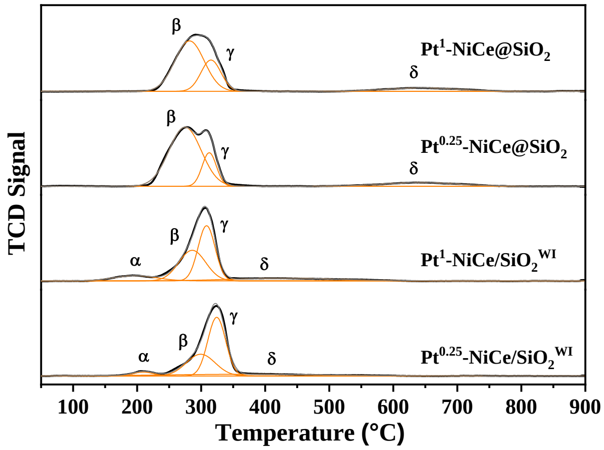

Figure 2.15. H_2-TPR profiles for Pt^1-NiCe@SiO_2, $Pt^{0.25}$-NiCe@SiO_2, Pt^1-NiCe/SiO_2^{WI}, and $Pt^{0.25}$-NiCe/SiO_2^{WI}.

catalysts is much larger than the actual amount of Pt (measured by ICP-OES (Table 2.4)), and it increases with the Pt loading (Table 2.3). This result can be explained by the H_2 spillover from the adjacent Pt or incorporated Pt species into the CeO_2 lattice leading to the lattice oxygen reduction of CeO_2, which is also observed in the HRTEM analysis (Figure 2.7).[133–135]

Table 2.3. H_2 uptake during H_2-TPR experiments for Pt^1-NiCe@SiO_2, $Pt^{0.25}$-NiCe@SiO_2, Pt^1-NiCe/SiO_2^{WI}, and $Pt^{0.25}$-NiCe/SiO_2^{WI}.

Catalyst	Pt (mmol)[a]	Ni (mmol)[a]	H_2 uptake (mmol)				
			α	β	γ	δ	Sum
Pt^1-NiCe@SiO_2	0.0015	0.086	-	0.058	0.024	0.010	0.092
$Pt^{0.25}$-NiCe@SiO_2	0.0006	0.101	-	0.074	0.019	0.011	0.104
Pt^1-NiCe/SiO_2^{WI}	0.0023	0.080	0.009	0.032	0.037	0.011	0.089
$Pt^{0.25}$-NiCe/SiO_2^{WI}	0.0006	0.078	0.003	0.024	0.041	0.011	0.079

[a] Measured by ICP-OES analysis.

Table 2.4. Metallic content of Pt^1-NiCe@SiO_2, $Pt^{0.25}$-NiCe@SiO_2, Pt^1-NiCe/SiO_2^{WI}, and $Pt^{0.25}$-NiCe/SiO_2^{WI} measured by ICP-OES.

Catalysts	Pt		Ni		Ce	
	Nominal	ICP	Nominal	ICP	Nominal	ICP
Pt^1-NiCe@SiO_2	1	0.88	9.23	9.76	5.82	5.72
$Pt^{0.25}$-NiCe@SiO_2	0.25	0.22	9.23	8.34	5.82	6.55
Pt^1-NiCe/SiO_2^{WI}	1	1.34	9.23	9.68	5.82	8.03
$Pt^{0.25}$-NiCe/SiO_2^{WI}	0.25	0.36	9.23	8.90	5.82	7.20

2.3.2 Activity measurements

The DRM performance of the yolk–shell and impregnated catalysts with and without 0.25 wt% Pt promotion is evaluated at 500 °C for 20 h TOS, as shown in Figure 2.16. The DRM performances are assessed over 75 mg catalyst with particle sizes of 250–420 μm. The inter/intra-particle mass transfer resistances are evaluated by varying the gas hourly space velocity (GHSV) and particle size of the catalysts, respectively, at 500 °C under DRM condition as shown in Figure 2.17. The former one is confirmed by changing the mass of catalysts with

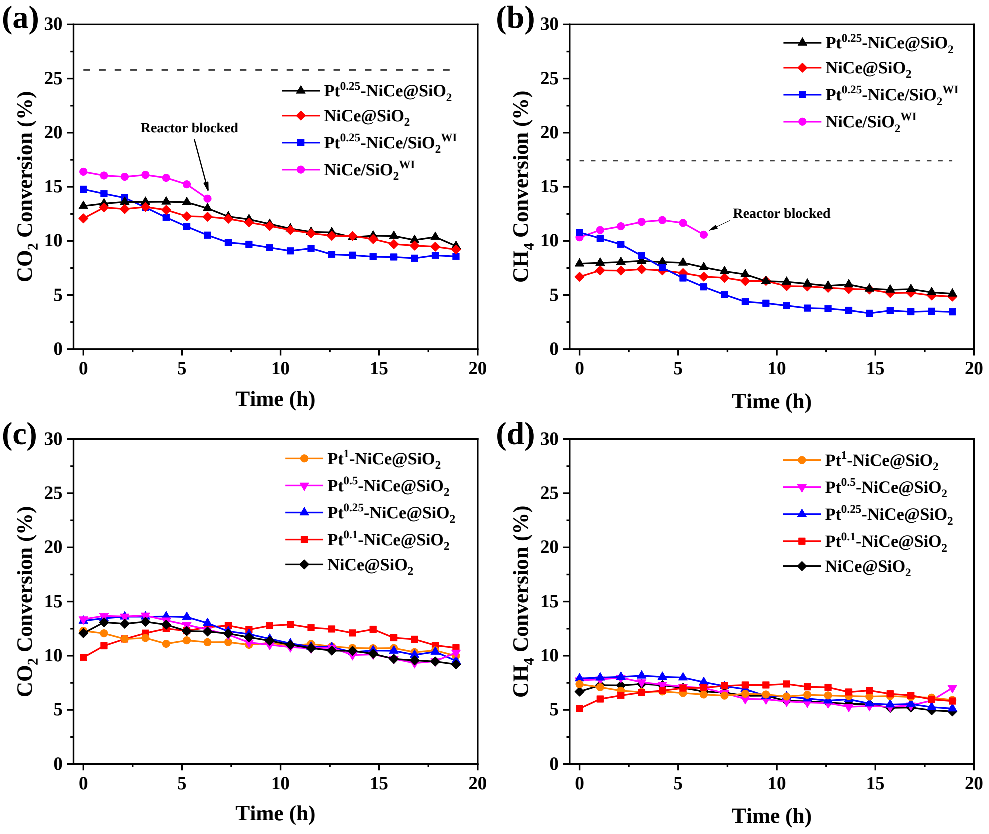

Figure 2.16. (a) CO_2 and (b) CH_4 conversions of yolk–shell and impregnated catalysts with and without 0.25 wt% Pt promotion under DRM at 500 °C (Dashed line indicates equilibrium conversion). (c) CO_2 and (d) CH_4 conversions of Pt^x-NiCe@SiO_2 in different wt% of Pt under DRM at 500 °C.

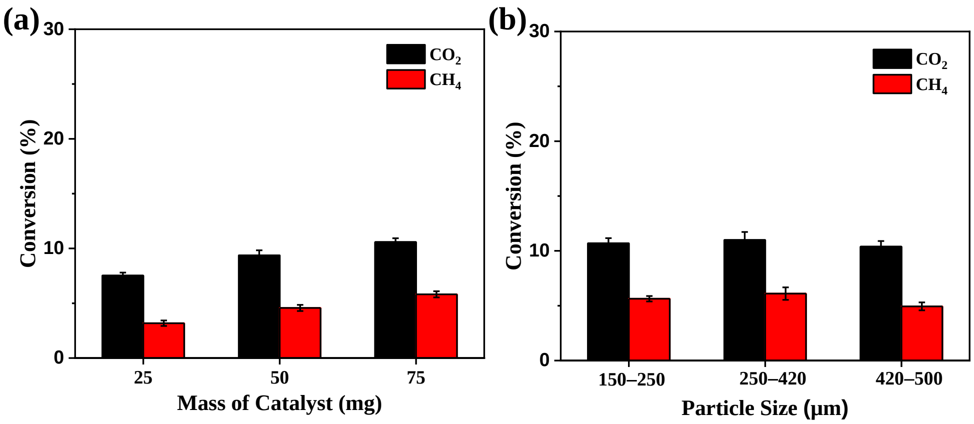

Figure 2.17. CO_2 and CH_4 conversions of $Pt^{0.25}$-NiCe@SiO_2 under DRM at 500 °C for (a) external mass transport resistance and (b) internal mass transport resistance measurements.

keeping constants of other parameters, and latter one is measured by varying the particle size of the catalysts with keeping constants of other parameters. The result shows that both CO_2 and CH_4 conversions does not increase at a high GHSV, indicating that no external mass transport resistance. The CO_2 and CH_4 conversions are also maintained at all ranges of particle size, demonstrating that the internal mass transport resistance is not occurred. Thermodynamic equilibrium conversions for CO_2 and CH_4 are calculated to be 25.8% and 17.4% at 500 °C, respectively, considering DRM and RWGS reaction ($CO_2 + H_2 \rightarrow CO + H_2O$, $\Delta H^o = +40.6$ kJ mol^{-1}). It has been observed that the impregnated catalysts with and without Pt promotion have slightly higher initial CO_2 and CH_4 conversion than the yolk–shell catalysts, possibly due to the higher metal dispersion. Despite their high initial conversion, the impregnated catalysts show fast deactivation. In particular, the activity of NiCe/SiO_2^{WI} plummets after 6 h TOS due to the severe carbon deposition, which blocks the catalyst bed. Addition of 0.25 wt% Pt to NiCe/SiO_2^{WI} significantly improves the catalyst stability, yet the conversions of CO_2 and CH_4 for $Pt^{0.25}$-NiCe/SiO_2^{WI} still decrease by 43.1% and 69.3%, respectively, over 20 h TOS. On the other hand, $Pt^{0.25}$-NiCe@SiO_2 shows a slight decrease in CO_2 and CH_4 conversions by 21.6% and 33.6%, respectively, over 20 h TOS.

The catalytic conversion rates of CO_2 and CH_4 are calculated and shown in Figure 2.18. $Pt^{0.25}$-NiCe/SiO_2^{WI} demonstrates the highest initial CO_2 and CH_4 conversion rates of 0.392 mmol g_{Ni+Pt}^{-1} s^{-1} and 0.277 mmol g_{Ni+Pt}^{-1} s^{-1}, while NiCe@SiO_2 exhibits the lowest initial CO_2 and CH_4 conversion rates of 0.287 mmol g_{Ni+Pt}^{-1} s^{-1} and 0.151 mmol g_{Ni+Pt}^{-1} s^{-1}, respectively. However, the activity of $Pt^{0.25}$-NiCe/SiO_2^{WI} decreases fast, reaching a plateau at 0.1 mmol g_{Ni+Pt}^{-1} s^{-1} for the CH_4 conversion rate within 10 h due to severe carbon formation. Among the catalysts tested, $Pt^{0.25}$-NiCe@SiO_2 achieves the highest activity over 20 h TOS. The yolk–shell catalysts show stable activity for up to 5 h, and the activity gradually decreases after 5 h, whereas

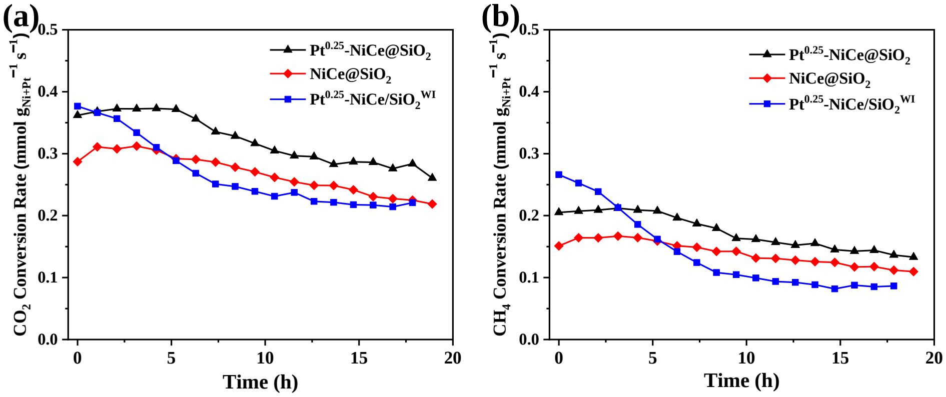

Figure 2.18. (a) CO_2 and (b) CH_4 conversion rates of Pt$^{0.25}$-NiCe@SiO$_2$, NiCe@SiO$_2$, and Pt$^{0.25}$-NiCe/SiO$_2^{WI}$ under DRM at 500 °C.

the impregnation catalysts deactivate fast for the first 10 h, and the activity stabilizes after 10 h. The yolk–shell catalysts show an increase in the activity during the initial hours of the reaction (Figure 2.16), possibly due to the reconstruction of the metal sites after interaction with the reactants and products. It is reported that the reconstruction of the active sites can be more pronounced on the larger size nanoparticles.[136] The yolk–shell catalysts with larger Ni crystallite size (16.2 nm) (compared to the impregnated catalysts (12.1 nm)) show stable or increased activity in the beginning of the reaction. However, the activity can still gradually decrease by sintering. In the case of the impregnated catalysts, severe carbon accumulation can be observed in the TGA and XRD analysis of the spent samples, which is discussed in Section 2.3.3. This fast deactivation can be attributed to the blocking of the active sites by carbon species. The carbon formation and carbon removal reaction rate can be similar to each other after ~10 h of reaction, which might stabilize the activity. The CO and H_2 yields and H_2/CO ratios of the catalysts are shown in Table 2.5. In general, all catalysts exhibit a higher CO_2 conversion than CH_4, and their H_2/CO ratios are below unity, indicating the effect of the concurrent RWGS reaction. The H_2/CO ratios of the yolk–shell catalysts (0.46-0.49) are lower than those of the impregnated catalysts (0.57–0.79), implying that RWGS reaction is favored on the yolk–shell catalyst. A strong oxidant like water produced by RWGS reaction can reduce the carbon formation, enhancing the catalyst stability.[64]

Table 2.5. H_2 and CO yield and H_2/CO ratio of yolk–shell and impregnated catalysts with and without 0.25 wt.% Pt promotion under DRM at 500 °C and 750 °C.

Reaction	Catalysts	H_2 yield (%)	CO yield (%)	H_2/CO ratio
500 °C	$Pt^{0.25}$-NiCe@SiO_2	5.38	10.75	0.49
	NiCe@SiO_2	4.67	9.84	0.46
	$Pt^{0.25}$-NiCe/SiO_2^{WI}	5.19	8.94	0.57
	NiCe/SiO_2^{WI}	7.60	9.28	0.79
750 °C	$Pt^{0.25}$-NiCe@SiO_2	54.9	64.1	0.89

2.3.3 XAS analysis in different Pt loadings

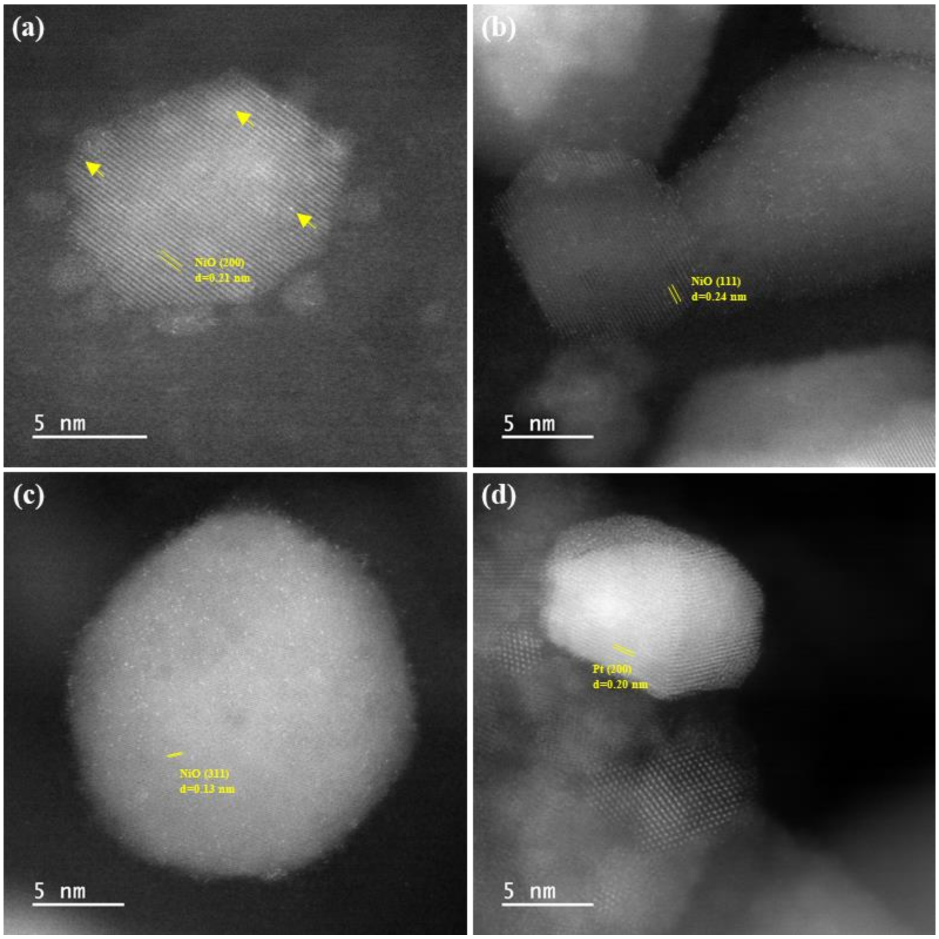

Figure 2.19. AC-HAADF-STEM images of fresh (a) $Pt^{0.1}$-NiCe@SiO_2, (b) $Pt^{0.25}$-NiCe@SiO_2, (c) $Pt^{0.5}$-NiCe@SiO_2, and (d) Pt^{1}-NiCe@SiO_2.

The effect of Pt loadings on the structure and DRM activity of the yolk–shell catalysts has also been studied by the addition of 0.1 wt%, 0.5 wt% and 1 wt% Pt. Figure 2.19 shows the representative AC-HAADF-STEM images of the fresh $Pt^{0.1}$-NiCe@SiO_2, $Pt^{0.25}$-NiCe@SiO_2, $Pt^{0.5}$-NiCe@SiO_2, and Pt^{1}-NiCe@SiO_2. As it can be seen in Figure 2.19a–c, individual Pt atoms are displayed as bright dots with higher contrast than the surrounding NiO lattice.[137] The NiO nanoparticles (10–20 nm) exhibit lattice fringes of 0.21 nm, 0.24 nm, and 0.13 nm, assigned to the (200), (111), and (311) planes, respectively. The low number of Pt single atoms (indicated by arrows) observed for $Pt^{0.1}$-NiCe@SiO_2 can be due to the small Pt loading (Figure 2.19a). Both $Pt^{0.25}$-NiCe@SiO_2 and $Pt^{0.5}$-NiCe@SiO_2 display well dispersed Pt single-atoms on NiO, as shown in Figure 2.19b,c. However, small Pt nanoparticles (~3 nm) with 0.20 nm lattice fringe for Pt (200) are detected for $Pt^{0.5}$-NiCe@SiO_2 (Figure 2.20a). When the Pt/Ni atomic ratio is increased (Pt^{1}-NiCe@SiO_2), large Pt nanoparticles (~10 nm) are observed, as shown in Figure 2.19d. This large Pt nanoparticles are also verified by the EDX elemental mapping (Figure 2.21), where the analyzed nanoparticle is only composed of Pt species. It is noted that the low number

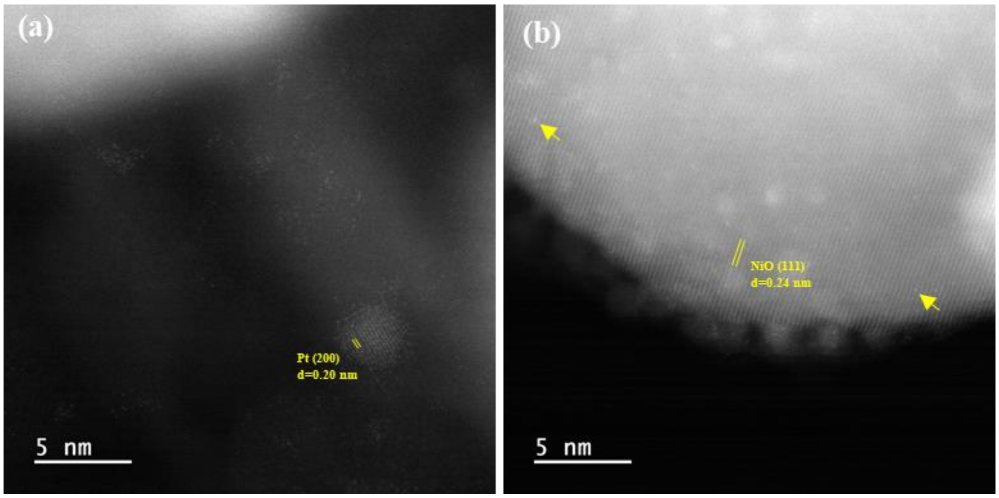

Figure 2.20. AC-HAADF-STEM images of fresh (a) $Pt^{0.5}$-NiCe@SiO_2 and (b) Pt^{1}-NiCe@SiO_2.

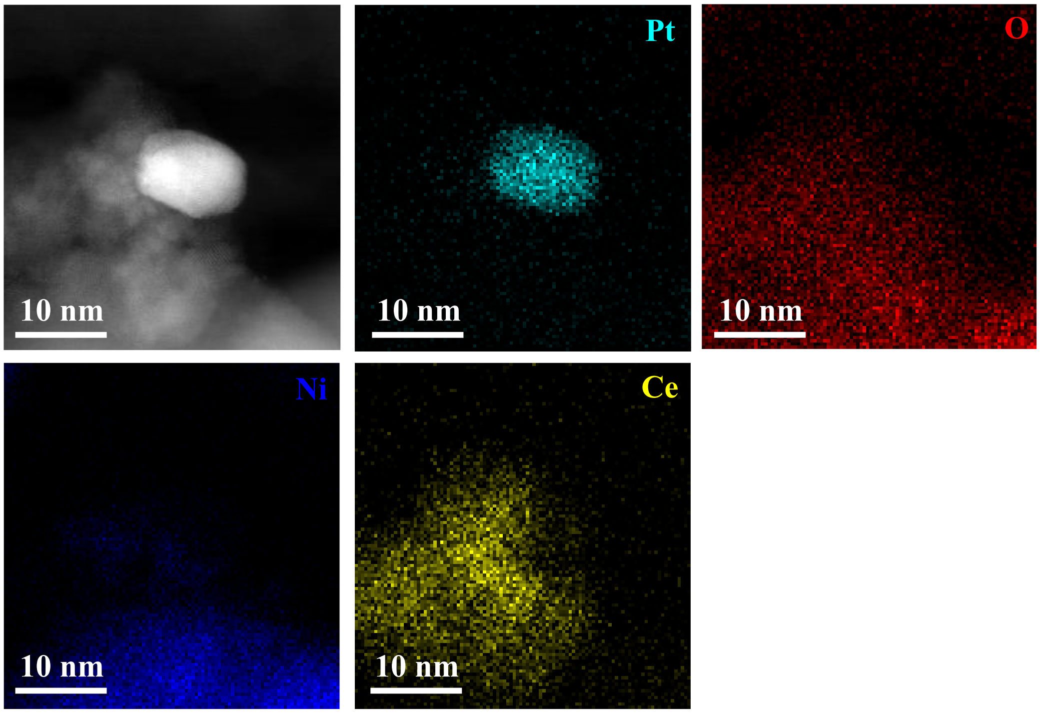

Figure 2.21. EDX elemental mapping images of fresh Pt^1-NiCe@SiO_2.

of Pt single atoms (indicated by arrows) can be anchored on NiO nanoparticles (Figure 2.20b), while the majority of Pt species form Pt nanoparticles.

Figure 2.22a displays the normalized XANES spectra of the catalysts loaded with different amount of Pt. The Pt foil and PtO_2 references at the Pt L_3-edge are also plotted. The

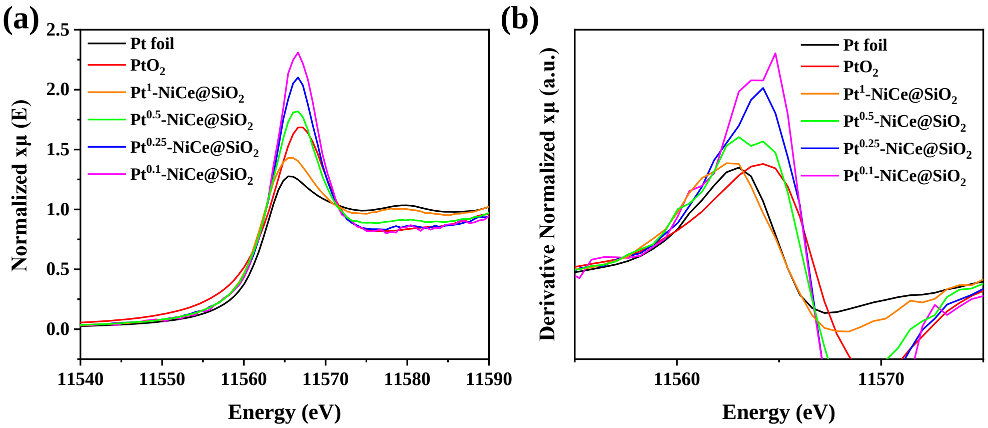

Figure 2.22. (a) Normalized XANES spectra and (b) first-order derivative of the XANES spectra at Pt L_3-edge for fresh $Pt^{0.1}$-NiCe@SiO_2, $Pt^{0.25}$-NiCe@SiO_2, $Pt^{0.5}$-NiCe@SiO_2, Pt^1-NiCe@SiO_2, Pt foil, and PtO_2.

absorption edges of Pt foil and PtO_2 appear at 11563.0 eV and 11564.2 eV indicating Pt^0 and Pt^{4+}, respectively. The white lines for the fresh $Pt^{0.1}$-NiCe@SiO_2, $Pt^{0.25}$-NiCe@SiO_2, $Pt^{0.5}$-NiCe@SiO_2 are similar to that of PtO_2, indicating the Pt species are in a highly oxidized state. It is also confirmed that the Pt species are in cationic states from the first-order derivative of the XANES spectra (Figure 2.22b). The adsorption edge shifts to the lower energy values as the Pt loading increases, suggesting that Pt–Pt interaction gets stronger. The white line intensity for the $Pt^{0.1}$-NiCe@SiO_2, $Pt^{0.25}$-NiCe@SiO_2, and $Pt^{0.5}$-NiCe@SiO_2 catalysts are higher than that for PtO_2 due to the Pt 5d orbital of vacancy generated by the atomically dispersed Pt on NiO.[137] The singly distributed Pt atoms over the oxide can facilitate charge transfer between metal atoms and host oxide due to the strong metal–support interaction. On the other hand, the normalized XANES data for Pt^1-NiCe@SiO_2 has the lowest rising absorption edge intensity, and its features are closer to the Pt foil spectrum. This is due to the Pt nanoparticle formation, in good agreement with the TEM analysis. Additionally, the white line intensity of Pt^1-NiCe@SiO_2 is in between that of the Pt foil and PtO_2, suggesting a mixture of the two states due to the possible Pt–SiO_2 support interaction.[138]

Figure 2.23a,b show the k^2-weighted EXAFS and Fourier transformed EXAFS spectra of the fresh catalysts with different Pt loadings, respectively. Table 2.6 shows the structural parameters obtained from the EXAFS fittings of the first shell. The first prominent peak at 1.7 Å (without phase correction) in Figure 2.23b is attributed to the Pt–O contribution. This Pt–O contribution has a bond distance of 2.04 Å with coordination numbers (CN) in between 3 and 4 for the low Pt-loaded catalysts, i.e. $Pt^{0.1}$-NiCe@SiO_2 and $Pt^{0.25}$-NiCe@SiO_2, which can be originated from the Pt atoms coordinated with four oxygen atoms on the host NiO.[139] The close bond distance of Pt–O for the low Pt-loaded catalysts and PtO_2 can imply strong Pt–NiO interaction.[140] The

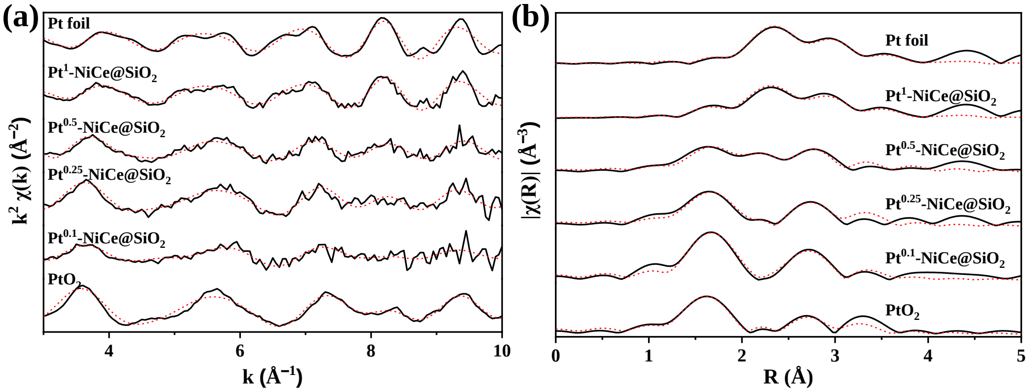

Figure 2.23. k^2-weighted (a) EXAFS functions and (b) Fourier transforms of EXAFS spectra at Pt L_3-edge for fresh $Pt^{0.1}$-NiCe@SiO_2, $Pt^{0.25}$-NiCe@SiO_2, $Pt^{0.5}$-NiCe@SiO_2, Pt^1-NiCe@SiO_2, Pt foil, and PtO_2. The fitting data are displayed in dashed lines.

Table 2.6. Structural parameters obtained from the EXAFS fittings of the first shell at Pt L_3-edge for fresh $Pt^{0.1}$-NiCe@SiO_2, $Pt^{0.25}$-NiCe@SiO_2, $Pt^{0.5}$-NiCe@SiO_2, Pt^1-NiCe@SiO_2, Pt foil, and PtO_2. (CN: coordination number, R: internal atomic distances, ΔE_0: edge-energy shift, σ^2: Debye–Waller factor, R-factor: closeness of the fit)

Samples	Path	CN	R (Å)	ΔE_0	σ^2	R-factor
Pt foil	Pt–Pt	12*	2.76±0.00	7.5±0.5	3.8±0.2	0.004
PtO_2	Pt–O	6*	2.02±0.01	10.5±1.2	1.2±1.6	0.013
Pt^1-NiCe@SiO_2	Pt–O	0.5±0.2	2.02±0.01	6.1±1.6	3*	0.016
	Pt–Pt	7.6±1.4	2.74±0.01		3.7±1.5	
$Pt^{0.5}$-NiCe@SiO_2	Pt–O	2.9±1.1	2.05±0.02	15.0±3.4	7.0±6.9	0.015
$Pt^{0.25}$-NiCe@SiO_2	Pt–O	3.4±1.2	2.04±0.02	13.3±2.5	3.8±5.9	0.022
$Pt^{0.1}$-NiCe@SiO_2	Pt–O	3.9±1.7	2.04±0.02	13.7±2.1	0.8±5.0	0.012

second peak at 2.7 Å in the phase uncorrected spectra in Figure 2.23b can be originated from the next-nearest neighbor Ni atoms bridged by the nearest O atoms (not fitted).[137] For the catalysts with high Pt loadings, i.e. $Pt^{0.5}$-NiCe@SiO_2 and Pt^1-NiCe@SiO_2, Pt–Pt contribution begins to appear at 2.3 Å (without phase correction) in the Fourier transformed EXAFS spectra, because of the Pt nanoparticles formation. The EXAFS spectrum of Pt^1-NiCe@SiO_2 resembles to the Pt foil spectrum, indicating a Pt–Pt CN and bond length of 7.6 and 2.74 Å, respectively. This confirms

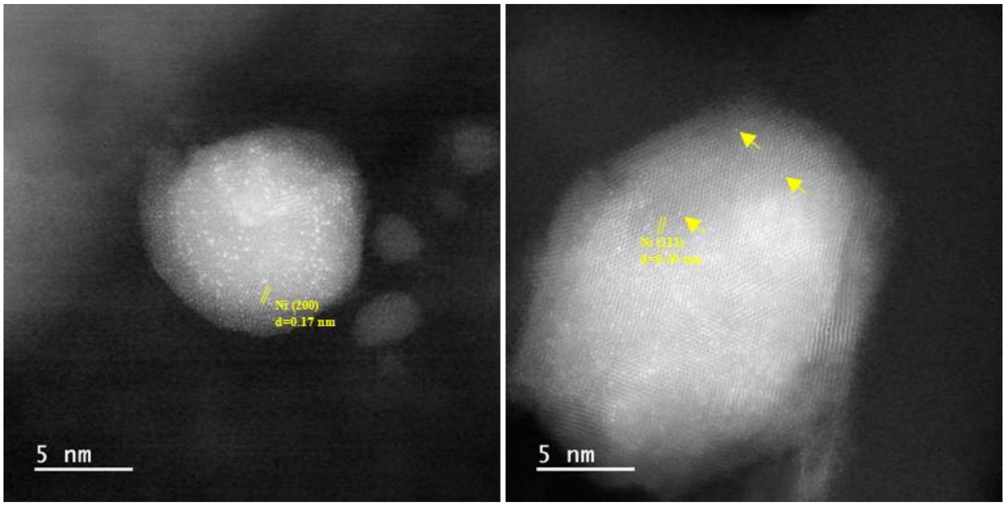

Figure 2.24. AC-HAADF-STEM images of reduced $Pt^{0.25}$-NiCe@SiO_2.

that large Pt (~10 nm) nanoparticles form at high Pt loadings, in consistent with the STEM analysis. Similar Pt–Pt CN (8) has been reported for the samples having Pt sizes of 10 nm.[141] It is noted that Pt^1-NiCe@SiO_2 has a small Pt–O contribution with CN of 0.5, which is probably due to the interaction between Pt nanoparticles and SiO_2 support in the confined structure.[142–144]

Figure 2.24 depicts the AC-HAADF-STEM images for the reduced $Pt^{0.25}$-NiCe@SiO_2. Many individual bright dots attributed to the Pt single atoms can be discerned on the surface of Ni (200) and Ni (111) with the lattice fringes of 0.17 nm and 0.20 nm, respectively, showing the possible formation of Pt–Ni SAA structure. The singly distributed Pt on NiO before the reduction can maintain its structure after the NiO is reduced.[145] For the high Pt-loaded catalysts (Pt^1-NiCe@SiO_2), the large Pt nanoparticles are still shown after the reduction with lattice fringes of 0.20 nm and 0.22 nm, corresponding to the Pt (200) and Pt (111), respectively (Figure 2.25). It is noted that a superlattice structure can be observed as Ni-Pt $L1_0$ structure with the alternative arrangement of Pt and Ni column by the Z contrast on the edge of the Pt nanoparticles for Pt^1-NiCe@SiO_2.[146] It is possible that Ni species around the Pt nanoparticles can react with Pt at the edge forming Ni-Pt alloys during H_2 reduction.

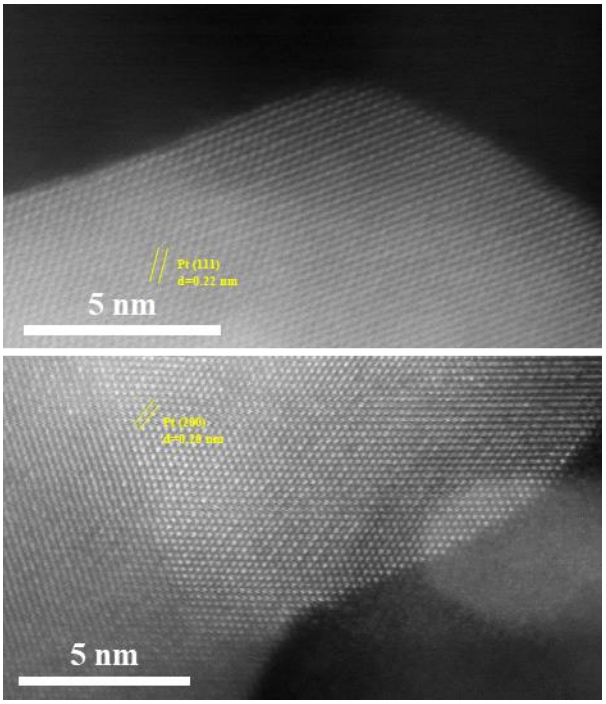

Figure 2.25. AC-HAADF-STEM images of reduced Pt^1-NiCe@SiO$_2$.

The electronic structure of Pt for the reduced Pt$^{0.25}$-NiCe@SiO$_2$ and Pt^1-NiCe@SiO$_2$ is evaluated by XANES and compared with that of the Pt foil and PtO$_2$ references (Figure 2.26a,b). The absorption edge position and white line intensity for both Pt$^{0.25}$-NiCe@SiO$_2$ and Pt^1-NiCe@SiO$_2$ are similar to the Pt foil, indicating that Pt atoms are in metallic state. A linear combination fitting (LCF) applied using the spectra of Pt foil and PtO$_2$ (limited to 20 eV below and 50 eV above the edge jump) suggests that Pt presents primarily in metal state on both catalysts (Table 2.7). However, the SAA structured catalyst (Pt$^{0.25}$-NiCe@SiO$_2$) shows different edge feature as compared to Pt foil or Pt^1-NiCe@SiO$_2$, indicating a different Pt coordination geometry exists on Ni. In addition, the Pt^1-NiCe@SiO$_2$ shows slightly higher white line intensity than the Pt foil with 3.9% of PtO$_2$ in LCF possibly due to the electron transfer between Pt and the SiO$_2$ support.[142,144] Figure 2.26c,d shows the normalized XANES spectra of the reduced NiCe@SiO$_2$, Pt$^{0.25}$-NiCe@SiO$_2$, and Pt^1-NiCe@SiO$_2$ at the Ni K-edge and Ce L$_3$-edge, respectively. The Ni foil, NiO, CeO$_2$, and Ce(NO$_3$)$_3$ samples are analyzed as references. The increased pre-edge

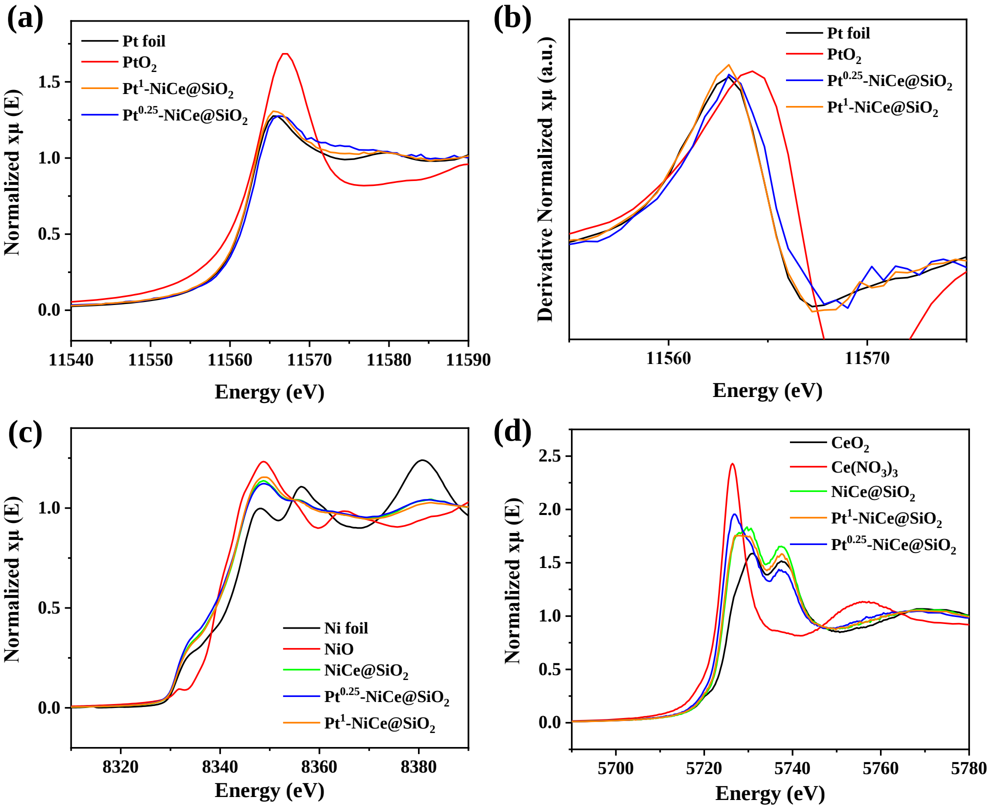

Figure 2.26. (a) Normalized XANES spectra and (b) first-order derivative of the XANES spectra at Pt L_3-edge for reduced $Pt^{0.25}$-NiCe@SiO_2, Pt^1-NiCe@SiO_2, Pt foil, and PtO_2. Normalized XANES spectra at (c) Ni K-edge for reduced NiCe@SiO_2, $Pt^{0.25}$-NiCe@SiO_2, Pt^1-NiCe@SiO_2, Ni foil, and NiO and (d) Ce L_3-edge for NiCe@SiO_2, $Pt^{0.25}$-NiCe@SiO_2, Pt^1-NiCe@SiO_2, CeO_2, and $Ce(NO_3)_3$.

intensity of Ni at 8334 eV and a decreased white line intensity for the $Pt^{0.25}$-NiCe@SiO_2 SAA imply that Ni reducibility is enhanced due to the high Pt–Ni interaction (Figure 2.26c).[147] The LCF of the $Pt^{0.25}$-NiCe@SiO_2 SAA, calculated by using the Ni foil and NiO references, shows the highest Ni^0 proportion of 65.0%, followed by 61.6% and 54.6% for NiCe@SiO_2 and Pt^1-NiCe@SiO_2, respectively. This analysis indicates that less Pt–Ni interaction exists when Pt forms large nanoparticles at the high Pt loadings.

Figure 2.26d shows the normalized XANES spectra of the samples at Ce L_3-edge. The reference spectra exhibit Ce^{4+} oxidation state with a double peak at 5730 eV and 5737 eV, and Ce^{3+} oxidation state with a peak at 5726 eV. All the reduced catalysts show pronounced Ce^{4+}

Table 2.7. Linear combination fitting (LCF) results of the XANES spectra.

Catalysts	Pt L_3-edge		Ni K-edge		Ce L_3-edge	
	Pt^0	Pt^{4+}	Ni^0	Ni^{2+}	Ce^{4+}	Ce^{3+}
Pt^1-NiCe@SiO_2	96.1%	3.9%	54.6%	45.4%	86.8%	13.2%
$Pt^{0.25}$-NiCe@SiO_2	100%	0%	65.0%	35.0%	67.7%	32.3%
NiCe@SiO_2	-	-	61.6%	38.4%	91.4%	8.6%

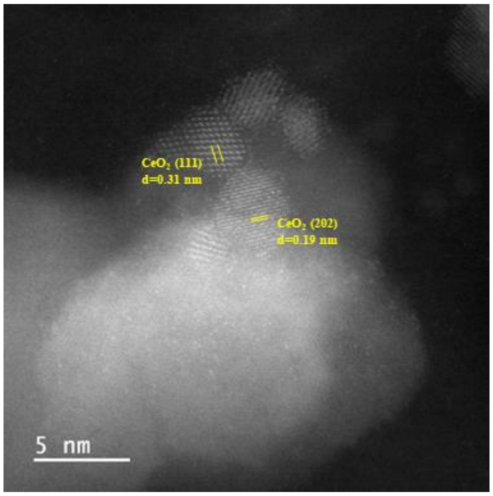

Figure 2.27. AC-HAADF-STEM images of fresh $Pt^{0.25}$-NiCe@SiO_2.

oxidation state, however, the spectrum of $Pt^{0.25}$-NiCe@SiO_2 has features similar to that of $Ce(NO_3)_3$ with a high Ce^{3+} proportion of 32.3% (Table 2.7). It is found that CeO_2 species can interact with Ni, as they are deposited on Ni species, as shown in Figure 2.27. The CeO_2 nanoparticles (~3 nm) with lattice fringes of 0.31 nm and 0.19 nm, assigned to the CeO_2 (111) and CeO_2 (202), respectively, are observed on the Ni nanoparticles. Since $Pt^{0.25}$-NiCe@SiO_2 has well dispersed Pt–Ni SAA structures, the high Ce^{3+} concentration can be derived by the electron transfer from Pt to CeO_2 on the CeO_2 deposited Pt–Ni SAA.[148]

Figure 2.28a,b shows k^2-weighted EXAFS and Fourier transformed EXAFS spectra for the reduced $Pt^{0.25}$-NiCe@SiO_2 and Pt^1-NiCe@SiO_2. The $Pt^{0.25}$-NiCe@SiO_2 has a peak at 2.1 Å (without phase correction), which is located between Pt–O peak (1.6 Å) of PtO_2 and Pt–Pt peak

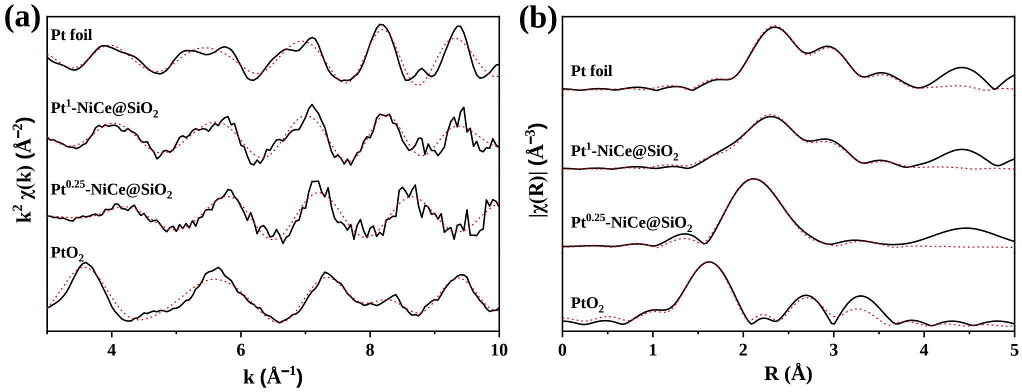

Figure 2.28. k^2-weighted (a) EXAFS functions and (b) Fourier transforms of EXAFS spectra at Pt L_3-edge for reduced $Pt^{0.25}$-NiCe@SiO_2, Pt^1-NiCe@SiO_2, Pt foil, and PtO_2. The fitting data are displayed in dashed lines.

(2.4 Å) of Pt foil, attributed to the Pt–Ni bonds, suggesting the formation of the isolated Pt atoms on Ni nanoparticles. The Pt–Ni interaction is detected in the first-shell at a bond distance of 2.53 Å (Table 2.8), which is in between the Pt–Pt (2.76 Å) and Ni–Ni (2.49 Å) bond lengths and can further support the formation of SAA structures.[149150] The $Pt^{0.25}$-NiCe@SiO_2 does not have any Pt–Pt interaction, indicating the absence of Pt nanoparticles at the low Pt loadings after the reduction. The fitting results demonstrate that Pt–Ni shell has a CN of 5 with a bond distance of 2.53 Å. The low CN is possible, if the atomically dispersed Pt atoms are located at the outermost

Table 2.8. Structural parameters obtained from the EXAFS fittings of the first shell at Pt L_3-edge for reduced $Pt^{0.25}$-NiCe@SiO_2, Pt^1-NiCe@SiO_2, Pt foil, and PtO_2. (CN: coordination number, R: internal atomic distances, ΔE_0: edge-energy shift, σ^2: Debye–Waller factor, R-factor: closeness of the fit)

Samples	Path	CN	R (Å)	ΔE_0 (eV)	σ^2 (10^{-3}Å^2)	R-factor
Pt foil	Pt–Pt	12*	2.76±0.00	7.5±0.5	3.8±0.2	0.004
PtO_2	Pt–O	6*	2.02±0.01	10.5±1.2	1.2±1.6	0.013
Pt^1-NiCe@SiO_2	Pt–Ni	3.5±1.7	2.60±0.01	7.0±1.4	15.9±5.7	0.007
	Pt–Pt	7.4±1.5	2.75±0.01		5.7±1.7	
$Pt^{0.25}$-NiCe@SiO_2	Pt–Ni	5.1±0.6	2.53±0.01	5.5±1.4	6.4±1.1	0.011

layer of Ni nanoparticles without diffusing into the Ni bulk lattice.[151] On the other hand, the shape of Fourier transformed EXAFS function for the Pt^1-NiCe@SiO_2 is similar to that of Pt foil with the Pt–Pt CN and bond distance of 7.4 and 2.75 Å, respectively, which shows the formation of Pt nanoparticles. It is calculated that Pt^1-NiCe@SiO_2 contains Pt–Ni contribution with a CN of 3.5 due to the formation of Ni-Pt $L1_0$ structure during the reduction process evidenced by STEM analysis (Figure 2.25).

The wavelet transforms (WT) of Pt EXAFS is performed for the reduced catalysts by decomposing both *k* and R signals of the EXAFS to identify the contributions of scattering paths.

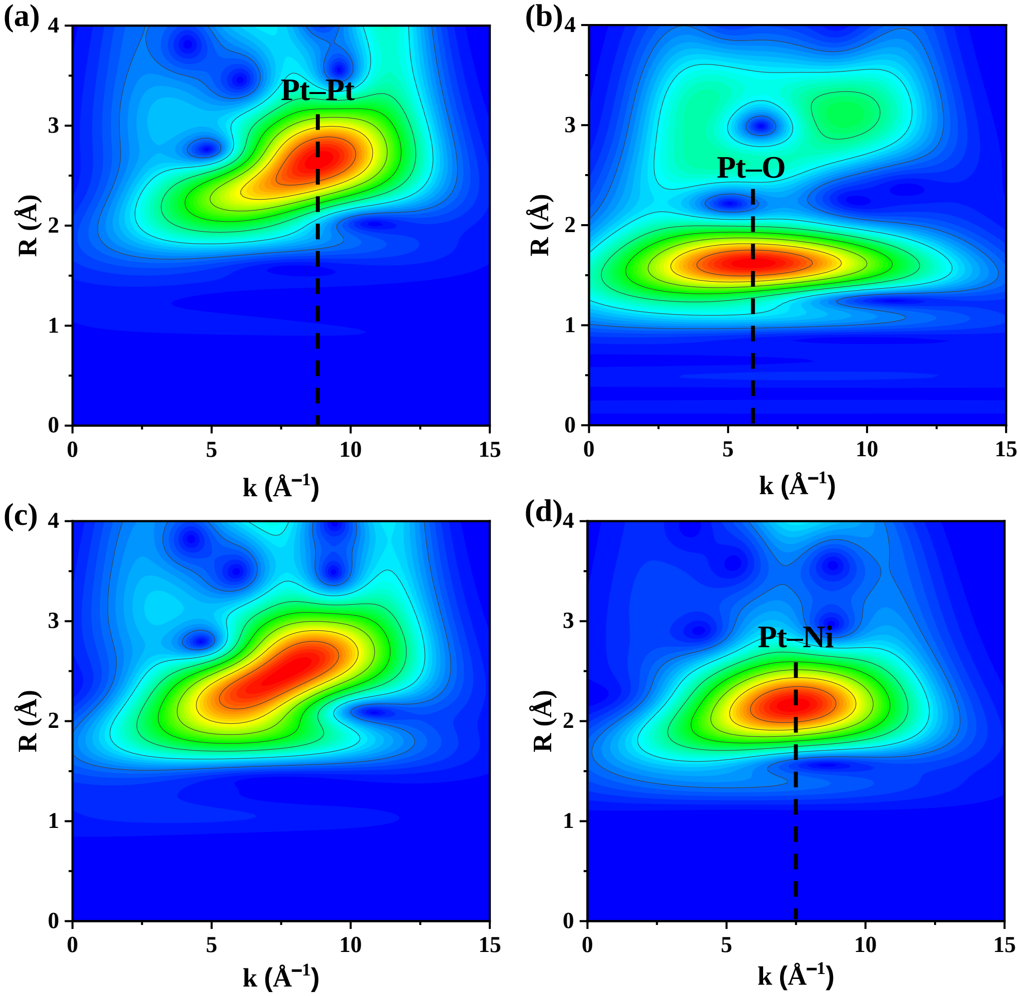

Figure 2.29. Wavelet transform (WT) for the k^2-weighted EXAFS signals of (a) Pt foil, (b) PtO_2, (c) Pt^1-NiCe@SiO_2, and (d) $Pt^{0.25}$-NiCe@SiO_2.

As it can be seen in Figure 2.29, the WT contour plots of Pt foil and PtO_2 references has the intensity maxima at 8.8 $Å^{-1}$ and 5.9 $Å^{-1}$, ascribing to the Pt–Pt and Pt–O contributions, respectively. The $Pt^{0.25}$-NiCe@SiO_2 SAA shows only one intensity maximum at 7.4 $Å^{-1}$, owing to the Pt–Ni contribution without no distinct features at higher *k* values, resulting from the atomically dispersed Pt atoms on the Ni surface.[152] The WT plots of the reduced Pt^1-NiCe@SiO_2 contains both Pt–Pt and Pt–Ni contributions, matching with the STEM and EXAFS analysis.

As shown in Figure 2.16c,d, the Pt^x-NiCe@SiO_2 catalysts exhibit nearly identical CO_2 and CH_4 conversions of 11.5% and 6.5%, respectively, over 20 h TOS. Finally, long-term stability tests are performed over 120 h TOS for the Pt^1-NiCe@SiO_2, $Pt^{0.25}$-NiCe@SiO_2, and NiCe@SiO_2 catalysts, as shown in Figure 2.30. Among the catalysts tested, $Pt^{0.25}$-NiCe@SiO_2 shows the most stable DRM activity over 120 h TOS, whereas the other catalyst beds are blocked at around 50 h TOS due to the carbon formation. Our results imply that amount of Pt does not influence the conversion rate of the yolk–shell catalysts, but the catalyst stability can be improved by minimizing the carbon formation at a certain Pt concentration, i.e., $Pt^{0.25}$-

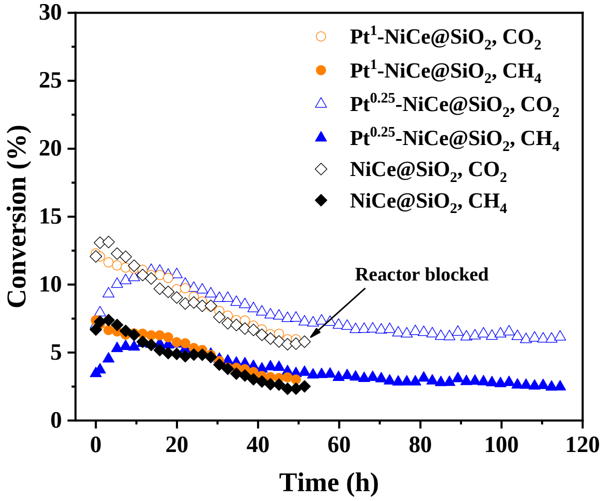

Figure 2.30. Long-term stability of Pt^1-NiCe@SiO_2, $Pt^{0.25}$-NiCe@SiO_2, and NiCe@SiO_2 over 120 h TOS under DRM at 500 °C.

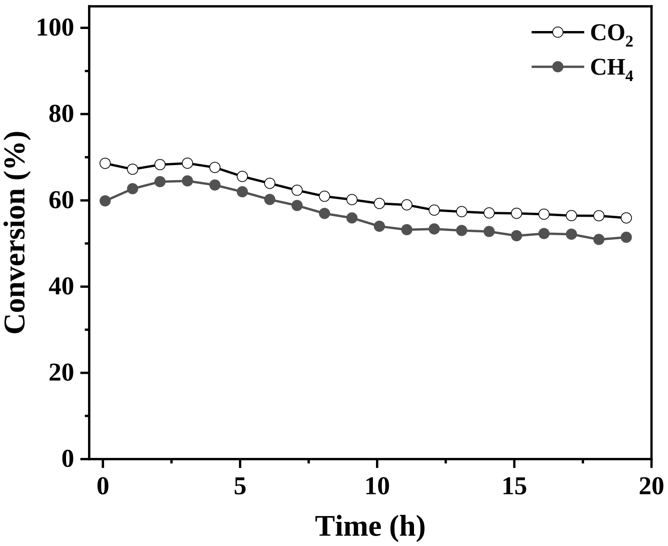

Figure 2.31. CO_2 and CH_4 conversion of $Pt^{0.25}$-NiCe@SiO_2 under DRM at 750 °C.

NiCe@SiO_2. Additionally, the DRM activity of the $Pt^{0.25}$-NiCe@SiO_2 SAA catalyst was tested at 750 °C for 20 h, as shown in Figure 2.31 and Table 2.5. The catalyst shows high initial CO_2 and CH_4 conversions of 68.6% and 64.5% with H_2 and CO yields of 54.9% and 64.1%, respectively. The activity decreases by 18% and 14% for CO_2 and CH_4 over 20 h TOS, respectively. However, there is no significant conversion drop during the reaction. The catalysts bed also is not blocked by severe carbon deposition. These results imply that the yolk–shell SAA presents good stability against the CO disproportionation reaction at high CO_2 and CH_4 conversions.

2.3.4 Kinetic studies

Kinetics experiments are performed to determine reaction order and activation energy for the best performing catalyst, i.e., $Pt^{0.25}$-NiCe@SiO_2, under differential conditions at 500 °C. The effect of the partial pressures of CO_2 and CH_4 on the consumption rate of reactants is depicted in Figure 2.32. The reaction rate is expressed by the following semi-empirical power-law rate equations for $Pt^{0.25}$-NiCe@SiO_2.

$$R_{CH4} = k_1(PCH_4)^{0.60}(PCO_2)^{-0.55} \qquad (2.6)$$

$$R_{CO2} = k_2(PCH_4)^{0.34}(PCO_2)^{-0.22} \qquad (2.7)$$

According to Eq. (2.6), the forward CH_4 reaction rate is proportional to P_{CH4} with the reaction order of 0.60, while the reaction order with respect to CO_2 is −0.55, suggesting that CO_2 adsorbs more strongly than CH_4. A negative reaction order with respect to CO_2 partial pressure is reported, when the catalyst shows high resistance to coking.[153–155] The increased surface coverage of oxygen species originated from CO_2 dissociation can block the sites for CO_2 adsorption. The high surface coverage of oxygen species can minimize coke formation as oxygen species react with the surface carbon.[154,155] We observe facile re-oxidation of the Ni species by feeding CO_2 in the *in-situ* DRIFTS experiments, which is discussed in Section 2.3.5. The apparent CH_4, CO_2, H_2, and CO activation energies are measured within the temperature range of

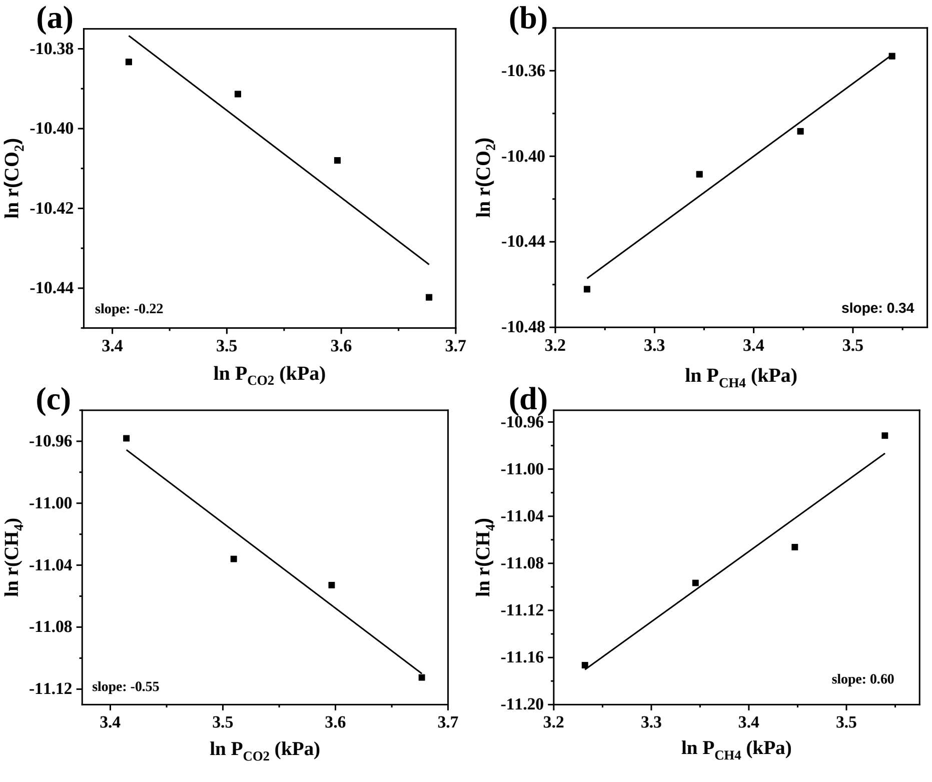

Figure 2.32. Reaction rates for the consumption of (a,b) CO_2 and (c,d) CH_4 as a function of the CO_2 and CH_4 partial pressures for $Pt^{0.25}$-NiCe@SiO_2 at 500 °C.

Table 2.9. Apparent activation energies ($E_{a,app}$) for $Pt^{0.25}$-NiCe@SiO_2 under DRM.

	$E_{a,app}$ (kJ mol^{-1})
CH_4	99.01
CO_2	79.87
H_2	120.40
CO	86.65

450–510 °C based on the consumption rates of CH_4 and CO_2 and formation rates of CO and H_2 (Table 2.9). The Arrhenius plots are presented in Figure 2.33. The CH_4 activation energy (99.0 kJ mol^{-1}) is higher than the CO_2 activation energy (79.9 kJ mol^{-1}), matching well with the literature. The activation energy for H_2 formation is 120.4 kJ/mol, which is greater than that of CO formation of 86.7 kJ mol^{-1} due to the RWGS reaction.[92,94,156–158]

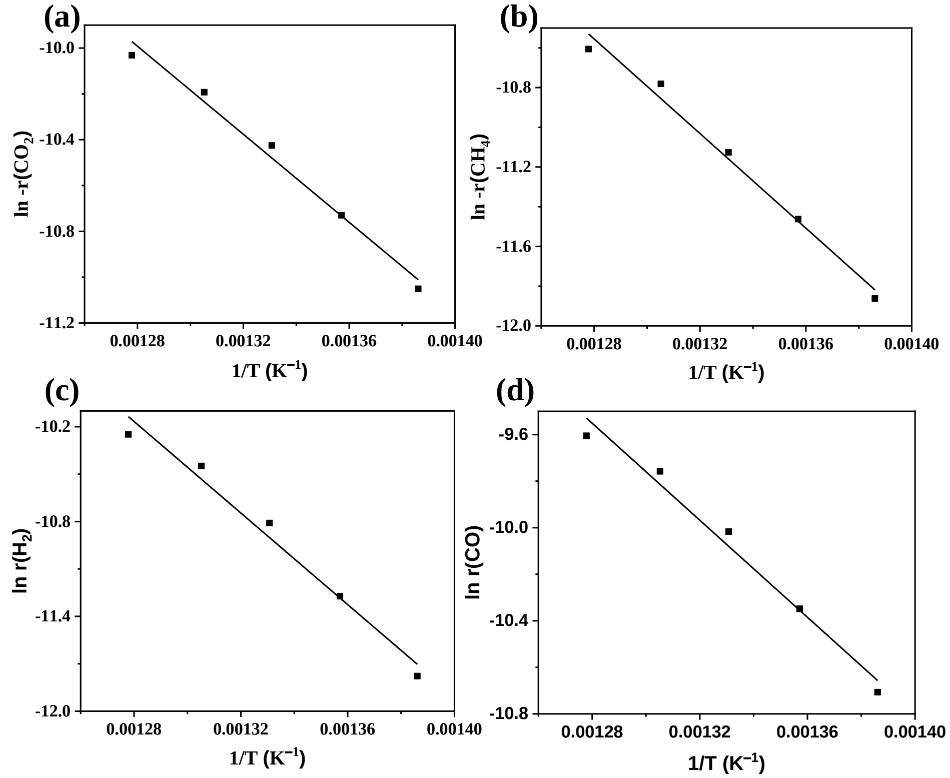

Figure 2.33. Arrhenius plots for reaction rates of (a) CO_2, (b) CH_4, (c) H_2, and (d) CO on $Pt^{0.25}$-NiCe@SiO_2.

The inhibition effect with respect to P_{CO2} can be associated with the competitive occupancy of active sites by the CO_2 species.[159] It is reported that inert SiO_2-supported metal catalysts follow the mono-functional pathway, in which both CO_2 and CH_4 are activated on the metal.[64] The CO_2 reaction rate increases with CH_4 partial pressure from DRM due to the facile adsorption of CH_4 on the surface, followed by its dissociation (Eq. (2.7)). Dissociation of CH_4 in DRM can produce H_2, which can react with CO_2 in RWGS reaction leading to an increase in the CO_2 reaction rate.[160] In contrast, the CO_2 reaction rate decreases with increasing CO_2 partial pressure. This can be attributed to the change in reaction mechanism, where at low CO_2 partial pressure, not only DRM but also the RWGS reaction is favored by H* from CH_4 decomposition, while CO_2 reacts with CH_4 by DRM at high CO_2 partial pressure.

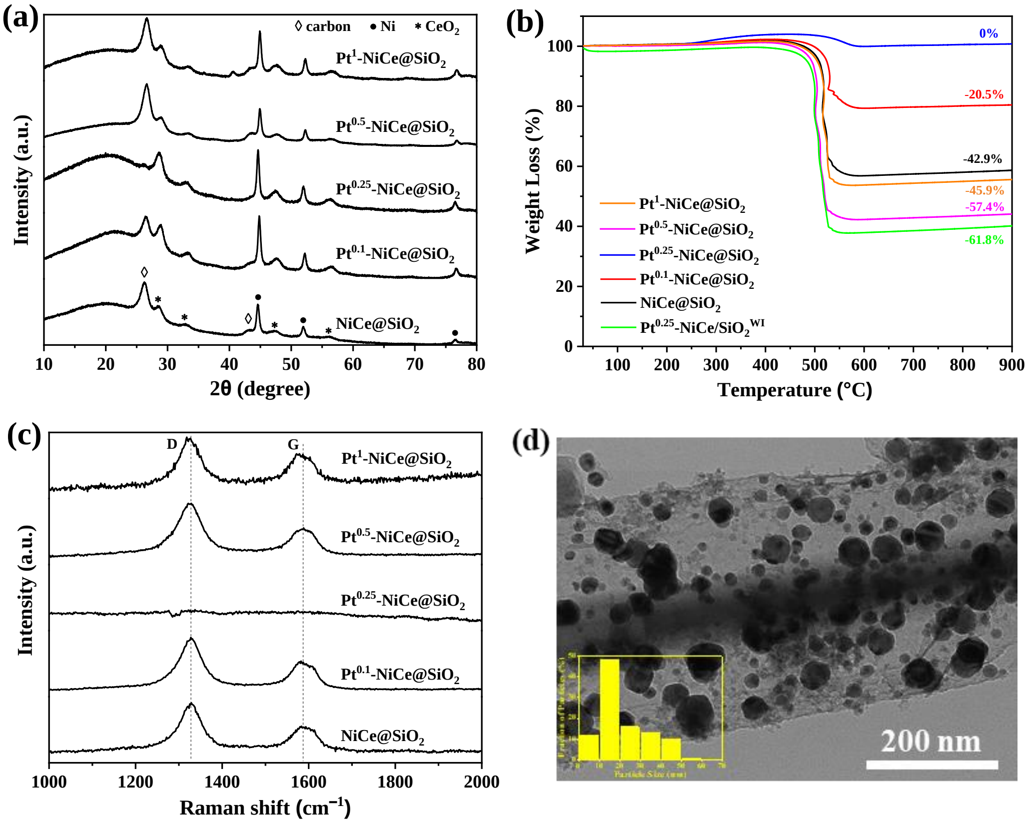

Figure 2.34. (a) XRD patterns, (b) TGA profiles, and (c) Raman spectra of spent Pt^x-$NiCe@SiO_2$ after 20 h of DRM and (d) TEM image of spent $Pt^{0.25}$-$NiCe@SiO_2$ after 20 h of DRM.

2.3.5 Carbon deposition

The spent yolk–shell catalysts loaded with different wt% of Pt are analyzed using XRD, TGA, and Raman spectroscopy to investigate carbon formation during DRM. As shown in Figure 2.34a, all the spent yolk–shell catalysts show diffraction peaks of metallic Ni and CeO_2, indicating no oxidation has occurred. A Pt diffraction peak is also visible, especially at high Pt loadings, and shows a shift compared to the fresh ones indicating the formation of the Pt–Ni alloy structures. The spent yolk–shell catalysts except $Pt^{0.25}$-NiCe@SiO_2 show diffraction peaks at 2θ of 26.6° and 43.5° corresponding to graphitic carbon. These carbon formations are more pronounced on the spent impregnated catalysts. As shown in Figure 2.35, the spent $Pt^{0.25}$-NiCe/SiO_2^{WI} shows strong carbon diffraction peaks, making it difficult to analyze the other metal species.

TGA is performed to quantify the amount of carbon formed on the spent yolk–shell catalysts and $Pt^{0.25}$-NiCe/SiO_2^{WI}, as shown in Figure 2.34b and Table 2.10. The weight of the spent yolk–shell catalysts slightly increases starting from 250 °C due to oxidation of the catalysts

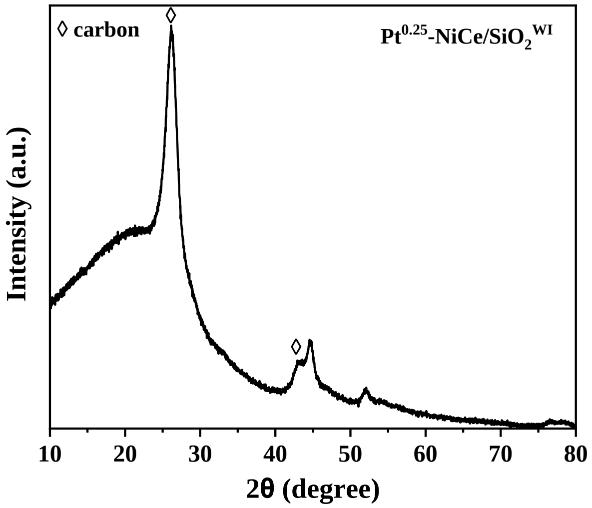

Figure 2.35. XRD pattern of spent $Pt^{0.25}$-NiCe/SiO_2^{WI} after 20 h of DRM.

Table 2.10. Deposited carbon amount and I_D/I_G ratios calculated for Pt^x-NiCe@SiO_2 and $P^{t0.25}$-NiCe/SiO_2^{WI} after 20 h of DRM.

Catalysts	Deposited carbon (mg g_{cat}^{-1})^a	I_D/I_G^b
Pt^1-NiCe@SiO_2	0.44	0.80
$Pt^{0.5}$-NiCe@SiO_2	0.56	1.00
$Pt^{0.25}$-NiCe@SiO_2	0	-
$Pt^{0.1}$-NiCe@SiO_2	0.20	0.89
NiCe@SiO_2	0.41	0.82
$Pt^{0.25}$-NiCe/SiO_2^{WI}	0.62	-

by air. Generally, a dramatic weight loss is observed on the spent catalysts at the temperature region of 400–600 °C, which is attributed to gasification of filamentous or graphitic carbon deposited during the DRM.[64] The amount of carbon formed during the DRM is calculated to be 0.41 mg g_{cat}^{-1} for NiCe@SiO_2, which decreases to 0.20 mg g_{cat}^{-1} after 0.1 wt% Pt promotion. Further promotion of the catalyst with 0.25 wt% Pt indicates that carbon accumulation is negligible, which is in good agreement with the XRD analysis. When the Pt loading exceeds 0.5 wt%, a significant weight loss occurs again due to the carbon formation during the DRM. The $Pt^{0.25}$-NiCe/SiO_2^{WI} contains the largest amount of carbon deposition of 0.62 mg g_{cat}^{-1} showing that the impregnated catalysts are the least resistant to the carbon deposition despite the Pt promotion.

The Raman spectra of the spent Pt^x-NiCe@SiO_2 are collected to determine the nature of carbon, as shown in Figure 2.34c. Two vibrational peaks centered at 1327 cm^{-1} and 1587 cm^{-1} are observed for all the spent yolk–shell catalysts except for $Pt^{0.25}$-NiCe@SiO_2. The former peak is assigned to the D band associated with the disordered defective carbon correlating with amorphous carbon structures, while the latter peak is the G band belonging to the ordered and well-graphitized carbon structures. The integrated intensity ratio of D band to G band (I_D/I_G) is calculated to compare fractions of the disordered and ordered carbons, as shown in Table 2.10. NiCe@SiO_2 exhibits I_D/I_G ratio of 0.82, and the value reaches unity for 0.5 wt% Pt promotion. Further promotion of the catalyst with 1 wt% Pt decreases I_D/I_G ratio to 0.8. The lack of a carbon peak on $Pt^{0.25}$-NiCe@SiO_2 might be explained by the disordered carbon formed mainly on the catalyst, which can be removed easily during DRM.[107,161]

The XRD, TGA, and Raman data for the spent catalysts indicate that $Pt^{0.25}$-NiCe@SiO_2 shows the highest resistance to carbon deposition during DRM. No significant carbon formation is observed in the TEM image of the spent $Pt^{0.25}$-NiCe@SiO_2 after 20 h TOS at 500 °C (Figure 2.34d). In addition, its nanotubular yolk–shell structure remains stable without showing any degree of destruction. Our results show that the percentage of yolks having size of 0–10 nm decreases from 31% to 12% after the 20 h of DRM reaction, while the percentage of 10–20 nm sized yolks increases from 28% to 48% (inset graph of Figure 2.1a and Figure 2.34d). Similarly, the percentage of 20–30 nm sized yolks decreases from 24% to 16% after the reaction, and this change matches with the increased percentage of 30–50 nm sized yolks. These results indicate that yolks can sinter during the reaction, which could be the reason for decrease in CO_2 and CH_4 conversions by 21.6% and 33.6%, respectively (Figure 2.16). In addition, the XRD patterns of the reduced and spent for $Pt^{0.25}$-NiCe@SiO_2 (Figure 2.9b) show that the Pt peaks are not observed before the reaction due to the singly distributed Pt, whereas the spent catalyst shows a very small hump, which could be attributed to the sintered Pt–Ni structure. However, the average yolk size of the spent $Pt^{0.25}$-NiCe@SiO_2 (24.4 nm) are similar to those of the reduced catalyst (Figure 2.1a), suggesting that SiO_2 encapsulation limits sintering and provides a strong metal–support interaction. The positive effect of SiO_2 encapsulation can also be observed in the crystallite size of Ni (Table 2.1 and Table 2.11). The crystallite size of active Ni for the reduced

Table 2.11. Crystallite size for fresh and spent Pt^{x}-NiCe@SiO$_2$ after 20 h of DRM.

Catalysts		Crystallite size (nm)[a]			
		NiO	Ni	CeO$_2$	Pt
Fresh	Pt^{1}-NiCe@SiO$_2$	14.94	-	6.25	12.35
	Pt$^{0.5}$-NiCe@SiO$_2$	15.12	-	5.93	7.43
	Pt$^{0.25}$-NiCe@SiO$_2$	15.73	-	5.71	5.44
	Pt$^{0.1}$-NiCe@SiO$_2$	13.44	-	6.60	-
	NiCe@SiO$_2$	15.99	-	6.58	-
Spent	Pt^{1}-NiCe@SiO$_2$	-	17.40	6.11	12.00
	Pt$^{0.5}$-NiCe@SiO$_2$	-	17.37	5.97	-
	Pt$^{0.25}$-NiCe@SiO$_2$	-	17.29	5.97	-
	Pt$^{0.1}$-NiCe@SiO$_2$	-	18.56	6.43	-
	NiCe@SiO$_2$	-	17.71	6.09	-

(16.25 nm) and spent (17.29 nm) Pt$^{0.25}$-NiCe@SiO$_2$ remains similar. Finally, the structure of Pt$^{0.25}$-NiCe@SiO$_2$ SAA after the 20 h of DRM reaction at 500 °C is analyzed by AC-HAADF-STEM and EXAFS analysis (Figure 2.36 and Figure 2.37). The presence of bright dots for the

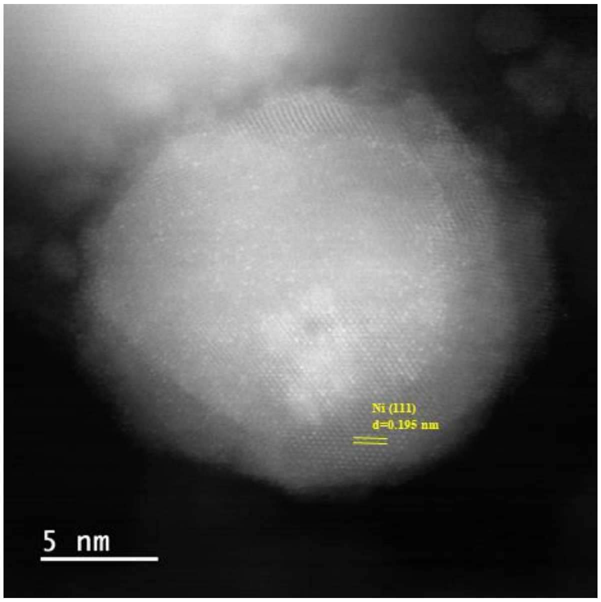

Figure 2.36. AC-HAADF-STEM images of spent Pt$^{0.25}$-NiCe@SiO$_2$ after 20 h of DRM at 500 °C.

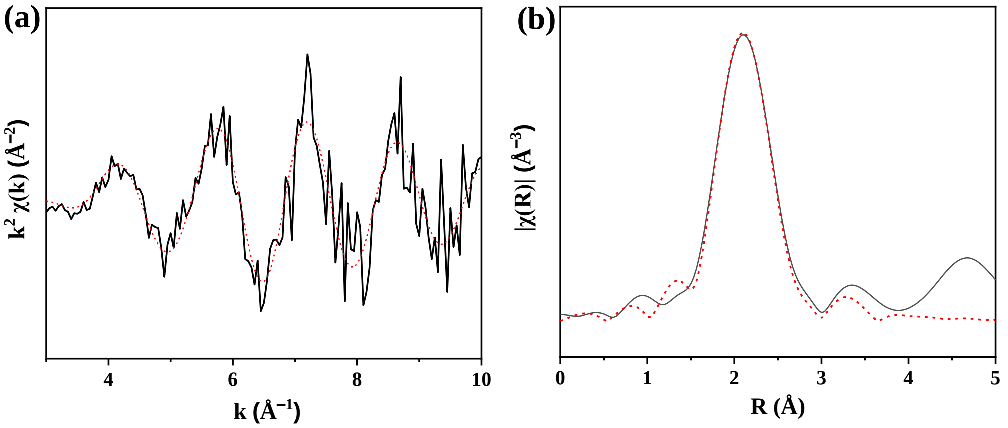

Figure 2.37. k^2-weighted (a) EXAFS spectrum and (b) Fourier transforms of EXAFS spectra at Pt L_3-edge for spent $Pt^{0.25}$-NiCe@SiO_2 after 20 h of DRM at 500 °C.

isolated Pt atoms on Ni in STEM image and showing only one peak at 2.52 Å for the Pt–Ni contribution with CN number of ~7 in EXAFS fitting result (Table 2.12) indicate that the Pt–Ni SAA structure remains after the DRM reaction, providing the stability of the SAA structure. Overall, the developed $Pt^{0.25}$-NiCe@SiO_2 exhibits similar activity and longer stability by minimizing carbon formation compared to the studies reported at low DRM temperatures.[92,93,162,163]

Table 2.12. Structural parameters obtained from the EXAFS fittings of the first shell at Pt L_3-edge for spent $Pt^{0.25}$-NiCe@SiO_2 after 20 h of DRM at 500 °C. (CN: coordination number, R: internal atomic distances, ΔE_0: edge-energy shift, σ^2: Debye–Waller factor, R-factor: closeness of the fit)

Path	CN	R (Å)	ΔE_0 (eV)	σ^2 (10^{-3}Å^2)	R-factor
Pt–Ni	7.33±0.82	2.52±0.01	3.4±1.2	8.8±1.0	0.009

2.3.6 *In situ* and *operando* DRIFTS

To provide a mechanistic understanding for the DRM activity of the yolk–shell and impregnated catalysts with and without 0.25 wt% Pt promotion, *in situ* and *operando* DRIFTS experiments are conducted. First, only CO_2 gas is injected into the DRIFT cell after H_2 reduction of the catalyst, and the temporal activity of the catalyst is recorded for 20 min. As shown in

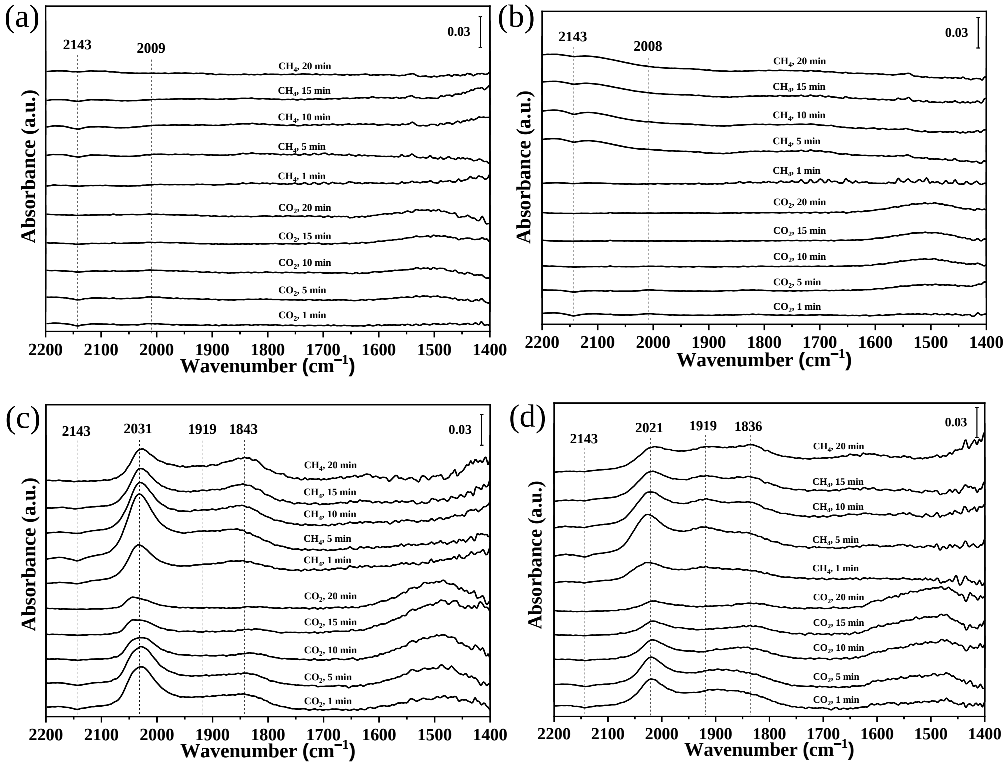

Figure 2.38. Time-resolved in situ DRIFTS spectra in CO_2 (CO_2:N_2=1:6) and CH_4 (CH_4:N_2=1:6) stream at 500 °C for (a) $Pt^{0.25}$-NiCe@SiO_2, (b) NiCe@SiO_2, (c) $Pt^{0.25}$-NiCe/SiO_2^{WI}, and (d) NiCe/SiO_2^{WI}.

Figure 2.38, the Fourier-transform infrared (FTIR) spectra of the catalysts show the gaseous (2143 cm^{-1}) and adsorbed (1730–2080 cm^{-1}) CO bands along with the characteristic IR bands for carbonate (CO_3^{2-}*) species located at 1410–1653 cm^{-1} in CO_2 stream. As shown in Figure 8c, $Pt^{0.25}$-NiCe/SiO_2^{WI} shows a strong CO* band for linearly adsorbed CO on the reduced metal sites at 2029 cm^{-1}, and broad CO* bands at 1919 cm^{-1} and 1844 cm^{-1} for the bridge and multi-centered bonded CO, respectively. The adsorbed CO_2 dissociates to CO* and O* species on Ni, where CO* desorbs subsequently as CO gas. Vibrational CO* bands are immediately visible upon CO_2 injection on the impregnated catalysts, yet their intensities decrease after 10 min. Similarly, the doublet of gaseous CO can be observed only for the first 10 min. It is possible that O* species formed during CO_2 injection can oxidize reduced Ni leading to its deactivation. As a result, the CO* coverage on Ni decreases on the surface and limits CO production. Additionally, CO_3^{2-}* species can form through the reaction of CO_2* and O* on CeO_2. As shown in Figure 8, the CO_3^{2-}* bands develop after CO_2 injection on both impregnated and yolk-shell catalysts, yet their intensity is much stronger on the impregnated catalysts. A clear difference between the yolk–shell and impregnated catalysts is shown in CO absorption bands. Unlike impregnated catalysts, the yolk–shell catalysts show a weak linear CO absorption band at 2011 cm^{-1}, while bridge CO bands are not observed (Figure 2.38a,b). Like impregnated catalysts, the gaseous CO and small linearly adsorbed CO peaks are not seen after 10 min of CO_2 stream due to the possible Ni oxidation.

Following CO_2 injection, CH_4 is introduced after flushing the cell with N_2 for 1 h. The linear and bridge CO absorption bands are still observed for the impregnated catalyst, whereas only a weak linear CO absorption band is identified for the yolk–shell catalysts during CH_4 injection. The CO_3^{2-}* peaks are not observable throughout the CH_4 feed stream. The presence of CO* bands at 1 min of CH_4 stream on the impregnated catalysts can imply that the adsorbed CO formed during CO_2 injection does not react with CH_4. The gaseous CO appears upon CH_4 injection at 1 min, because the CO_3^{2-}* species formed during CO_2 injection can react with H* to generate formate species (COOH*) followed by their decomposition to CO.[164] The gaseous and adsorbed CO peaks continue to increase for the first 5 min of CH_4 injection and start to decrease after 10 min for the impregnated catalysts. The initial increase of CO bands can be explained with the reaction between the decomposed carbon from CH_4 and reactive lattice oxygen. Once the reactive lattice oxygen is consumed, further decomposition of CH_4 blocks the active sites with carbon, reducing the intensity of CO bands.[64] The yolk–shell catalyst does not have any gaseous and adsorbed CO bands at 1 min CH_4 stream due to the low amount of carbonate species

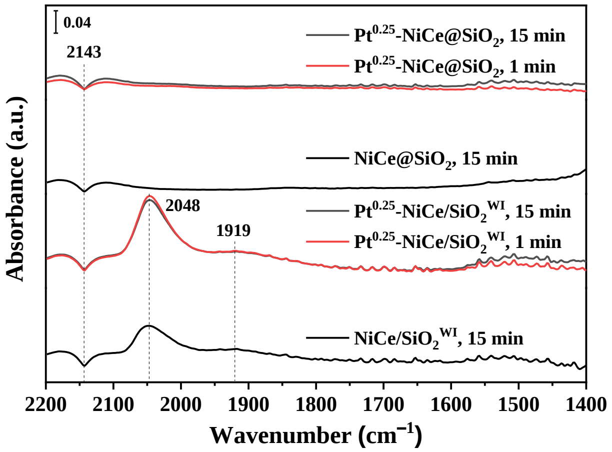

Figure 2.39. Operando DRIFTS spectra of yolk–shell and impregnated catalysts with and without 0.25 wt% Pt promotion in DRM condition (CO_2:CH_4:N_2=1:1:6) at 500 °C.

formed during CO_2 injection. However, the gaseous CO band observed after 5 min remains up to 20 min of CH_4 stream indicating that yolk–shell catalysts present high resistance to carbon deposition, matching with DRM activity data.

Lastly, *operando* DRIFTS experiment is performed at 500 °C. As shown in Figure 2.39, the FTIR spectra of all catalysts show the doublet of gaseous CO (2143 cm^{-1}) produced from DRM. Similar to the *in situ* DRIFTS experiments, impregnated catalysts show absorption bands for linear- and bridge-bonded CO, whereas CO absorption bands are not pronounced on the yolk–shell catalysts. During DRM, carbon is formed through methane decomposition ($CH_4 \rightarrow C+2H_2$, $\Delta H°= +74.9$ kJ mol^{-1}) and CO disproportionation (the Boudouard reaction), and the latter reaction is dominant at the relatively low reaction temperature (e.g. 500 °C). The lack of CO absorption bands on the yolk–shell catalysts implies that carbon formation on the active sites through the Boudouard reaction might not occur.[47,64,165] In comparison to CO_2 injection experiments, the linearly adsorbed CO band is shifted to 2048 cm^{-1} from 2029 cm^{-1} during DRM due to the increase in the dipole-dipole coupling between the CO* molecules.[93,166] It is important

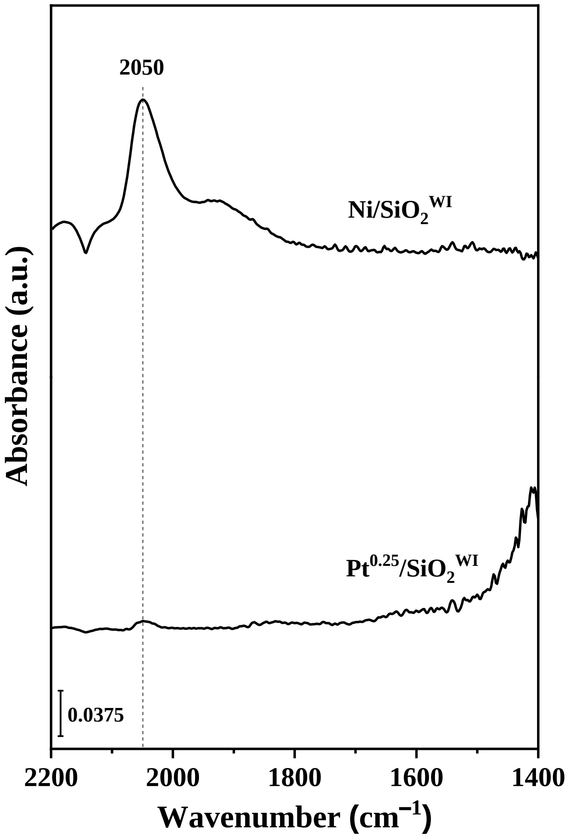

Figure 2.40. DRIFTS spectra of Ni/SiO_2^{WI} and $Pt^{0.25}$/SiO_2^{WI} during DRM condition ($CO_2/CH_4/N_2$=1/1/6).

to note that linearly adsorbed CO bands on Ni and Pt cannot be differentiated from each other. As shown in Figure 2.40, the linearly adsorbed CO band on both Ni and Pt are detected at the same wavenumber (2050 cm^{-1}) for Ni/SiO_2^{WI} and $Pt^{0.25}$/SiO_2^{WI} under DRM condition, which is in agreement with the literature.[127,167] Compared to the CO_2 and CH_4 injection experiments, the gaseous and adsorbed CO bands do not diminish during the *operando* experiments suggesting that feeding CO_2 and CH_4 simultaneously can stabilize the catalyst by inhibiting Ni oxidation or carbon deposition due to facile interaction among the intermediates. Based on the experimental data analysis, elementary steps of the DRM reaction mechanism can be summarized in Figure 2.41. Both CH_4 and CO_2 are activated on the Pt–Ni SAA structures which are in interaction with

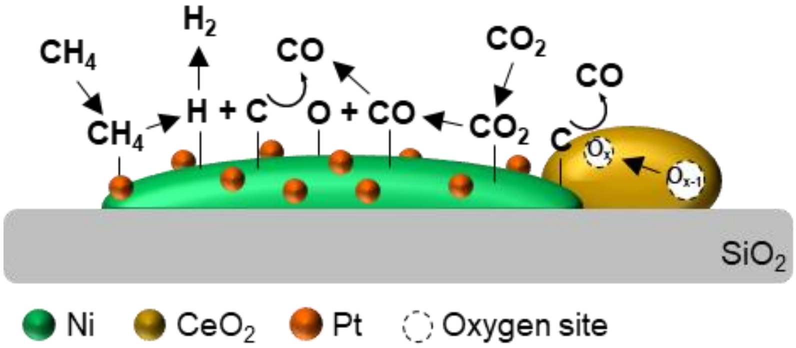

Figure 2.41. Reaction mechanism for DRM on yolk–shell $Pt^{0.25}$-NiCe@SiO_2 SAA catalyst.

CeO_2 and supported on SiO_2 shell. CH_4 (g) adsorbs on the Pt–Ni and Ni sites and dissociates to CH_x intermediates to form C* and H* species (eq. 2.8). H* species react on the Ni to form H_2 (g) (eq. 2.9). CO_2 adsorbs on the Ni site and dissociate to form CO (g) and O* (eq. 2.10 and eq. 2.11).[64] CO is produced from the reaction between O* formed on the Pt–Ni and Ni sites, and C* (eq. 2.12). The high mobility of lattice oxygen in CeO_2 can play an important role for carbon removal reaction. The oxygen sites (O_x) on CeO_2 can convert C* by forming CO* at the interface between Ni and CeO_2, leaving O_{x-1} vacancy. For the confined morphology of the yolk–shell, CO* on Ni can easily desorb as CO (g) (eq. 2.11) rather than forming surface carbon through the CO disproportionation reaction (eq. 2.13). Pt single atoms can inhibit carbon generation by increasing the energy barrier for subsequent CH_x dissociation (eq. 2.8). The overall mechanism can be more pronounced on the well dispersed Pt single atoms interacting with Ni, e.g. 0.1 wt% and 0.25 wt% Pt promotions. The yolk–shell catalysts without Pt promotion or with high Pt promotion (> 0.25 wt%) generate more amount of carbon due to the lack of Pt–Ni SAA structures.

$$CH_4^* \leftrightarrow CH_x^* + H^* \leftrightarrow C^* + H^* \qquad (2.8)$$

$$2H^* \leftrightarrow H_2\ (g) \qquad (2.9)$$

$$CO_2^* \leftrightarrow CO^* + O^* \qquad (2.10)$$

$CO^* \leftrightarrow CO\ (g)$ (2.11)

$C^* + O^* \leftrightarrow CO^*$ (2.12)

$2CO \leftrightarrow C + CO_2$ (2.13)

The RWGS reaction occurs during DRM by activation of CO_2^* with H* to generate OH* followed by reaction between OH* and H* to generate H_2O gas (eq. 2.14 and eq. 2.15).

$CO_2^* + H^* \leftrightarrow COOH^* \leftrightarrow CO^* + OH^*$ (2.14)

$OH^* + H^* \leftrightarrow H_2O$ (2.15)

2.4 Discussion

Our results confirm that the yolk–shell catalysts exhibit higher resistance to carbon deposition compared to the conventional ones during DRM. The cavity inside the shell can be beneficial for rapid chemical diffusion and conversion, which facilitates the gasification of carbon intermediates. The two-dimensional-confined cavity can disperse active metals as well as enhance adsorption and mass transfer of reactants.[132] Addition of Pt can lead to the formation of Pt–Ni alloy structures, which can promote carbon oxidation while suppressing Ni oxidation on the surface by forming Pt-rich metal surfaces.[127,149,168] The Pt-dominant bimetallic surface can weaken the O binding energy and reduce carbon oligomerization, thereby enhancing the DRM activity and stability.[169] Particularly, promotion of active metals with low Pt concentrations (< 1 wt%) can prevent carbon formation in methane reforming reactions due to the strong metal–support interaction, high Pt dispersion, and enhanced coke gasification.[106,130,170,171] A specific amount of Pt promotion might be necessary to keep the desired Pt concentration on the Ni surface, while minimizing the formation of Pt nanoclusters or nanoparticles. In our work, we report that carbon formation can be minimized at certain low Pt concentrations, i.e., 0.25 wt%, with a positive effect of confined space in the yolk–shell structures. We observe that promotion of NiCe@SiO_2 with 0.25 wt% Pt can form Pt–Ni SAA structures, which increase Pt–Ni interaction and the reducibility of Ni species, as shown in the HRTEM and H_2-TPR analysis. Pt has low segregation energy, and it can remain on the Ni surface forming SAA structures.[120] When the Pt–Ni SAAs formed, it is shown that the SAAs can maintain a high activation energy for CH_x dehydrogenation and increase carbon gasification rate compared to monometallic catalysts.[111–114] Additionally, singly dispersed Pt can effectively dissociate H_2 followed by its spillover on to the Ni surface.[172,173] These highly reactive H atoms can hydrogenate adsorbed carbon species, which hinders the nickel carbide formation while minimizing the carbon dissolution into the Ni lattice.[174] When Pt concentration increases from 0.25 wt% to 1 wt%, Pt nanoparticles are observed in the yolks, as shown in Figure S3 and S4. Formation of Pt nanoparticles at high Pt loadings can facilitate dehydrogenation of $CH_{4,}$ enabling oligomerization of C–H species to form coke.[175]

In situ and *operando* DRIFTs experiments do not confirm directly whether intermediate CO* is reacting fast to form other surface adsorbed species or released from the surface as CO gas on the yolk–shell structures. It has been reported that CO binds weekly on single Pt atoms in SAAs that can impede the Boudouard reaction preventing carbon formation on the catalyst.[176] However, our results indicate that the linear- or bridge-bonded CO is not directly associated with Pt promotion; instead it is related to the confined morphology of the yolk–shell structures. It is possible that the adsorption energy of CO can be influenced by surface deformations in the confined morphology. Strain effects induced from the lattice mismatch between yolks and shell materials can affect the electronic property, producing a shift of the surface d-band states of the transition metals.[177] A change in electron density of the confined Ni strongly interacting with

SiO_2 shell can change CO adsorption behavior having CO species to be easily released from the surface.[47] As shown in Table 2.5, the yolk–shell catalysts produce less H_2/CO ratio than the impregnated catalysts, possibly due to the efficient release of CO species.[178] In addition, the CO* absorption band observed on the Ni active sites can influence CH_4 activation. As shown in Figure S15, a decrease in the CH_4 conversion rate for the impregnated catalyst is faster than that for the yolk–shell catalysts, which might indicate that the active sites for CH_4 is blocked by CO* from the mono-functional pathway.[179]

2.5 Conclusions

In this work, we have evaluated the low-temperature DRM performance of the nanotubular yolk–shell structured Pt-NiCe@SiO_2 at 500 °C. The developed Pt-NiCe@SiO_2 exhibits high resistance to carbon deposition in the confined morphology due to the efficient CO desorption, whereas the conventional impregnated catalyst deactivates fast by severe carbon formation through favorable Boudouard reaction during DRM. The $Pt^{0.25}$-NiCe@SiO_2 catalyst presents atomically dispersed Pt on the yolks forming Pt–Ni SAA structures encapsulated by a nanotubular SiO_2 shell. The Pt–Ni SAA facilitates Pt–Ni interaction and enhances the reducibility of Ni species, which further suppresses carbon formation during DRM. When the Pt loading increases above 0.25 wt%, Pt nanoclusters form leading to oligomerization of C–H species to form coke. Promotional effects of both confined morphology and Pt–Ni SAA structures can lower the operating temperature of DRM without showing any catalyst deactivation. These discoveries highlight the potential routes to design catalysts for industrially relevant DRM process to utilize GHGs to produce syngas, which can contribute to carbon neutrality.

CHAPTER 3

Direct CO_2 Hydrogenation to Light Olefins over Tandem Catalysts

3.1 Introduction

High atmospheric CO_2 concentration contributes to global warming and ocean acidification.[7] Activation of CO_2 to high value-added chemicals and fuels is a promising route to mitigate CO_2 emissions and open possibilities to net-zero carbon based energy production.[11] One approach for CO_2 utilization can be direct conversion of CO_2 to light olefins (ethylene, propylene, and butylene) by a tandem catalyst via methanol mediated reaction, where CO_2 is first hydrogenated to methanol (3.1), followed by methanol-to-olefins (MTO) reaction (3.2) in a single reactor.[180,181]

$$CO_2 + 3H_2 \rightleftharpoons CH_3OH + H_2O,\ \Delta H^o = -49.5\ \text{kJ mol}^{-1} \qquad (3.1)$$

$$nCH_3OH \leftrightarrows C_nH_{2n} + nH_2O \qquad (3.2)$$

$$CO_2 + H_2 \leftrightarrows CO + H_2O,\ \Delta H^\circ = +42.1\ \text{kJ mol}^{-1} \qquad (3.3)$$

The former reaction is thermodynamically favored at low reaction temperatures (< 250 °C), while the MTO reaction can be operated at high reaction temperatures (> 350 °C).[182,183] The difference in reaction temperatures can decrease the desired product selectivity, when two active catalysts for each reaction are coupled in a single reactor as a tandem reaction. However, the tandem process can promote consumption of the intermediate species, shifting the reaction equilibrium to the right, while minimizing the undesired CO formation by reverse water-gas shift (RWGS) reaction (3.3).[184] Additionally, the methanol intermediate route occurring on the tandem catalyst can break the Anderson–Schulz–Flory (ASF) distribution, which results in higher light olefins selectivity (> 80%) compared with the modified Fischer–Tropsch reaction.[185,186]

Generally, the direct conversion of CO_2-to-light olefins can be carried out on a mixture of In_2O_3 supported on ZrO_2 and SAPO-34, where CO_2 to methanol and MTO reactions occur, respectively.[180,187] Surface oxygen vacancies of In_2O_3 has been identified as active sites for methanol formation by CO_2 hydrogenation.[188,189] The oxygen vacancies created by H_2 can promote CO_2 activation and stabilize the reaction intermediates, followed by replenishing the oxygen vacancy by CO_2, producing methoxy species during the reaction.[190] One of the most well-performing catalysts investigated for the CO_2 hydrogenation to methanol is ZrO_2-supported In_2O_3. In_2O_3 supported on monoclinic zirconia demonstrates up to 10 times higher methanol yield than In_2O_3 supported on Al_2O_3, CeO_2, TiO_2, ZnO, and SiO_2 due to the tensile strain caused by pronounced lattice mismatching.[189,191] In_2O_3/ZrO_2 can provide not only higher dispersion and sintering resistance but also advantageous metal–support interaction, which all promote high stability of the catalyst.[189,191,192] High dispersion of In_2O_3 on ZrO_2 leads to a strong electronic interaction with ZrO_2, The electrons located in the vicinity of ZrO_2 can be depleted by In_2O_3 impregnation, abstracting O atoms from the active phase leading to increase the vacancies.[189] Dang et al. demonstrated that chemisorption of CO_2 is stronger on the oxygen vacancy sites close to Zr ions compared to that on the pure In_2O_3. These sites can also stabilize intermediate species for methanol formation in $In_{1-x}Zr_xO_y$ and promote activity.[193]

Unlike ZrO_2, yttria-stabilized zirconia (YSZ) is a unique material with a stable cubic fluorite structure that is prone to higher levels of oxygen-ion conductivity due to the difference in valence charges of Y^{3+} to Zr^{4+}. YSZ-based catalysts have been generally studied for oxidation reaction as it can facilitate spillover of oxygen ions onto the metal surface. For instance facile oxygen ion diffusion in YSZ can replenish the oxygen consumed by partial oxidation of methane enhancing the activity.[194] In addition to the oxygen diffusion, YSZ promotes metal–support interaction with high oxygen vacancies, and it is shown to have high reaction rate for low temperature toluene oxidation despite the low Pt dispersion.[195] The spillover of oxygen ion species onto metals due to the strong metal–support interaction can enhance the activity because oxygen chemisorption on Pt is the rate-determining step for toluene oxidation. The YSZ-supported catalysts can have beneficial effect for CO_2 hydrogenation as strong interaction between metal and YSZ with high content of oxygen vacancies can facilitate CO_2 adsorption with stabilizing the reaction.[191,196]

For the MTO reaction, chabazite zeolites with high hydrothermal stability, such as SAPO-34, are great interest due to their excellent performance and high selectivity towards light olefins production.[197] L. Han et al. synthesized hierarchical porous SAPO-34, and it presented a long lifetime of up to 740 min with light olefins selectivity of 87.5%.[198] However, the channels in SAPO-34 can be partially blocked by coking, deactivating the reaction.[199] It is reported that low crystal size of SAPO-34 can increase the catalyst lifetime and product selectivity because the high external surface area and short residence time of the reactants and products hinders the coking and further formation of paraffins or larger hydrocarbons.[200,201] Therefore, applying the nano-sized SAPO-34 can benefit the stability of the tandem catalyst for CO_2 hydrogenation to light olefins.

Here, we report a tandem catalyst composed of indium oxide supported on zirconia and nano-sized SAPO-34 zeolite for direct CO_2 hydrogenation to light olefins at high temperature (420 °C). Two different types of zirconia-based supports (YSZ and ZrO_2) are adopted and compared in the reaction performance. The high oxygen vacancies in YSZ can stabilize the light olefins production, and developed nano-sized SAPO-34 can prolong the lifetime of the catalytic reaction with high light olefins selectivity without any significant coke formation.

3.2 Experimental Methods

3.2.1 Catalyst preparation

In_2O_3 supported on YSZ (Sigma Aldrich) and ZrO_2 (Alfa Aesar) catalysts were prepared with 10 wt% of In using incipient wetness impregnation. Appropriate amounts of indium nitrate hydrate ($In(NO_3)_3 \cdot xH_2O$, 99.99%, Alfa Aesar) was dissolved in deionized (DI) water, and the aqueous solution were added dropwise to the support. The sample was dried at 373 K overnight and calcined in static air at 773 K for 4 h with a ramping rate of 5 °C min^{-1}. The prepared catalysts in YSZ and ZrO_2 supports are denoted as In_2O_3/YSZ and In_2O_3/ZrO_2, respectively. A nano-sized SAPO-34 was synthesized by a microwave-assisted hydrothermal method. Finely ground aluminum isopropoxide ($Al(OPr^i)_3$, 98%, Sigma Aldrich) was mixed with tetraethylammonium hydroxide solution (TEAOH, ~40% in H_2O, Sigma Aldrich) and DI water until dissolved completely. Tetraethyl orthosilicate (TEOS, 99.0%, Sigma Aldrich) was then added dropwise to the solution, followed by stirring for 2 h. After that, phosphoric acid (H_3PO_4, 85%, Alfa Aesar) was added dropwise, and the mixture was further stirred for additional 1 h. The final precursors gel with the molar composition of $1.0Al_2O_3 : 1.2P_2O_5 : 0.6SiO_2 : 2.0TEAOH : 40H_2O$ was transferred into Teflon vessels and placed inside a microwave oven (MARS 5, CEM Corporation). The vessels were heated to 180 °C with magnetic stirring for 1 h under autogenous pressure with an 800 W output. The resulting solids were collected by centrifugation and washed with ethanol (C_2H_6O, anhydrous, Fisher Chemical) and DI water. The washed sample was dried at 100 °C overnight and calcined in static air at 500 °C for 6 h with a ramping rate of 5 °C min^{-1}.

The activity of microwave synthesized SAPO-34 is compared with the commercial SAPO-34^{COM}, purchased from ACS Material, LLC.

3.2.2 Characterization

High-resolution transmission electron microscopy (HRTEM) images with energy dispersive X-ray spectroscopy (EDX) were obtained using JEOL Grand ARM. The samples were ultrasonically dispersed in ethanol and loaded on a carbon coated Cu grid. Field emission scanning electron microscopy (FESEM) images were taken on Zeiss Ultra plus. Powder X-ray diffraction (XRD) patterns were recorded with Rigaku MiniFlex II using Cu Kα source radiation ($\lambda = 1.5406$ Å) in a 2θ range of 10°–80° with a step rate of 2° min^{-1}. Raman spectroscopy measurements were conducted on XploRA PLUS, Horiba in the backscattering configuration using 638 nm wavelength. N_2 adsorption and desorption isotherms were collected by Micromeritics ASAP 2020 at −196 °C. Prior to the measurements, the samples were degassed at 300 °C for 7 h. Surface area, pore volume, and pore size were determined by Brunauer-Emmett-Teller (BET) and Barrett-Joyner- Halenda (BJH) methods. H_2 temperature-programmed reduction (H_2-TPR) was conducted on Micromeritics AutoChem II. First, 50 mg of catalyst was heated at 300 °C for 1 h under helium, and then cooled down to 30 °C. After pretreatment step, the temperature was ramped from 30 °C to 900 °C at a rate of 10 °C min^{-1} in a 10% H_2/Ar mixture with recording the signal in thermal conductivity detector (TCD). H_2 chemisorption experiments were conducted on the same Micromeritics AutoChem II to obtain H_2 uptake. 100 mg of catalyst was purged at 300 °C for 1 h under He, and H_2 pulse chemisorption was carried out at 35 °C in 10% H_2/Ar with 8 min intervals. H_2 temperature-programmed desorption (H_2-TPD) and CO_2-TPD were performed on Micromeritics 3Flex equipped with TCD. First, 100 mg of catalyst was heated at 300 °C for 1 h under argon and cooled down to 50 °C. After the preparation step, the sample was saturated in H_2 or CO_2 for 1 h at 50 °C, followed by purging with argon for additional 1 h to remove any physisorbed molecules. H_2-TPD and CO_2-TPD experiments were then performed at 50–1000 °C with a heating rate of 10 °C min^{-1} in argon flow. X-ray photoelectron spectroscopy (XPS) was performed using a Kratos Axis Ultra DLD with Al K_α radiation, and the binding energy was calibrated to the signal of C 1s at 284.8 eV. Thermogravimetric analysis (TGA) was employed on TG 209 F1 Libra, NETZSCH. The samples were heated from 30 °C to 900 °C with a ramping temperature of 10 °C min^{-1} under flowing air.

3.2.3 Catalyst evaluation

The performance of tandem catalysts for CO_2 hydrogenation to light olefins was carried out in a fixed-bed continuous-flow reactor. The supported In_2O_3 and SAPO-34 was mixed physically with a mass ratio of 1:1. 400 mg of the tandem catalyst was loaded in a stainless-steel tubular reactor with an inlet diameter of 7.7 mm. Temperature of the catalyst was measured using a K-type thermocouple placed on top of the catalyst bed. The reaction gases ($CO_2 : H_2 : N_2 = 1 : 3 : 1$) were introduced to the reactor via mass flow controllers. The reaction was conducted at 320–420 °C under 30 bar at a GHSV of 4,000 ml g^{-1} h^{-1}. The effluent gases were analyzed online using a gas chromatograph (GC) equipped with a TCD and a flame ionization detector (FID). The CO_2 conversion (X), product selectivity (S), and light olefins yield (Y) are calculated using the following equations:

$$\mathrm{X}\,(\%) = \frac{\mathrm{F_{CO2,in}} - \mathrm{F_{CO2,out}}}{\mathrm{F_{CO2,in}}} \times 100 \qquad (3.4)$$

$$\mathrm{S_{CO}}\,(\%) = \frac{\mathrm{F_{CO}}}{\mathrm{F_{CO}} + \sum_1^m \mathrm{F_{CmHn}}} \times 100 \qquad (3.5)$$

$$\mathrm{S_{CmHn}}\,(\%) = \frac{\sum_1^m \mathrm{mF_{CmHn}}}{\mathrm{F_{CO}} + \sum_1^m \mathrm{mF_{CmHn}}} \times 100 \qquad (3.6)$$

$$Y_{C_2^{=}-C_4^{=}}\ (\mathrm{mmol\ h^{-1}\ g_{cat}^{-1}}) \ = \ \frac{\mathrm{GHSV}\cdot\frac{X_{CO2}}{100}\cdot\frac{S_{C2-C4}}{100}}{22.4} \qquad (3.7)$$

where $F_{CO2,in}$ and $F_{CO2,out}$ are the molar flow rates of CO_2 measured at the inlet and outlet of the reactor, respectively, and F_{CO} and F_{CmHn} are the molar flow rates of the products. In all experiments, carbon molar balance was closed within ±2%, and the reproducibility of the catalytic activity for all experiments is found to be deviating within ±5%.

3.3 Results and Discussion

3.3.1 Characterization of catalysts

Figure 3.1a,b show TEM images of In_2O_3/YSZ and In_2O_3/ZrO_2 with particle size distribution in the inset of the images. The particles of the In_2O_3/YSZ is distributed in the range of 2–10 nm with the average size of 6.0 nm, whereas In_2O_3/ZrO_2 has particle size from 10 nm to 45 nm with the average size of 21.1 nm. The HRTEM images in Figure 3.1c,d show a lattice fringe with interplanar spacings of 0.29 nm corresponding to the In_2O_3 (222) planes, and the In_2O_3 is shown to be deposited on the surface of both YSZ and ZrO_2. The In_2O_3 particle supported on YSZ shows size of 7.1 nm, which is similar with the YSZ support, and In_2O_3 deposited on ZrO_2 has size of 9.4 nm. The EDX elemental mapping analysis indicates that the In_2O_3 particles are dispersed evenly on the YSZ and ZrO_2 supports (Figure 3.1e,f).

The XRD patterns of In_2O_3/YSZ, In_2O_3/ZrO_2, and bare supports are shown in Figure 3.2a. The diffraction patterns observed at 2θ of 24.2°, 28.2°, 31.6°, and 34.3° for In_2O_3/ZrO_2 and ZrO_2 correspond to the monoclinic zirconia phase (Crystallography Open Database (COD) no. 96-900-5834). The XRD pattern for the In_2O_3/ZrO_2 catalyst shows an additional diffraction peak at 2θ of 31.0°, which is assigned to the (222) plane of the In_2O_3 bcc phase (COD no. 96-152-

1754). The XRD patterns for both In_2O_3/YSZ and YSZ show diffraction peaks at 30.5°, 35.3°, 50.5°, and 59.9°, which are assigned to the cubic zirconia phase (COD no. 96-152-1754).[202] In_2O_3 diffraction peaks are not detectable for In_2O_3/YSZ because of the overlapped large cubic zirconia peak located at 30.5°. The lattice constants of cubic In_2O_3 and cubic zirconia are similar to each other, which makes the XRD patterns to be identical.[191] The crystallite size of In_2O_3 calculated using the Scherrer equation is 11.3 nm for In_2O_3/ZrO_2 (Table 3.1). The crystallite sizes of YSZ and ZrO_2 is 6.9 nm and 15.4 nm, respectively, which is in good agreement with the

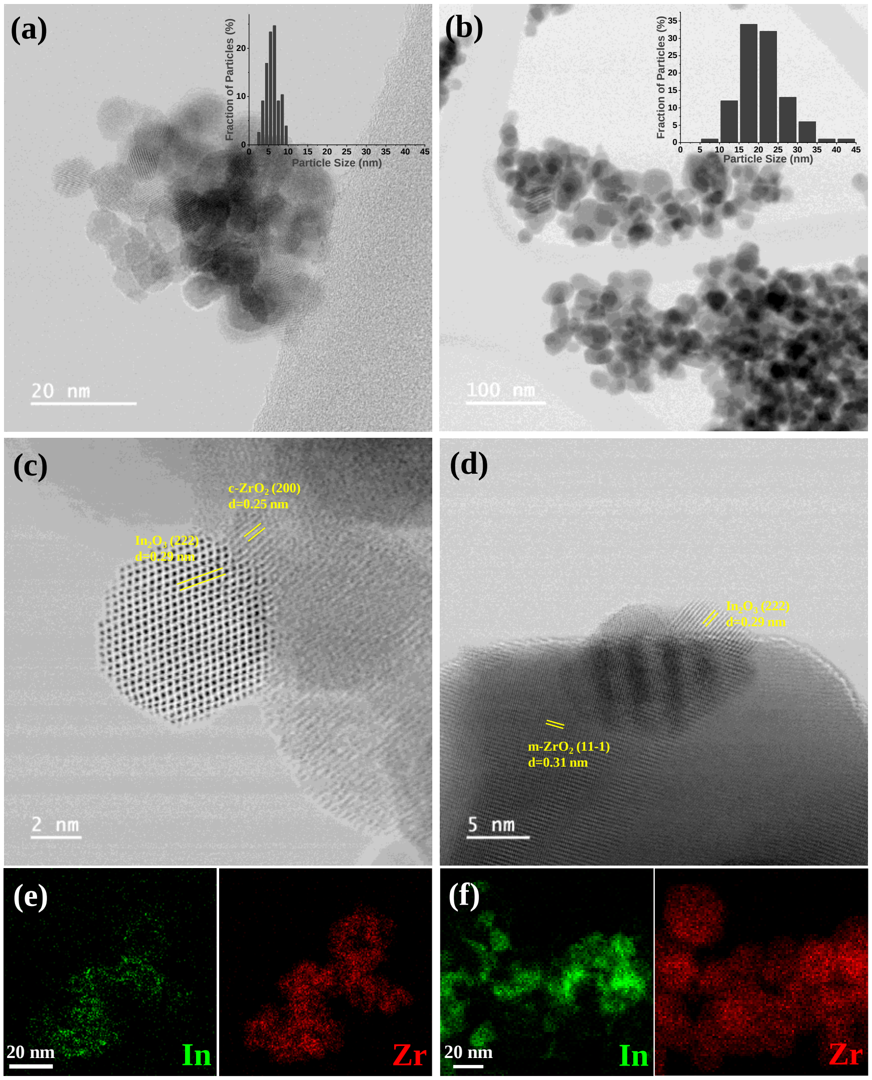

Figure 3.1. HRTEM and EDX elemental mapping images of (a) In_2O_3/YSZ and (b) In_2O_3/ZrO_2 (In: green and Zr: red)

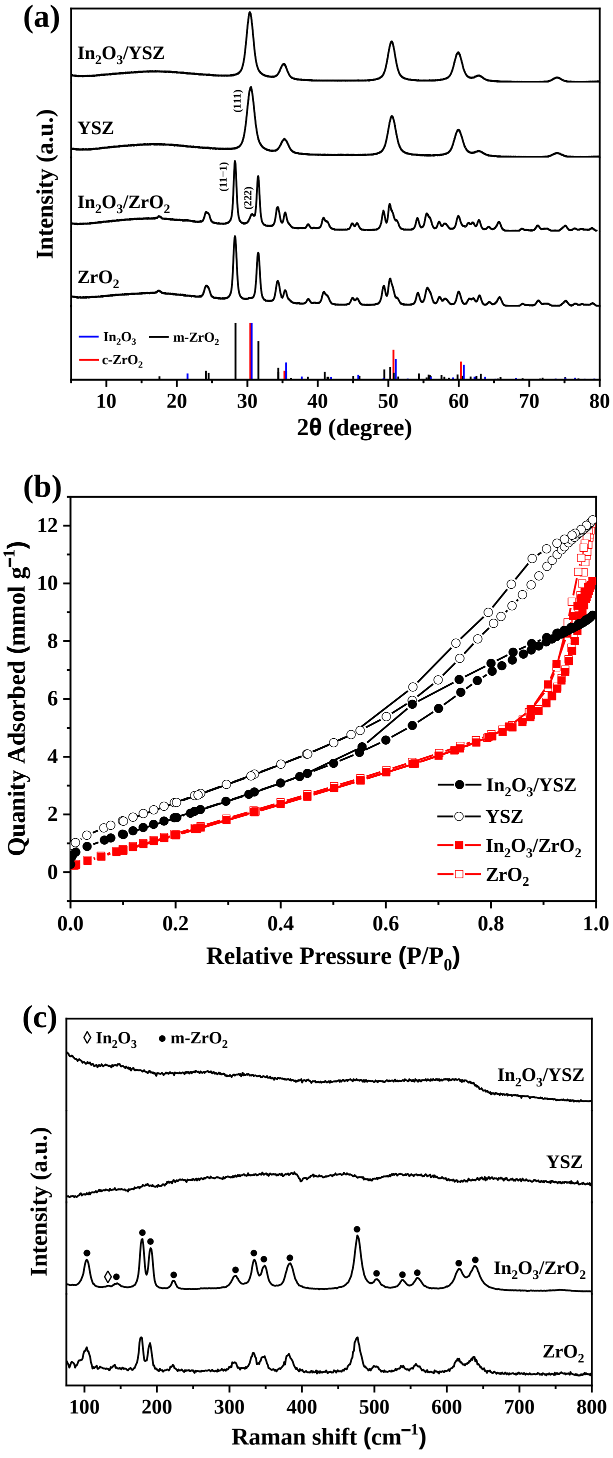

Figure 3.2. (a) XRD patterns, (b) N_2 adsorption–desorption isotherms, and (c) Raman spectra of In_2O_3/YSZ, In_2O_3/ZrO_2, and their bare supports.

TEM analysis. After impregnation of indium species, the crystallite sizes of YSZ and ZrO_2

slightly increase to 7.4 nm and 18.0 nm, respectively, possibly due to the sintering of ZrO_2 species during calcination.

Table 3.1. Crystallite size of In_2O_3/YSZ, In_2O_3/ZrO_2, and their bare supports.

Catalysts	Crystallite size (nm)		
	m-ZrO_2 (11−1)	c-ZrO_2 (111)	In_2O_3 (222)
In_2O_3/YSZ	-	7.4	-
YSZ	-	6.9	-
In_2O_3/ZrO_2	18.0	-	11.3
ZrO_2	15.4	-	-

N_2 adsorption–desorption isotherms of catalysts are shown in Figure 3.2b, and their textural properties are displayed in Table 3.2. All isotherms can be assigned to type IV isotherms with H2 hysteresis, indicating that mesoporous with bottle necked structures formed after impregnation and calcination process.[187] The specific surface areas of the bare YSZ and ZrO_2 supports are 222.4 $m^2\ g^{-1}$ and 158.7 $m^2\ g^{-1}$ with the pore volume of 0.399 $cm^3\ g^{-1}$ and 0.270 $cm^3\ g^{-1}$, respectively. YSZ possesses larger surface area and pore volume than ZrO_2 because of smaller particle size of YSZ than ZrO_2. After impregnation of In_2O_3, the surface area and pore volume of the both supports decrease as In_2O_3 can occupy pores of the support. The difference is more pronounced for the YSZ than ZrO_2 due to the similar size between YSZ and In_2O_3. As shown in Figure 3.3 and Table 3.2, the pore sizes of In_2O_3/YSZ and In_2O_3/ZrO_2 show similar values of 6.33 nm and 6.74 nm, respectively. The presence of mesopores in In_2O_3/ZrO_2 could be associated with the interparticle voids within the particles possibly due to the large particle size of ZrO_2, whereas In_2O_3/YSZ does not show the mesopores region due to the small particle size, evidenced by TEM and XRD analysis.

Table 3.2. Textural properties of In_2O_3/YSZ, In_2O_3/ZrO_2, and their bare supports.

Catalysts	S_{BET} ($m^2\ g^{-1}$)^a	V_p ($cm^3\ g^{-1}$)^a	Pore size (nm)
In_2O_3/YSZ	184.8	0.292	6.33
YSZ	222.4	0.399	7.18
In_2O_3/ZrO_2	157.6	0.266	6.74
ZrO_2	158.7	0.270	6.79

$^a S_{BET}$ and V_p represent the BET surface area and total pore volume, respectively.

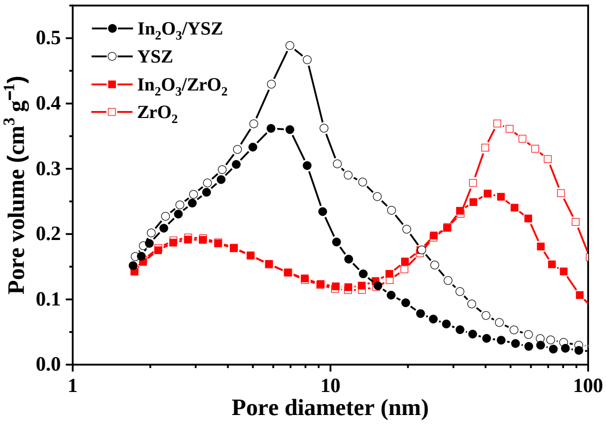

Figure 3.3. Pore size distribution diagrams of In_2O_3/YSZ, In_2O_3/ZrO_2, and their bare supports using the Barrett–Joyner–Halenda (BJH) method.

The Raman spectra of the catalysts are collected to determine the structural disorders and oxygen vacancies. As shown in Figure 3.2c, the spectra of In_2O_3/YSZ and YSZ can be characterized by amorphous-like broad bands, related to the disordered oxygen sublattice and lowering symmetry from the Y substitution of Zr.[203,204] Both In_2O_3/ZrO_2 and ZrO_2 shows the typical vibrational peaks centered at 103 cm^{-1}, 144 cm^{-1}, 180 cm^{-1}, 191 cm^{-1}, and 223 cm^{-1} corresponding to the monoclinic zirconia phase. The small peak located at 133 cm^{-1} for In_2O_3/ZrO_2 can be assigned to the phonon vibration modes of the bcc-In_2O_3. The structural disordering in Raman for YSZ can be associated with the oxygen vacancies.[204] The high amount of oxygen vacancy in YSZ can provide facile oxygen vacancy elimination and generation cycle, which can enhance the catalytic performance.

H_2-TPR is performed to investigate the reducibility of In species and their interaction with the support in Figure 3.4. As a baseline, the bare YSZ and ZrO_2 supports are also analyzed for their H_2 consumption. Both bare supports do not show any distinct H_2 reduction peaks up to 900 °C due to the irreducible nature of YSZ and ZrO_2. After In_2O_3 impregnation, a small broad α peak at the temperature range of 150–400 °C is observed on both In_2O_3/YSZ and In_2O_3/ZrO_2, which can be ascribed to the partial reduction of dispersed In species on the surface.[193] The dispersed species can have more oxygen vacancies with low formation energy of oxygen vacancy.[205206] This indicates that the oxygen vacancies might be presented at the CO_2 hydrogenation reaction temperature applied. The high temperature peak (β) located at 464 °C for In_2O_3/ZrO_2 can be assigned to the reduction of In_2O_3 into metallic In.[207] The asymmetric shape with a tail of the reduction peak suggests the presence of heterogeneously distributed In species. The unsupported In_2O_3 also contains two broad peaks from the reduction of In_2O_3, as shown in Figure 3.5. The small broad peak (α) at low temperature below 127 °C is related with the

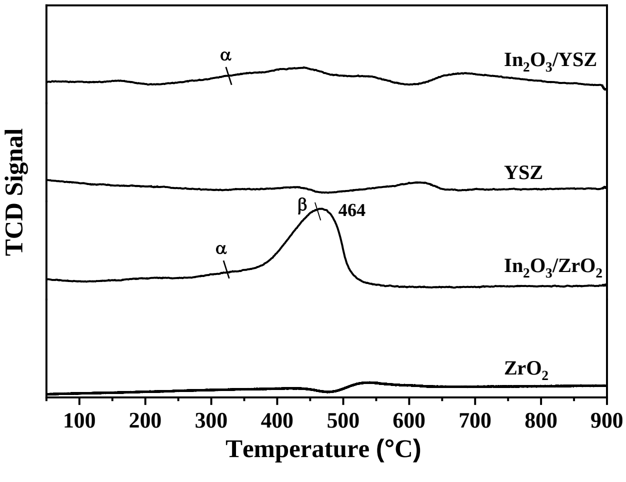

Figure 3.4. H_2-TPR profiles of In_2O_3/YSZ, In_2O_3/ZrO_2, and their bare supports.

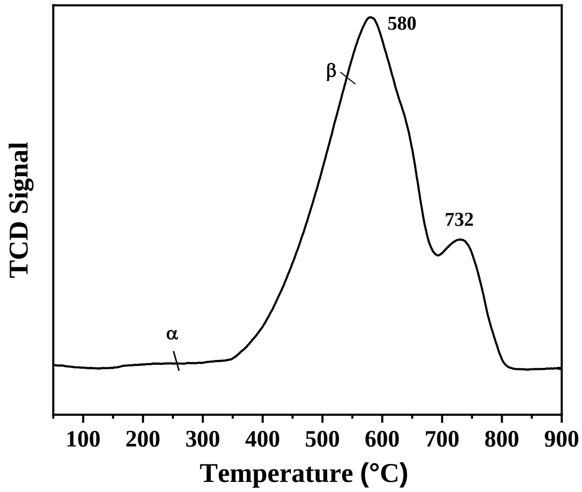

Figure 3.5. H_2-TPR profile of pure In_2O_3.

reduction of surface In_2O_3, and the strong peak (β) at high temperature range (> 400 °C) is attributed to the reduction of bulk In_2O_3.[208] The peak located at much higher temperature (732 °C) could be related to the reduction of the large crystallite size of In_2O_3.[209] When In_2O_3 is impregnated onto the ZrO_2 support, the major peaks shift to the lower temperature from 580 °C to 464 °C, suggesting that supported In_2O_3 is more easily reduced than unsupported In_2O_3. However, when In_2O_3 is impregnated onto YSZ, no distinct peaks are observed. In_2O_3 on YSZ can be hardly reduced compared to In_2O_3 on ZrO_2 due to the strong metal–support interaction, which can provide high metal dispersion, thereby high activity. H_2 chemisorption measured on the samples shows that H_2 uptake for In_2O_3/YSZ is 2.26 times larger than that for In_2O_3/ZrO_2 (Table 3.3).[210] In addition, the strong metal–support interaction can prevent In_2O_3 from over-reduction to metallic In, stabilizing the methanol production as oxygen vacancies in In_2O_3 is the

Table 3.3. H_2 uptake measured by H_2 chemisorption for In_2O_3/YSZ and In_2O_3/ZrO_2.

Catalysts	H_2 uptake (mmol g^{-1})
In_2O_3/ZrO_2	0.0093
In_2O_3/YSZ	0.0210

the active sites.[188]

Figure 3.6a shows the H_2-TPD profiles of the supported In_2O_3 and bare supports. The bare ZrO_2 support presents less amount of H_2 adsorption capacity and lower desorption temperature of 240 °C compared to the bare YSZ support. YSZ shows not only large amount of H_2 adsorption capacity but also a higher H_2 adsorption temperature of 440 °C. Impregnation of In_2O_3 onto the both supports lowers the desorption temperature and H_2 adsorption capacity compared to the bare supports. However, In_2O_3/YSZ still shows larger H_2 adsorption capacity and higher H_2 desorption temperature of 263 °C than that of 231 °C for In_2O_3/ZrO_2. CO_2-TPD is

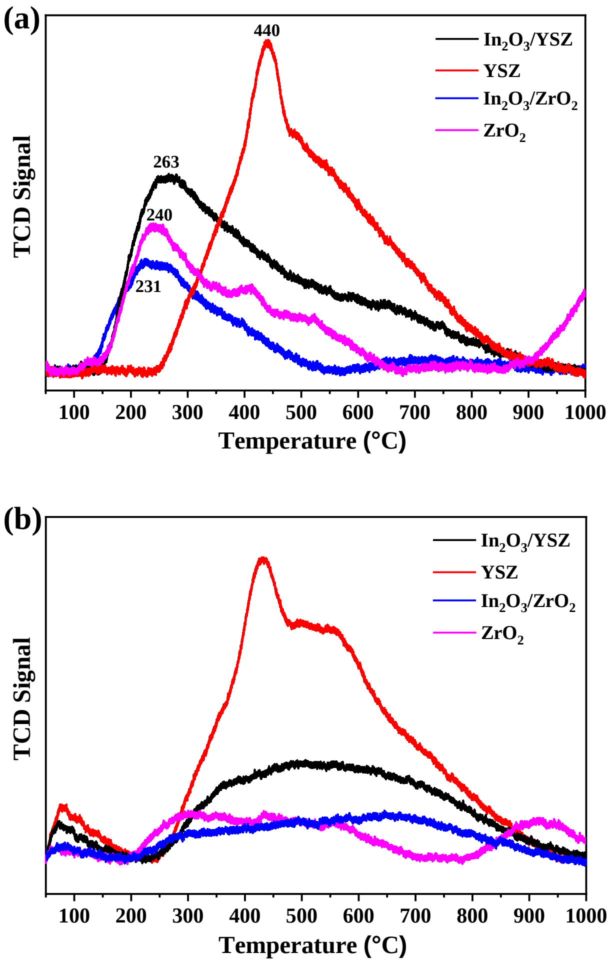

Figure 3.6. (a) H_2-TPD and (b) CO_2-TPD profiles of In_2O_3/YSZ, In_2O_3/ZrO_2, and their bare supports.

performed to elucidate oxygen vacancies of the catalysts. As shown in Figure 3.6b, the desorption peak observed at low temperatures (50–200 °C) can be ascribed to the desorption of the physiosorbed CO_2 from weak basic sites. The large peaks observed at temperatures higher than 200 °C can be associated to the chemisorbed CO_2 on the oxygen vacancies.[211] The bare YSZ presents the highest CO_2 uptake, whereas the bare ZrO_2 shows the lowest CO_2 adsorption capacity. This finding indicates that YSZ provides stronger CO_2 adsorption sites on the oxygen vacancy site near the Zr than the ZrO_2. After In_2O_3 impregnation, In species on the supports lowers the CO_2 uptake compared to the bare supports. However, In_2O_3/YSZ still shows a larger CO_2 uptake compared to In_2O_3/ZrO_2. Gao et al. reported that CO_2 is strongly chemisorbed on the oxygen vacancy sites near the Zr dopant on $In_{1-x}Zr_xO_y$ surface than the pure In_2O_3.[180] The enhanced adsorption capacity for both H_2 and CO_2 can increase CO_2 hydrogenation activation on the YSZ-supported In_2O_3.

Core level photoelectron spectra of the supported In_2O_3 and bare supports are collected to elucidate surface speciation. As shown in Fig. 3.7a, the O 1s core level spectra of catalysts can be deconvoluted into three peaks, whose relative contents are shown in Table 3.4. The main peak located at 530.0 eV originates from the lattice oxygen (O_{latt}), and two other peaks observed at

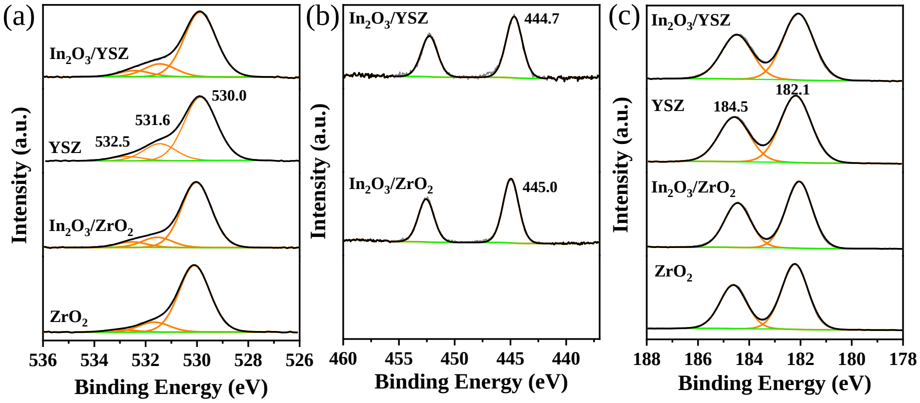

Figure 3.7. (a) O 1s, (b) In 3d, and (c) Zr 3d XPS spectra of In_2O_3/YSZ, In_2O_3/ZrO_2, and their bare supports.

Table 3.4. Relative surface concentration of oxygen species of In_2O_3/YSZ, In_2O_3/ZrO_2, and their bare supports measured by XPS

Catalysts	O_{latt}	O_{ads}	OH	O_{ads}/O_{latt}
In_2O_3/YSZ	77.3	15.4	7.3	0.20
YSZ	74.8	20.2	5.0	0.27
In_2O_3/ZrO_2	80.5	12.6	6.9	0.16
ZrO_2	84.3	12.7	3.0	0.15

531.6 eV and 532.5 eV can be assigned to surface adsorbed oxygen (O_{ads}) and surface hydroxyls (OH) groups, respectively. The oxygen defect concentration, which is proportional to the O_{ads}/O_{latt} ratio, are measured to be 0.20 and 0.16 for In_2O_3/YSZ and In_2O_3/ZrO_2, respectively, indicating that the YSZ supported-In_2O_3 presents higher surface oxygen vacancies compared to In_2O_3/ZrO_2. For the bare supports, YSZ possesses almost two times higher oxygen vacancies (0.27) than ZrO_2 (0.15). The In 3d core level spectra show two main peaks corresponding to the characteristic spin-orbit coupling of In^{3+} (Figure 3.7b). It is noted that the In $3d_{5/2}$ peak of In_2O_3/YSZ has a lower binding energy of 444.7 eV compared to the one of 445.0 eV for In_2O_3/ZrO_2, indicating that electron density of In on YSZ increases through the donated electrons from the neighboring Zr sites due to the strong metal–support interaction, matching well with the H_2-TPR results.[193] The Zr 3d core level spectra indicates that the spin-orbit doublet of Zr^{4+} has similar binding energies for Zr $3d_{3/2}$ (184.5 eV) and Zr $3d_{5/2}$ (182.1 eV) for both In_2O_3/YSZ and In_2O_3/ZrO_2, as shown in Figure 3.7c. The atomic In/Zr ratios on the In_2O_3/YSZ and In_2O_3/ZrO_2 surfaces are calculated to be 12.7% and 20.4%, respectively (Table 3.5). The low In/Zr ratio on In_2O_3/YSZ indicates less In enrichment on the support surface, suggesting a high In_2O_3 dispersion, in consistent with the H_2-TPR and H_2 chemisorption data.

Table 3.5. Relative surface chemical concentration of In_2O_3/YSZ, In_2O_3/ZrO_2, and their spent catalysts without SAPO-34 after 45 h of reaction.

Catalysts		Surface concentration (at%)[a]					ratios	
		Zr	In	O	Y	C	In/Zr	Zr/O
Fresh	In_2O_3/YSZ	22.8	2.9	65.4	3.3	5.6	12.7	34.9
	In_2O_3/ZrO_2	24.0	4.9	59.3	-	11.8	20.4	40.5
Spent (320 °C)	In_2O_3/YSZ	36.9	3.7	49.1	3.2	7.1	10.0	75.2
	In_2O_3/ZrO_2	37.1	3.4	40.7	-	18.8	9.2%	91.2
Spent (693 °C)	In_2O_3/YSZ	40.3	3.9	48.1	3.1	4.6	9.7%	83.8
	In_2O_3/ZrO_2	45.5	5.1	42.4	-	7.0	11.2	107.3

[a] Measured by XPS analysis

Figure 3.8a,c,d show the SEM and STEM images of the nano-sized SAPO-34 synthesized by microwave heating. The developed SAPO-34 presents small spherical particle

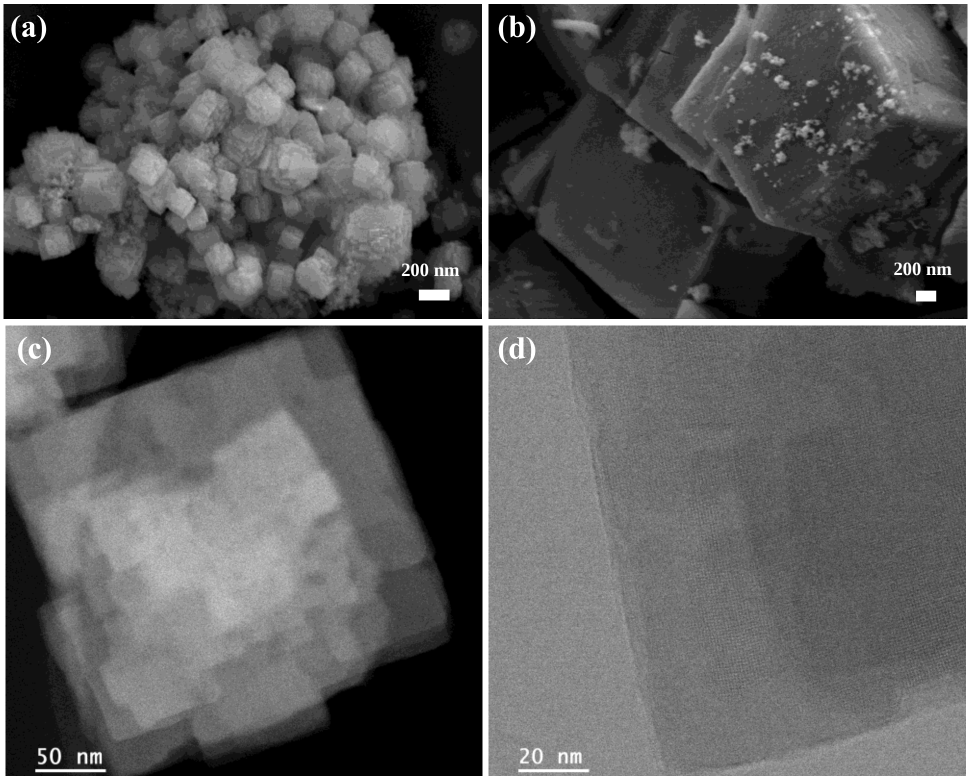

Figure 3.8. SEM images of (a) nano-sized SAPO-34 and (b) commercial SAPO-34^{COM} and (c) HAADF-STEM and (d) STEM images of nano-sized SAPO-34.

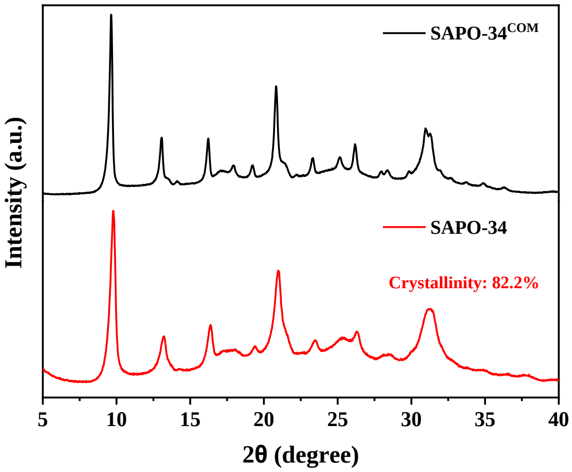

Figure 3.9. XRD patterns of nano-sized SAPO-34 and commercial SAPO-34.

sizes ranging in between 0.2–0.35 µm, possibly formed by aggregation of the cubic crystals of ca. 60 nm. However, commercially obtained SAPO-34^{COM} has much larger particle sizes ranging from 2–5 µm (Figure 3.8.b). The XRD pattern of the synthesized SAPO-34 shows characteristic diffraction peaks of the CHA structure and match with the XRD pattern of SAPO-34^{COM} (Figure 3.9). The diffraction peaks of the nano-sized SAPO-34 have broader shapes and their intensities are lower than those of SAPO-34^{COM}, leading to an ~80% of relative crystallinity. N_2 adsorption-

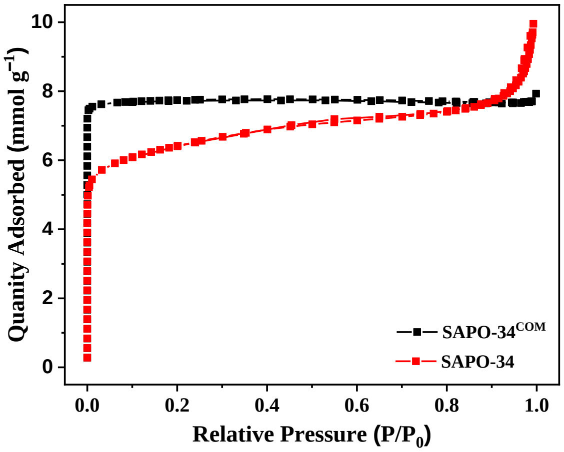

Figure 3.10. N_2 adsorption–desorption isotherms of nano-sized SAPO-34 and commercial SAPO-34^{COM}.

desorption isotherms of the nano-sized SAPO-34 and SAPO-34^{COM} are analyzed (Figure 3.10), and their textural properties are shown in Table 3.6. SAPO-34^{COM} has Type I isotherm, whereas developed SAPO-34 has a composite of Types I and II isotherms with pronounced N_2 uptake near saturation pressure. This indicates that the synthesized SAPO-34 has nano-sized hierarchical structures consisting of smaller crystal sizes as well as mesopores and macropores.[201,212] The overall surface area of SAPO-34^{COM} (527.0 m^2 g^{-1}) is larger than that of the nano-sized SAPO-34 (455.9 m^2 g^{-1}). However, the nano-sized SAPO-34 possesses much larger external surface area of 162.0 m^2 g^{-1} due to the small crystal size, whereas SAPO-34^{COM} presents small external surface area of 20.7 m^2 g^{-1}. It is known that high external surface area can provide enhanced mass transfer for reactants and products.[212] This would be beneficial for the MTO reaction. For instance, the less contact time of the produced light olefins with SAPO-34 can reduce further conversion of light olefins to paraffins or aromatics. Additionally, the decreased crystal size can shorten the diffusion length for the reactants and products leading to a less coke deposition.[213]

Table 3.6. Textural properties of nano-sized SAPO-34 and commercial SAPO-34^{COM}.

	SAPO-34	SAPO-34^{com}
$S_{overall}$ (m^2 g^{-1})	455.9	527.0
S_{micro} (m^2 g^{-1})	293.9	506.3
$S_{external}$ (m^2 g^{-1})	162.0	20.7
Pore size (nm)	2.485	2.023
V_{micro} (cm^3 g^{-1})	0.152	0.259
V_{meso} (cm^3 g^{-1})	0.131	0.007
Crystal size (μm)	0.2–0.35	2–5

3.3.2 Activity measurements

CO_2 hydrogenation activity of In_2O_3/YSZ with/without the presence of the microwave synthesized SAPO-34 is measured at each reaction temperatures after 4 h of reaction. As shown in Figure 3.11(a) and Table 3.7, when only In_2O_3/YSZ presents, methanol is produced at 320 °C with CO_2 conversion of 10.4% and methanol, CO and CH_4 selectivity's of 43.2%, 54.8% and 2.0%, respectively. CO is the major product with high selectivity due to the kinetically favored endothermic RWGS reaction, and undesired CH_4 can be generated by CO_2 methanation reaction (the Sabatier reaction, $CO_2 + 4H_2 \rightarrow CH_4 + 2H_2O$, $\Delta H^o = -165.0$ kJ mol^{-1}). When the reaction temperature increases to 370 °C and 420 °C, the CO_2 conversion increases to 25.9% and 34.9%, respectively, and CO selectivity increases to 77.1% and 97%, respectively. Hydrocarbons are not observed at all reaction temperatures, as molecular sieves are required for methanol conversion

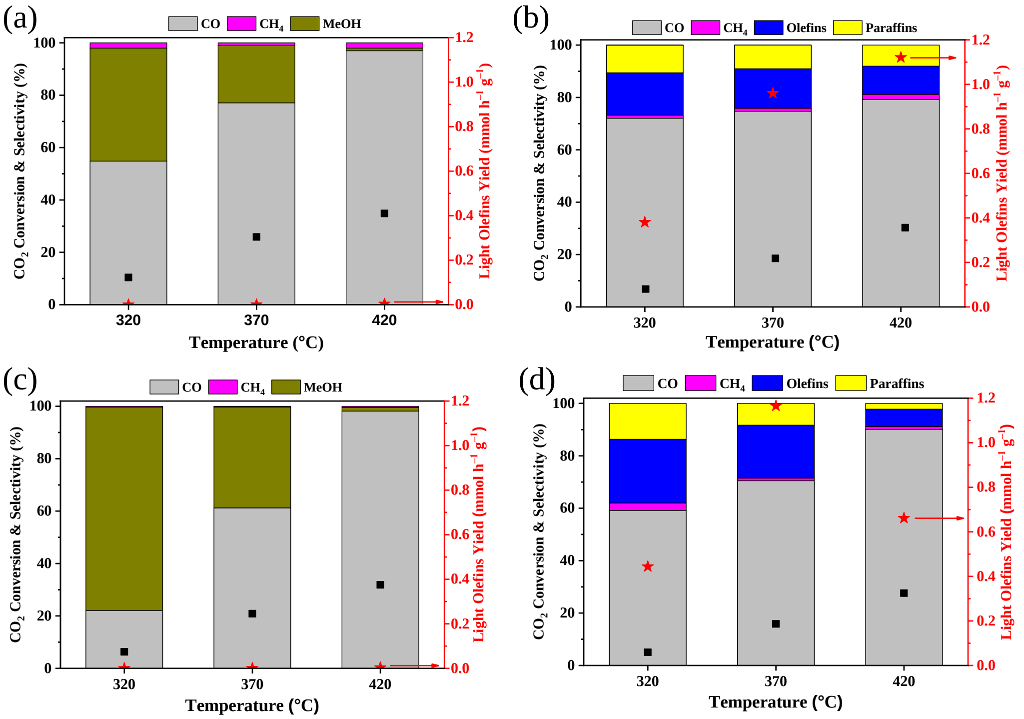

Figure 3.11. CO_2 conversion (black square), product selectivity (bar graph), and light olefins yield (red star) of (a) In_2O_3/YSZ, (b) In_2O_3/YSZ//SAPO-34, (c) In_2O_3/ZrO_2, and (d) In_2O_3/ZrO_2//SAPO-34.

Table 3.7. Catalytic performance in CO_2 hydrogenation of supported In_2O_3 with/without SAPO-34 at different temperatures.

	Catalysts	X_{CO2} (%)	Product selectivity (%)					Light olefins yield (mmol h^{-1} g^{-1})
			CO	CH_4	MeOH	Light olefins	Light paraffins	
320 °C	In_2O_3/YSZ	10.4	54.8	2.0	43.2	-	-	-
	In_2O_3/YSZ//SAPO-34	6.8	72.1	1.1	-	16.3	10.5	0.380
	In_2O_3/ZrO_2	6.3	22.1	0.3	77.6	-	-	-
	In_2O_3/ZrO_2//SAPO-34	5.9	59.2	2.8	-	24.3	13.7	0.444
370 °C	In_2O_3/YSZ	25.9	77.1	1.1	21.8	-	-	-
	In_2O_3/YSZ//SAPO-34	18.5	74.7	1.1	-	15.2	9.0	0.960
	In_2O_3/ZrO_2	20.9	61.2	0.3	38.5	-	-	-
	In_2O_3/ZrO_2//SAPO-34	18.7	70.5	1.0	-	20.2	8.3	1.166
420 °C	In_2O_3/YSZ	34.9	97.0	2.0	1.0	-	-	-
	In_2O_3/YSZ//SAPO-34	30.3	79.3	1.9	-	10.8	8.0	1.121
	In_2O_3/ZrO_2	31.9	98.2	0.5	1.3	-	-	-
	In_2O_3/ZrO_2//SAPO-34	32.5	90.0	1.3	-	6.5	2.2	0.661

to hydrocarbons. When In_2O_3/YSZ is combined with SAPO-34 as a tandem catalyst, light olefins are produced at all reaction temperatures due to the MTO reaction, confirming that SAPO-34 shifts the equilibrium right via selective C–C coupling. Our results show that the In_2O_3/YSZ//SAPO-34 tandem catalyst can show CO_2 conversion of 6.8%, and selectivity for light hydrocarbons (C_2–C_4) and light olefins ($C_2^=$–$C_4^=$) as high as 26.8% and 16.3% at 320 °C, respectively. As the temperature increases to 370 °C and 420 °C, the CO_2 conversion increases to 18.5% and 30.3%, respectively. Compared to the catalyst without the presence of SAPO-34, the CO selectivity is reduced to 74.7% and 79.3% at 370 °C and 420 °C, respectively, indicating that presence SAPO-34 shifts the equilibrium of methanol formation reaction to the right with decreasing the RWGS rate. As it can be seen in Fig. 3.11c,d, In_2O_3/ZrO_2 presents similar activity trends with In_2O_3/YSZ. The methanol selectivity of In_2O_3/ZrO_2 at 320 °C shows higher value of 77.6% compare to the In_2O_3/YSZ of 43.2%, and it can be attributed to the different CO_2 conversion. ZrO_2-supported In_2O_3 exhibits lower CO_2 conversion than that of In_2O_3/YSZ, and the low CO_2 conversion leads to the higher selectivity of methanol production in CO_2 hydrogenation.[214,215] Adsorption and activation of CO_2 can be promoted on the defects of metal oxides.[192,216] The oxygen vacancies defects in YSZ can be generated by addition of Y due to the charge neutrality. The abundance of oxygen vacancies on In_2O_3/YSZ//SAPO-34 facilitates CO_2 adsorption.[191] In addition, H_2O can dissociate on the defects of YSZ induced by Y^{3+} and form hydroxyl groups which are necessary for CO_2 chemisorption.[217] Our results show that bare YSZ displays a multitude of surface hydroxyl groups compared to bare ZrO_2 (Table 3.5). Overall, the higher CO_2 conversion observed on In_2O_3/YSZ compared to In_2O_3/ZrO_2 can be attributed to the large surface area and high affinities towards H_2 and CO_2 coupled with high oxygen vacancies, evidenced by N_2 isotherms and TPD analysis.

The stability of catalytic performance for In_2O_3/YSZ//SAPO-34 and In_2O_3/ZrO_2//SAPO-34 tandem catalysts for CO_2 hydrogenation reaction are evaluated at 420 °C for 45 h time-on-stream (TOS) as shown in Figure 3.12. In the beginning of the reaction, In_2O_3/YSZ//SAPO-34 shows higher CO_2 conversion of 31.3% than that of 25.4% for In_2O_3/ZrO_2//SAPO-34. CO is found to be the major product for both catalysts with the same initial CO selectivity of 81.6%. The initial selectivity of the light olefins for In_2O_3/YSZ//SAPO-34 and In_2O_3/ZrO_2//SAPO-34 are 6.3% and 9.7%, leading to light olefins yields of 0.844 mmol h^{-1} g^{-1} and 0.680 mmol h^{-1} g^{-1}, respectively. Both catalysts show no obvious decline in CO_2 conversion during 45 h TOS. However, the light olefins selectivity decreases to 4.2% for In_2O_3/ZrO_2//SAPO-34, and CO selectivity increases to 91.8% after 45 h TOS. Decreasing light olefins production can be

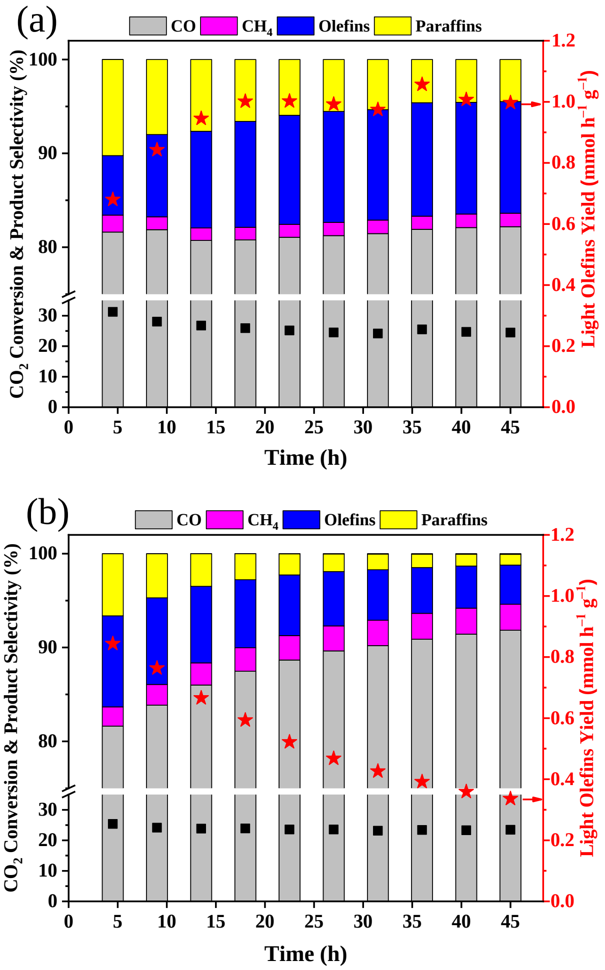

Figure 3.12. CO_2 conversion (black square), product selectivity (bar graph), and light olefins yield (red star) of (a) In_2O_3/YSZ//SAPO-34 and (b) In_2O_3/ZrO_2//SAPO-34 at 420 °C.

ascribed to the further reduction of the catalyst with CO, leading to the formation an amorphous molten state of In^0, which can block the active sites and decrease the methanol selectivity.[188] On the other hand, the light olefins selectivity for In_2O_3/YSZ//SAPO-34 starts to increase for the first 20 h TOS and stabilizes at 11.9% after 20 h. Initial increase observed for the light olefins selectivity can be attributed to the creation of oxygen vacancies in In_2O_3.[188] Formation of oxygen vacancies is facilitated in the presence of CO compared to H_2 due to the more exothermicity with CO than H_2.[190] CO formed by RWGS can reduce In_2O_3 and generate more oxygen vacancies, which will enhance the reaction rate.[189] Pustovarenko et al. observed that an induction period is required for MOF-derived In@Co catalyst to stabilize the methanol selectivity, which is associated with the formation of the active phase between the indium oxide and cobaltite phase.[218] After 45 h TOS, CO selectivity barely changes for In_2O_3/YSZ//SAPO-34 throughout the reaction, and the overall hydrocarbons selectivity maintains throughout the 45 h TOS. The longer stability in light olefins selectivity observed on In_2O_3/YSZ//SAPO-34 can be attributed to the higher metal dispersion and strong metal–support interaction which can inhibit the restructuring effects of the indium particles. In addition, In_2O_3/ZrO_2//SAPO-34 generates two times higher CH_4 selectivity (2.8%) than that of In_2O_3/YSZ//SAPO-34 (1.4%). Methanol is not observed throughout the reaction, indicating that all methanol converted to the C_2–C_4 hydrocarbons on the SAPO-34. Table 3.8 shows CO_2 conversion, product selectivity, and light olefins yield at the 45 h TOS for both catalysts. Our results show that CO_2 conversion is slightly higher on In_2O_3/YSZ//SAPO-34 compared to In_2O_3/ZrO_2//SAPO-34. Additionally, In_2O_3/YSZ//SAPO-34 presents hydrocarbons and light olefins selectivity's of 16.4% and 11.9%, while In_2O_3/ZrO_2//SAPO-34 shows much smaller selectivity's of 5.3% and 4.0%, respectively. This can lead to produce almost three times higher light olefins yield for In_2O_3/YSZ//SAPO-34 (0.997 mmol h^{-1} g^{-1}) compared to In_2O_3/ZrO_2//SAPO-34 (0.336 mmol h^{-1} g^{-1}). Among the olefins produced, $C_3^=$ shows the most selective product followed by $C_2^=$ and $C_4^=$ for In_2O_3/YSZ//SAPO-34.

Table 3.8. Catalytic performance in CO_2 hydrogenation of In_2O_3/YSZ//SAPO-34 and In_2O_3/ZrO_2//SAPO-34 at 45 h TOS.

Catalysts	X_{CO2} (%)	Product selectivity (%)								Light olefins yield (mmol h^{-1} g^{-1})
		CO	CH_4	Light olefins			Light paraffins			
				$C_2^=$	$C_3^=$	$C_4^=$	C_2°	C_3°	C_4°	
In_2O_3/YSZ//SAPO-34	24.5	82.2	1.4	3.8	7.1	1.0	0.4	2.2	1.9	0.997
In_2O_3/ZrO_2//SAPO-34	23.5	91.9	2.8	1.5	0.1	2.4	0.4	0.3	0.6	0.336

3.3.3 Characterization of spent catalysts

Carbon deposition in internal channels of zeolite during MTO reaction can be detrimental, resulting in deactivation.[201,219] The TGA profiles of the spent catalysts are plotted in Figure 3.13a. Both In_2O_3/YSZ//SAPO-34 and In_2O_3/ZrO_2//SAPO-34 shows a weight loss of 6.1% and 7.5%, respectively, at temperatures below 157 °C, which can be attributed to the desorption of water. At temperatures larger than 157 °C, only 5.3%, and 2.9% of weight loss are observed due to carbon gasification deposited inside the nano-sized SAPO-34, indicating high

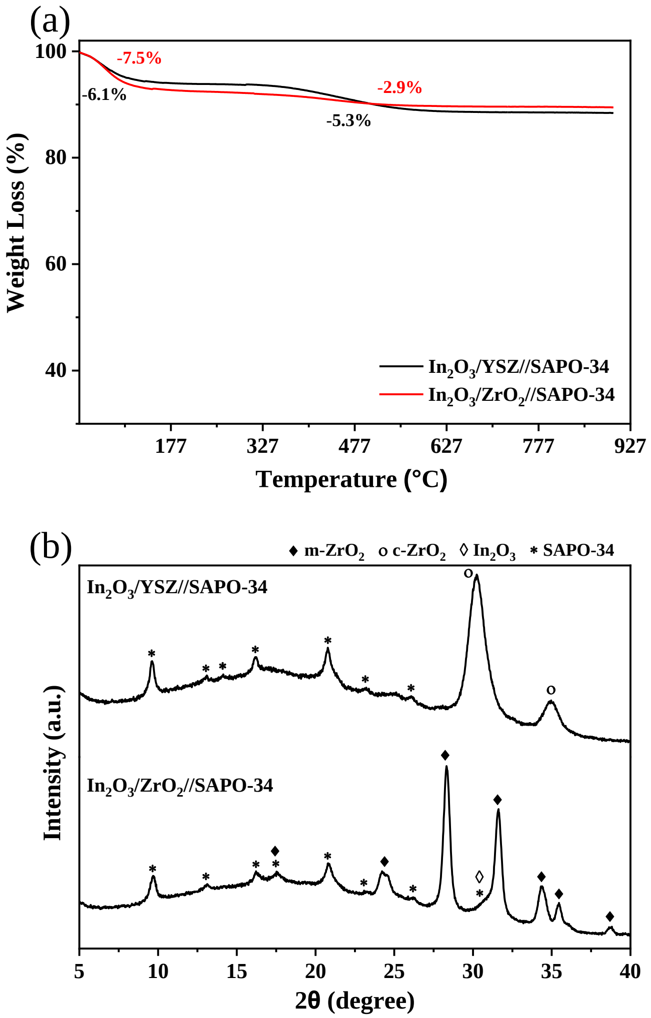

Figure 3.13. (a) TGA profiles and (b) XRD patterns of spent In_2O_3/YSZ//SAPO-34 and spent In_2O_3/ZrO_2//SAPO-34 after 45 h of reaction at 420 °C.

resistance to carbon deposition. This also implies that coking does not account for the decrease in methanol selectivity. In_2O_3/YSZ//SAPO-34 would present slightly higher amount of weight loss than In_2O_3/ZrO_2//SAPO-34 due to the larger amount of hydrocarbon yield with stable production during the 45 h TOS. The high carbon-resistant nature of SAPO-34 can also be determined by the $C_3^=/C_2^=$ ratio during the reaction. It is known that larger hydrocarbon production can decrease over SAPO-34 during MTO reaction because the intracrystalline diffusion of hydrocarbon species over SAPO-34 can turn into the intercrystallite diffusion by occurrence of coke deposition.[220] However, the $C_3^=/C_2^=$ ratio maintains stable activity after 15 h without a decline in the stabilized region as shown in Figure 3.14, indicating that there is no significant coking during direct CO_2 hydrogenation to light olefins reaction.

Figure 3.13b and Table 3.9 show XRD patterns and crystallite size of the spent catalysts after 45 h of CO_2 hydrogenation reaction at 420 °C. For the spent In_2O_3/YSZ//SAPO-34, the crystallite size of YSZ (7.4 nm) is identical to the fresh one, and no appreciable change in the structure is observed. Similarly, the spent In_2O_3/ZrO_2//SAPO-34 presents identical diffraction

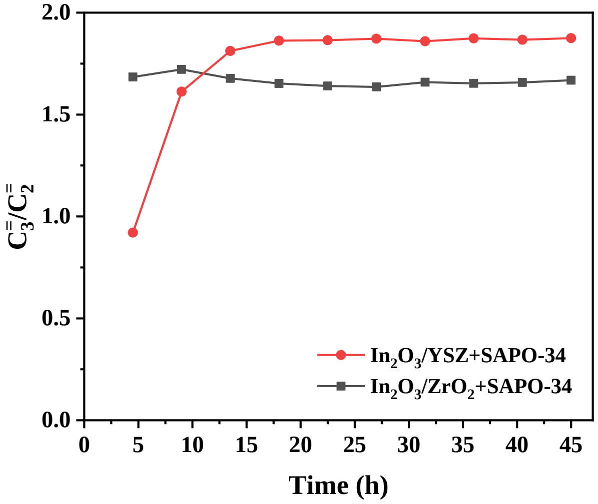

Figure 3.14. $C_3^=/C_2^=$ product ratio during 45 h of reaction at 420 °C for In_2O_3/YSZ//SAPO-34 and In_2O_3/ZrO_2//SAPO-34.

patterns of In_2O_3, ZrO_2, and SAPO-34 compared with the fresh catalyst. The crystallite size of ZrO_2 slightly increase to 20.0 nm from 18.0 nm, while the crystallite size of In_2O_3 remains the same as the fresh catalyst of 11.3 nm. This result might imply that In_2O_3 species has high resistance to sintering during the reaction.

Table 3.9. Crystallite size and lattice constant for spent In_2O_3/YSZ//SAPO-34 and spent In_2O_3/ZrO_2//SAPO-34 after 45 h of reaction at 420 °C.

Catalysts	Crystallite size (nm)		
	m-ZrO_2 (11−1)	c-ZrO_2 (111)	In_2O_3 (222)
In_2O_3/YSZ//SAPO-34	-	7.4	-
In_2O_3/ZrO_2//SAPO-34	20.0	-	11.3

The oxidation states of the chemical species presented in the spent catalysts were evaluated by XPS. As shown in Figure 3.15, the In 3d core level spectra of the spent In_2O_3/ZrO_2//SAPO-34 contain an additional peak located at 446.5 eV, which can be attributed to $In(OH)_3$ with 41.1%, possibly formed due to the reaction with H_2O.[221] In the case of the spent In_2O_3/YSZ//SAPO-34, the In 3d core level spectra shows only one oxidation state of In^{3+} as the fresh catalyst without $In(OH)_3$. Similarly, the Zr 3d core level spectra of the spent In_2O_3/ZrO_2//SAPO-34, contains an additional peak at 182.8 eV, which can be associated with the Zr^{4+} bonding with OH groups due to the hydroxylation of Zr^{4+} ions with 28.9%.[222] However, the spent In_2O_3/YSZ//SAPO-34 contains only peaks that are associated with the ZrO_2 lattice. The spent In_2O_3 catalysts supported on YSZ and ZrO_2 show similar In^{3+} binding energies as the fresh catalysts. The binding energy of Zr^{4+} in the spent catalysts shifts to the lower energies when compared to the fresh ones. This is possibly due to the fact that the part of the electrons remains in the oxygen vacancy, localizing the zirconium atoms during the reaction under the reducing environment.[223] The O 1s XPS data for the spent catalysts could not be analyzed due to the

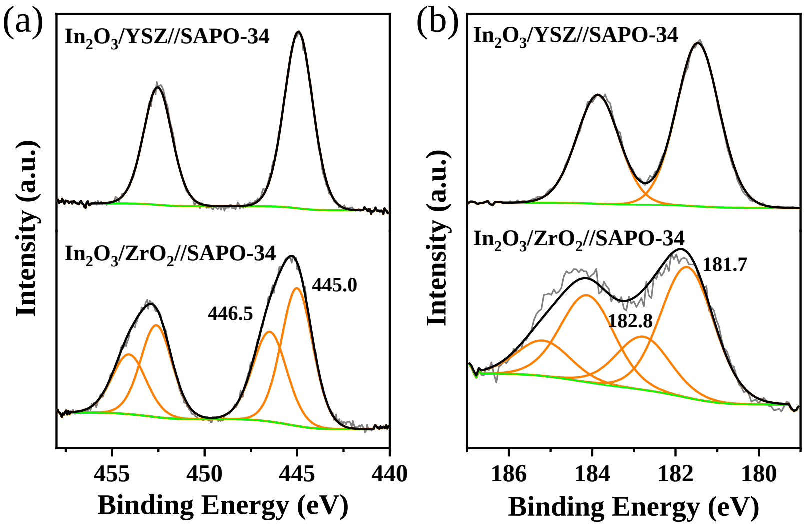

Figure 3.15. (a) In 3d and (b) Zr 3d XPS spectra of spent In_2O_3/YSZ//SAPO-34 and spent In_2O_3/ZrO_2//SAPO-34 after 45 h of reaction at 420 °C.

presence of SAPO-34. Therefore, we tested the activity of the supported In_2O_3 without the presence of the SAPO-34 at 420 °C for 45 h and analyzed them in XPS. As shown Figure 3.16, In_2O_3/ZrO_2 still contains peaks associated with $In(OH)_3$ and $Zr(OH)_4$ with 20.2% and 26.3%, respectively, whereas In_2O_3/YSZ has only In_2O_3 and ZrO_2 characteristic peaks. These results indicate that hydroxide formations do not related with the SAPO-34, but rather it can be directly associated with CO_2-to-methanol and MTO reactions. The water produced during the reaction can adsorb on the surface, leading to an increase in the amount of hydroxyl (OH) species, as

Table 3.10. Relative surface concentration of oxygen species of spent In_2O_3/YSZ and spent In_2O_3/ZrO_2 after 45 h of reaction measured by XPS.

	Catalysts	O_{latt}	O_{ads}	OH
320 °C	In_2O_3/YSZ	54.5	10.3	35.2
	In_2O_3/ZrO_2	51.7	11.8	36.5
420 °C	In_2O_3/YSZ	55.5	12.9	31.6
	In_2O_3/ZrO_2	58.1	23.6	18.2

shown in O 1s spectra compared to the fresh catalysts (Figure 3.16 and Table 3.10). The high amount of H_2O produced during CO_2 hydrogenation and MTO reactions can be detrimental to the catalytic activity and the methanol selectivity.[196] It is reported that the high concentration of H_2O can aggregate In species, thereby decreasing the metal distribution on the support, deactivating the methanol selectivity.[211] The amount of OH species on the spent In_2O_3/YSZ and In_2O_3/ZrO_2 surfaces after the reaction at 420 °C is calculated to be 31.6% and 18.2%, respectively by O 1s XPS results (Table 3.10). It is possible that the adsorbed OH species react with ZrO_2 and In_2O_3 to form $Zr(OH)_4$ and $In(OH)_3$. These results indicate that Zr ions in YSZ have more resistance to hydroxylation during the reaction. After H_2O adsorption, the defect oxygen concentration in In_2O_3 decreases due to the increased concentrations of OH and $In(OH)_3$ species on the surface. The higher amount of oxygen vacancy in the YSZ support can adopt more OH species without forming hydroxide of Zr species, preventing further formation of indium hydroxide, leading to stabilizing the performance. The surface Zr/O ratio for the spent In_2O_3/YSZ obtained by XPS increases to 83.8% from 34.9% observed on the fresh one, while the ratio for spent In_2O_3/ZrO_2 increases to 107.3% from the fresh one of 40.5% (Table 3.5). It can imply that ZrO_2-supported In_2O_3 shows higher reducibility than YSZ-supported In_2O_3, which is

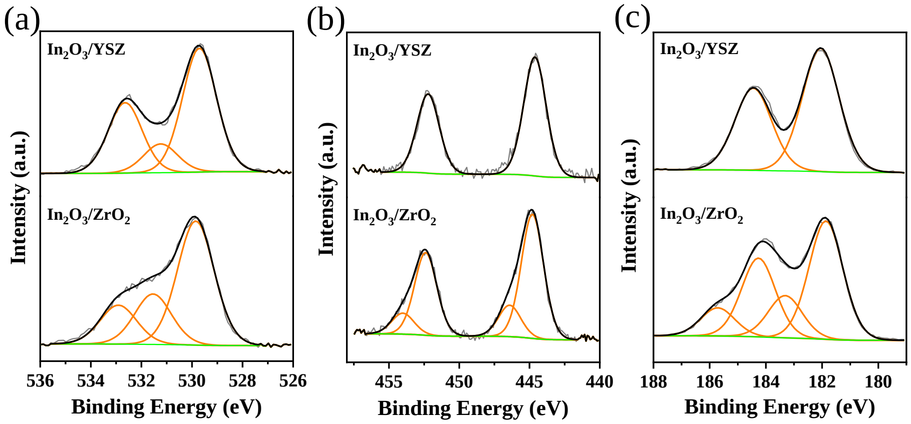

Figure 3.16. (a) O 1s, (b) In 3d, and (b) Zr 3d XPS spectra of spent In_2O_3/YSZ and spent In_2O_3/ZrO_2 after 45 h of reaction at 420 °C.

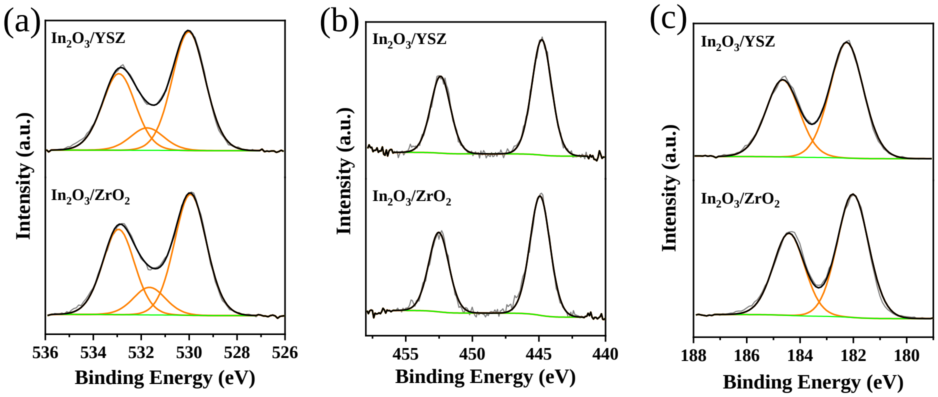

Figure 3.17. (a) O 1s, (b) In 3d, and (b) Zr 3d XPS spectra of spent In_2O_3/YSZ and spent In_2O_3/ZrO_2 after 45 h of reaction at 320 °C.

in good agreement with H_2-TPR data. High reducibility can lead to water-induced sintering or hydroxylation, which can decrease the methanol formation. M. S. Frei et al. studied Pd-promoted In_2O_3 for CO_2 hydrogenation to methanol, and they observed deterioration of the performance for the Pd atoms deposited onto the In_2O_3.[224] It shows negative rate dependence on the water pressure, speculating that less facilitated water desorption by too much H_2 spillover leaded to over-reduction and water-induced sintering of In_2O_3 crystals. On the other hand, the spent catalysts tested for 45 h at lower temperature of 320 °C present similar amount of OH species for In_2O_3/YSZ (35.2%) and In_2O_3/ZrO_2 (31.6%) (Figure 3.17). In addition, the XPS spectra of In 3d and Zr 3d tested at 593 K do not show any $In(OH)_3$ or $Zr(OH)_4$ for both YSZ and ZrO_2-supported In_2O_3 unlike the ones tested at 420 °C. It is known that the zirconium hydroxide can be observed, upon exposure to the H_2O in the bare zirconia. OH groups from water molecules are physisorbed on the ZrO_2 surface followed by the penetration of OH species into the substrate lattice forming zirconium hydroxide with heat treatment.[225] It is hypothesized that the OH can also migrate to the In species, transforming indium to the indium hydroxide. This can emphasize the beneficial of using YSZ support exhibiting high resistance to hydroxylation for tandem reactions applied at high reaction temperature.

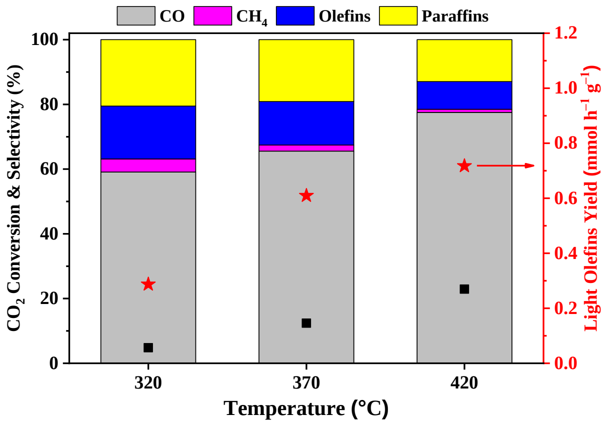

Figure 3.18. CO_2 conversion (black square), product selectivity (bar graph), and light olefins yield (red star) of In_2O_3/ZrO_2//SAPO-34^{COM}.

Figure 3.18 shows CO_2 hydrogenation performance for In_2O_3/ZrO_2 combined with commercial SAPO-34^{COM} in a temperature range of 320–420 °C. At 320 K, the CO selectivity (59.2%) is similar to the value of tandem catalyst composed of developed nano-sized SAPO-34 of 59.2% (Figure 3.11d). At the high temperature of 420 °C, In_2O_3/ZrO_2//SAPO-34 shows a higher CO selectivity (90.0%) than that for In_2O_3/ZrO_2//SAPO-34^{COM} (77.5%). This is because In_2O_3/ZrO_2//SAPO-34 shows higher CO_2 conversion of 32.5% compared to In_2O_3/ZrO_2//SAPO-34^{COM} of 27.0% since small crystallite size of nano-sized SAPO-34 can shift the CO_2 to methanol reaction more. However, due to smaller diffusion path inside SAPO-34 channel, produced methanol converts to more light olefins rather than further transforming to paraffins. The light olefins/paraffins (O/P) ratio of hydrocarbon products for In_2O_3/ZrO_2//SAPO-34 is always higher than SAPO-34^{COM} (Table 3.11). The O/P ratio for the tandem In_2O_3/ZrO_2//SAPO-34 almost 4.5-times higher than that for In_2O_3/ZrO_2//SAPO-34^{COM} at the reaction of temperature of 420 °C. This data indicates that small crystallite with a short diffusion length of nano-sized zeolite is beneficial to produce high light olefins selectivity. However, acidity cannot be ruled out for considering light olefins selectivity, as low acidity with low Si/Al ratio in zeolites can

Table 3.11. Produced O/P ratio for In_2O_3/ZrO_2//SAPO-34 and In_2O_3/ZrO_2//SAPO-34^{COM} in CO_2 hydrogenation reaction.

Catalysts	Temperatures		
	320 °C	370 °C	420 °C
In_2O_3/ZrO_2//SAPO-34	1.78	2.44	3.05
In_2O_3/ZrO_2//SAPO-34^{COM}	0.80	0.70	0.66

produce high O/P ratio of the products.[226,227] The developed nano-sized SAPO-34 and commercially obtained SAPO-34^{COM} has Si/Al ratio of 0.3 and 1, respectively. Therefore, it is possible that the higher O/P ratio of products in In_2O_3/ZrO_2//SAPO-34 could be related with the acidity. This work has focused on the supported In_2O_3 for obtaining stable CO_2 to light olefins, therefore investigating different physical and chemical structures of the zeolites for the tandem catalysts will need to be considered in future research.

3.4 Conclusions

In this work, we have prepared In_2O_3/YSZ//SAPO-34 tandem catalysts for stable and selective synthesis of light olefins by CO_2 hydrogenation. The yield of light olefins reaches to 0.997 mmol h^{-1} g^{-1} with selectivity of 11.9% (66.9% without CO) over 45 h TOS at 420 °C without any deactivation. It is concluded that the large amount of oxygen vacancies and strong metal–support interaction on YSZ-supported In_2O_3 can prevent In species from hydroxylation and over-reduction, stabilizing the active sites. However, In_2O_3 supporting on regular ZrO_2 presents a decline of light olefins production in time because water produced can fill the vacancies, generating indium hydroxide and zirconium hydroxide at high reaction temperature of 420 °C. In addition, the In_2O_3 can be transformed to the molten In^0 due to the low metal–support interaction. The developed nano-sized SAPO-34 synthesized by microwave heating shows stable light olefins selectivity with high resistance to carbon formation due to low crystal size with high external surface areas. The new findings of this work can pave the way for integrating YSZ in CO_2 hydrogenation for rational design of the tandem catalyst.

SUMMARY AND FUTURE WORK

Two main reactions are investigated for CO_2 utilization: methane reforming and CO_2 hydrogenation. First, TRM which CO_2 reacts with CH_4, H_2O, and O_2 is studied over nanotubular NiCe@SiO_2 multi–yolk–shell catalyst. The conventional impregnated catalyst shows fast deactivation because of severe carbon deposition on the catalyst. However, the developed yolk–shell catalyst exhibits high resistance to carbon deposition due to the facile CO* desorption in the confined morphology, which minimizes the Boudouard reaction. The catalyst presents distinct characteristic behavior at various feed gas streams under TRM, where carbon deposition or metal re-oxidation is correlated with the yolk size and Ce^{3+} concentration. Next, the yolk–shell catalyst is developed by doping with Pt forming SAA structure with Ni species to further strengthen the resistance against the carbon formation. The yolk–shell morphology with SAA structure shows high stability in DRM reaction at low temperature of 500 °C due to the enhanced Ni reducibility with high Pt–Ni interaction. The 0.25 wt% of Pt is the optimum loading to create the well dispersed Pt–Ni SAA structure, whereas a high Pt-loaded catalyst creates Pt nanoparticles, reducing the Pt–Ni interactions. The developed catalyst operated at wide temperature ranges is proven to be effective for the reactions generating carbon species. For the future work, more detailed experiments can be performed to investigate the behavior of intermediate species and carbon generation/removal reaction during methane reforming by DRIFTS-MS and isotope exchange methods. In addition, a computational study such as density-functional theory (DFT) can be incorporated to investigate how the Pt–Ni SAA structure can alter the reactants dissociation path. Fundamental understanding of the unique structured yolk–

shell SAA will guide us to prepare catalysts with low cost so that the overall methane reforming reactions can be feasible and carried out in a worldwide region.

Secondly, the In_2O_3/YSZ//SAPO-34 tandem catalyst is prepared for CO_2 hydrogenation to generate light olefins. Combination of In_2O_3/YSZ metal oxide and SAPO-34 zeolite in a single reactor can promote shifting of the methanol production equilibrium to the right, leading to a high light olefins selectivity. The light olefins selectivity for In_2O_3/YSZ//SAPO-34 shows steady production of 11.9% during 45 h of reaction whereas the tandem catalyst with conventional ZrO_2-supported catalyst behaves decreasing in selectivity. The stable performance of the YSZ-supported catalyst can be explained by higher oxygen vacancy in YSZ and stronger In_2O_3–YSZ interaction compared to the ZrO_2-supported In_2O_3. The water produced during the reaction can facilitate hydroxide formation and overreduction of In_2O_3 for ZrO_2-based one, inhibiting methanol formation and decreasing the light olefins production. On the other hand, YSZ with high oxygen vacancies presents high resistance to hydroxide formation and reduction of active species, maintaining the targeted production rates. To obtain high performances, the tandem catalysts should be combined in a well-tuned way with high proximity. A capsule catalyst such as core–shell morphology for the tandem catalyst can benefit the desired production rate by lower adsorption energy and large surface area of zeolite in the shell. The high proximity between core and shell structure can demonstrate better mass transfer and diffusion by minimizing the side reactions, enhancing the light olefins selectivity. In addition, the induction heating method can be applied to the tandem catalyst system. Incorporating inductive materials can solve the temperature mismatch between two different reactions in a single reactor, which can overcome the different thermodynamics. These studies highlight the potential approach to design the catalysts for industrially relevant processes to utilize CO_2 to produce useful chemicals, which can contribute to both carbon neutrality and human energy use.

REFERENCES

1. Masson-Delmotte, V. *et al.* Global warming of 1.5°C. IPCC Press (2018).
2. U. S. Energy Information Administration. International Energy Outlook 2019. https://www.eia.gov/outlooks/archive/ieo19/pdf/ieo2019.pdf (accessed 2019-09-24).
3. Song, C. Global challenges and strategies for control, conversion and utilization of CO_2 for sustainable development involving energy, catalysis, adsorption and chemical processing. *Catal. Today* **115**, 2–32 (2006).
4. Lashof, D. A. & Ahuja, D. R. Relative contributions of greenhouse gas emissions to global warming. *Nature* **344**, 529–531 (1990).
5. Cassia, R., Nocioni, M., Correa-Aragunde, N. & Lamattina, L. Climate Change and the Impact of Greenhouse Gasses: CO_2 and NO, Friends and Foes of Plant Oxidative Stress. *Front. Plant Sci.* **9**, 1–11 (2018).
6. Omri, A. CO_2 emissions, energy consumption and economic growth nexus in MENA countries: Evidence from simultaneous equations models. *Energy Econ.* **40**, 657–664 (2013).
7. Fawzy, S., Osman, A. I., Doran, J. & Rooney, D. W. Strategies for mitigation of climate change: a review. *Environ. Chem. Lett.* **18**, 2069–2094 (2020).
8. Gabrielli, P., Gazzani, M. & Mazzotti, M. The Role of Carbon Capture and Utilization, Carbon Capture and Storage, and Biomass to Enable a Net-Zero-CO_2 Emissions Chemical Industry. *Ind. Eng. Chem. Res.* **59**, 7033–7045 (2020).
9. Jang, W. J., Shim, J. O., Kim, H. M., Yoo, S. Y. & Roh, H. S. A review on dry reforming of methane in aspect of catalytic properties. *Catal. Today* **324**, 15–26 (2019).
10. Song, C. & Pan, W. Tri-reforming of methane: A novel concept for catalytic production of industrially useful synthesis gas with desired H_2/CO ratios. *Catal. Today* **98**, 463–484 (2004).
11. Peter, S. C. Reduction of CO_2 to chemicals and fuels: A solution to global warming and energy crisis. *ACS Energy Lett.* **3**, 1557–1561 (2018).
12. Ampelli, C., Perathoner, S. & Centi, G. CO_2 utilization: an enabling element to move to a resource- and energy-efficient chemical and fuel production. *Philos. Trans. R. Soc. A* **373**, 20140177 (2015).
13. Saeidi, S., Amin, N. A. S. & Rahimpour, M. R. Hydrogenation of CO_2 to value-added products—A review and potential future developments. *J. CO_2 Util.* **5**, 66–81 (2014).
14. Whipple, D. T. & Kenis, P. J. A. Prospects of CO_2 utilization via direct heterogeneous electrochemical reduction. *J. Phys. Chem. Lett.* **1**, 3451–3458 (2010).
15. Yu, K. M. K., Curcic, I., Gabriel, J. & Tsang, S. C. E. Recent advances in CO_2 capture and utilization. *ChemSusChem* **1**, 893–899 (2008).

16. Jiang, Z., Xiao, T., Kuznetsov, V. L. & Edwards, P. P. Turning carbon dioxide into fuel. *Philos. Trans. A. Math. Phys. Eng. Sci.* **368**, 3343–3364 (2010).

17. Freund, H.-J. & Roberts, M. W. Surface chemistry of carbon dioxide. *Surf. Sci. Rep.* **25**, 225–273 (1996).

18. Kang, J. S., Kim, D. H., Lee, S. D., Hong, S. I. & Moon, D. J. Nickel-based tri-reforming catalyst for the production of synthesis gas. *Appl. Catal. A Gen.* **332**, 153–158 (2007).

19. Sadeghi, M., Jafari, M., Yari, M. & Mahmoudi, S. M. S. Exergoeconomic assessment and optimization of a syngas production system with a desired H_2/CO ratio based on methane tri-Reforming Process. *J. CO_2 Util.* **25**, 283–301 (2018).

20. Zhao, X. *et al.* NiMg/ceria-zirconia cylindrical pellet catalysts for tri-reforming of surrogate biogas. *Ind. Eng. Chem. Res.* **57**, 845–855 (2018).

21. Minutillo, M. & Perna, A. A novel approach for treatment of CO_2 from fossil fired power plants, Part A: The integrated systems ITRPP. *Int. J. Hydrogen Energy* **34**, 4014–4020 (2009).

22. Pichas, C., Pomonis, P., Petrakis, D. & Ladavos, A. Kinetic study of the catalytic dry reforming of CH_4 with CO_2 over $La_{2-x}Sr_xNiO_4$ perovskite-type oxides. *Appl. Catal. A Gen.* **386**, 116–123 (2010).

23. Guczi, L. *et al.* Methane dry reforming with CO_2: A study on surface carbon species. *Appl. Catal. A Gen.* **375**, 236–246 (2010).

24. Son, I. H. *et al.* Study on coke formation over Ni/γ-Al_2O_3, Co-Ni/γ-Al_2O_3, and Mg-Co-Ni/γ-Al_2O_3 catalysts for carbon dioxide reforming of methane. *Fuel* **136**, 194–200 (2014).

25. Zhao, X. *et al.* In situ preparation of Ni nanoparticles in cerium-modified silica aerogels for coking- and sintering-resistant dry reforming of methane. *New J. Chem.* **41**, 4869–4878 (2017).

26. Lee, S. H. *et al.* Tri-reforming of CH_4 using CO_2 for production of synthesis gas to dimethyl ether. *Catal. Today* **87**, 133–137 (2003).

27. Dwivedi, A., Gudi, R. & Biswas, P. An improved tri-reforming based methanol production process for enhanced CO_2 valorization. *Int. J. Hydrogen Energy* **42**, 23227–23241 (2017).

28. Luyben, W. L. Control of parallel dry methane and steam methane reforming processes for Fischer-Tropsch syngas. *J. Process Control* **39**, 77–87 (2016).

29. Bian, Z., Wang, Z. & Kawi, S. Ni-phyllosilicate structure derived Ni–SiO_2–MgO catalysts for bi-reforming applications: acidity, basicity and thermal stability. *Catal. Sci. Technol.* **8**, 1730–1742 (2018).

30. Kathiraser, Y. *et al.* Highly active and coke resistant Ni/SiO_2 catalysts for oxidative reforming of model biogas: Effect of low ceria loading. *J. CO_2 Util.* **19**, 284–295 (2017).

31. Singha, R. K. *et al.* Energy efficient methane tri-reforming for synthesis gas production over highly coke resistant nanocrystalline Ni-ZrO_2 catalyst. *Appl. Energy* **178**, 110–125 (2016).

32. Zhang, Y., Zhang, S., Gossage, J. L., Lou, H. H. & Benson, T. J. Thermodynamic analyses of tri-reforming reactions to produce syngas. *Energy and Fuels* **28**, 2717–2726 (2014).

33. García-Vargas, J. M., Valverde, J. L., Díez, J., Dorado, F. & Sánchez, P. Catalytic and kinetic analysis of the methane tri-reforming over a Ni-Mg/β-SiC catalyst. *Int. J. Hydrogen Energy* **40**, 8677–8687 (2015).

34. Schmal, M., Toniolo, F. S. & Kozonoe, C. E. Perspective of catalysts for (Tri) reforming of natural gas and flue gas rich in CO_2. *Appl. Catal. A Gen.* **568**, 23–42 (2018).

35. Wang, J. B., Tai, Y. L., Dow, W. P. & Huang, T. J. Study of ceria-supported nickel catalyst and effect of yttria doping on carbon dioxide reforming of methane. *Appl. Catal. A Gen.* **218**, 69–79 (2001).

36. Pino, L., Vita, A., Cipitì, F., Laganà, M. & Recupero, V. Hydrogen production by methane tri-reforming process over Ni–ceria catalysts: Effect of La-doping. *Appl. Catal. B Environ.* **104**, 64–73 (2011).

37. García-Vargas, J. M., Valverde, J. L., Díez, J., Sánchez, P. & Dorado, F. Preparation of Ni-Mg/β-SiC catalysts for the methane tri-reforming: Effect of the order of metal impregnation. *Appl. Catal. B Environ.* **164**, 316–323 (2015).

38. Wang, S. & Lu, G. Q. Role of CeO_2 in Ni/CeO_2–Al_2O_3 catalysts for carbon dioxide reforming of methane. *Appl. Catal. B Environ.* **19**, 267–277 (1998).

39. Deganello, F. & Martorana, A. Phase analysis and oxygen storage capacity of ceria-lanthana-based TWC promoters prepared by sol-gel routes. *J. Solid State Chem.* **163**, 527–533 (2002).

40. Walker, D. M., Pettit, S. L., Wolan, J. T. & Kuhn, J. N. Synthesis gas production to desired hydrogen to carbon monoxide ratios by tri-reforming of methane using Ni-MgO-(Ce,Zr)O_2 catalysts. *Appl. Catal. A Gen.* **445–446**, 61–68 (2012).

41. Singha, R. K. *et al.* Ni nanocluster on modified CeO_2–ZrO_2 nanoporous composite for tri-reforming of methane. *Catal. Sci. Technol.* **6**, 7122–7136 (2016).

42. Yao, Q., Lu, Z. H., Zhang, Z., Chen, X. & Lan, Y. One-pot synthesis of core-shell Cu@SiO_2 nanospheres and their catalysis for hydrolytic dehydrogenation of ammonia borane and hydrazine borane. *Sci. Rep.* **4**, 4–11 (2014).

43. Ghosh Chaudhuri, R. & Paria, S. Core/shell nanoparticles: Classes, properties, synthesis mechanisms, characterization, and applications. *Chem. Rev.* **112**, 2373–2433 (2012).

44. Wang, F., Xu, L. & Shi, W. Syngas production from CO_2 reforming with methane over core-shell Ni@SiO_2 catalysts. *J. CO_2 Util.* **16**, 318–327 (2016).

45. Li, Z., Li, M., Bian, Z., Kathiraser, Y. & Kawi, S. Design of highly stable and selective core/yolk–shell nanocatalysts—A review. *"Applied Catal. B, Environ.* **188**, 324–341 (2016).

46. Li, Z. *et al.* Silica-based micro- and mesoporous catalysts for dry reforming of methane. *Catal. Sci. Technol.* **8**, 2763–2778 (2018).

47. Bian, Z. & Kawi, S. Sandwich-like silica@Ni@silica multicore–shell catalyst for the low-temperature dry reforming of methane: Confinement effect against carbon formation. *ChemCatChem* **10**, 320–328 (2018).

48. Li, Z. & Kawi, S. Multi-Ni@Ni phyllosilicate hollow sphere for CO_2 reforming of CH_4: influence of Ni precursors on structure, sintering, and carbon resistance. *Catal. Sci. Technol.* **8**, 1915–1922 (2018).

49. Ashok, J., Ang, M. L. & Kawi, S. Enhanced activity of CO_2 methanation over Ni/CeO_2-ZrO_2 catalysts: Influence of preparation methods. *Catal. Today* **281**, 304–311 (2017).

50. Li, Z., Kathiraser, Y., Ashok, J., Oemar, U. & Kawi, S. Simultaneous tuning porosity and basicity of nickel@nickel−magnesium phyllosilicate core−shell catalysts for CO_2 reforming of CH_4. *Langmuir* **30**, 14694–14705 (2014).

51. Li, Z., Kathiraser, Y. & Kawi, S. Facile synthesis of high surface area yolk–shell Ni@Ni embedded SiO_2 via Ni phyllosilicate with enhanced performance for CO_2 reforming of CH_4. *ChemCatChem* **7**, 160–168 (2015).

52. Zhao, X., Li, H., Zhang, J., Shi, L. & Zhang, D. Design and synthesis of NiCe@m-SiO_2 yolk-shell framework catalysts with improved coke- and sintering-resistance in dry reforming of methane. *Int. J. Hydrogen Energy* **41**, 2447–2456 (2016).

53. Liu, J. *et al.* Yolk-shell hybrid materials with a periodic mesoporous organosilica shell: Ideal nanoreactors for selective alcohol oxidation. *Adv. Funct. Mater.* **22**, 591–599 (2012).

54. Liu, J. *et al.* Yolk/shell nanoparticles: new platforms for nanoreactors, drug delivery and lithium-ion batteries. *Chem. Commun.* **47**, 12578 (2011).

55. Kuo, C. H. *et al.* Yolk-shell nanocrystal@ZIF-8 nanostructures for gas-phase heterogeneous catalysis with selectivity control. *J. Am. Chem. Soc.* **134**, 14345–14348 (2012).

56. Wang, S., Zhang, M. & Zhang, W. Yolk-shell catalyst of single Au nanoparticle encapsulated within hollow mesoporous silica microspheres. *ACS Catal.* **1**, 207–211 (2011).

57. Li, Z., Wang, Z., Jiang, B. & Kawi, S. Sintering resistant Ni nanoparticles exclusively confined within SiO_2 nanotubes for CH_4 dry reforming. *Catal. Sci. Technol.* **8**, 3363–3371 (2018).

58. Li, Z. & Sibudjing, K. Facile Synthesis of Multi-Ni-Core@Ni Phyllosilicate@CeO_2 Shell Hollow Spheres with High Oxygen Vacancy Concentration for Dry Reforming of CH_4. *ChemCatChem* **10**, 2994–3001 (2018).

59. Li, Z., Mo, L., Kathiraser, Y. & Kawi, S. Yolk−satellite−shell structured Ni−Yolk@Ni@SiO_2 nanocomposite: Superb catalyst toward methane CO_2 reforming reaction. *ACS Catal.* **4**, 1526–1536 (2014).

60. Li, L. *et al.* Highly Active and Stable Lanthanum-doped Core-Shell-structured Ni@SiO_2 Catalysts for the Partial Oxidation of Methane to Syngas. *ChemCatChem* **5**, 3781–3787 (2013).

61. Majewski, A. J. & Wood, J. Tri-reforming of methane over Ni@SiO_2 catalyst. *Int. J. Hydrogen Energy* **39**, 12578–12585 (2014).

62. Jiang, H., Li, H., Xu, H. & Zhang, Y. Preparation of Ni/$Mg_xTi_{1-x}O$ catalysts and investigation on their stability in tri-reforming of methane. *Fuel Process. Technol.* **88**, 988–995 (2007).

63. Dahlberg, K. A. & Schwank, J. W. Synthesis of Ni@SiO_2 nanotube particles in a water-in-oil microemulsion template. *Chem. Mater.* **24**, 2635–2644 (2012).

64. Das, S. *et al.* Silica–ceria sandwiched Ni core–shell catalyst for low temperature dry reforming of biogas: Coke resistance and mechanistic insights. *Appl. Catal. B Environ.* **230**, 220–236 (2018).

65. Zhu, J. *et al.* Synthesis gas production from CO_2 reforming of methane over Ni-Ce/SiO_2 catalyst: The effect of calcination ambience. *Int. J. Hydrogen Energy* **38**, 117–126 (2013).

66. Yang, T. *et al.* Hierarchical mesoporous yolk–shell structured carbonaceous nanospheres for high performance electrochemical capacitive energy storage. *Chem. Commun.* **51**, 2518–2521 (2015).

67. Ashok, J. & Kawi, S. Steam reforming of toluene as a biomass tar model compound over CeO_2 promoted Ni/CaO–Al_2O_3 catalytic systems. *Int. J. Hydrogen Energy* **38**, 13938–13949 (2013).

68. Zhang, L., Li, M., Ren, T., Liu, X. & Yuan, Z.-Y. Ce-modified Ni nanoparticles encapsulated in SiO_2 for CO_x-free hydrogen production via ammonia decomposition. *Int. J. Hydrogen Energy* **40**, 2648–2656 (2015).

69. Du, X., Zhang, D., Shi, L., Gao, R. & Zhang, J. Morphology dependence of catalytic properties of Ni/CeO_2 nanostructures for carbon dioxide reforming of methane. *J. Phys. Chem. C* **116**, 10009–10016 (2012).

70. Lakshmanan, P., Kim, M. S. & Park, E. D. A highly loaded Ni@SiO_2 core-shell catalyst for CO methanation. *Appl. Catal. A Gen.* **513**, 98–105 (2016).

71. Kang, K. M., Kim, H. W., Shim, I. W. & Kwak, H. Y. Catalytic Test of Supported Ni Catalysts with Core/Shell Structure for Dry Reforming of Methane. *Fuel Process. Technol.* **92**, 1236–1243 (2011).

72. Iglesias, D. & Melchionna, M. Enter the tubes: Carbon nanotube endohedral catalysis. *Catalysts* **9**, 128 (2019).

73. Pino, L., Vita, A., Laganà, M. & Recupero, V. Hydrogen from biogas: Catalytic tri-reforming process with Ni/La–Ce–O mixed oxides. *"Applied Catal. B, Environ.* **148–149**, 91–105 (2014).

74. Li, B., Xu, X. & Zhang, S. Synthesis gas production in the combined CO_2 reforming with partial oxidation of methane over Ce-promoted Ni/SiO_2 catalysts. *Int. J. Hydrogen Energy* **38**, 890–900 (2013).

75. Krause, K. R., Schabes-Retchkiman, P. & Schmidt, L. D. Microstructure of Rh-Ce particles

on silica: interactions between Ce and SiO_2. *J. Catal.* **134**, 204–219 (1992).

76. Farmer, J. A. & Campbell, C. T. Ceria maintains smaller metal catalyst particles by strong metal-support bonding. *Science* **329**, 933–936 (2010).

77. Nagai, Y. *et al.* Sintering inhibition mechanism of platinum supported on ceria-based oxide and Pt-oxide-support interaction. *J. Catal.* **242**, 103–109 (2006).

78. Kim, J.-H., Suh, D. J., Park, T.-J. & Kim, K.-L. Effect of metal particle size on coking during CO_2 reforming of CH over Ni–alumina aerogel catalysts. *Appl. Catal. A Gen.* **197**, 191–200 (2000).

79. Li, Z., Hu, X., Zhang, L., Liu, S. & Lu, G. Steam reforming of acetic acid over Ni/ZrO_2 catalysts: Effects of nickel loading and particle size on product distribution and coke formation. *Appl. Catal. A Gen.* **417–418**, 281–289 (2012).

80. Luisetto, I., Tuti, S., Battocchio, C., Lo Mastro, S. & Sodo, A. Ni/CeO_2–Al_2O_3 catalysts for the dry reforming of methane: The effect of $CeAlO_3$ content and nickel crystallite size on catalytic activity and coke resistance. *Appl. Catal. A Gen.* **500**, 12–22 (2015).

81. Zhang, J., Wang, H. & Dalai, A. K. Effects of metal content on activity and stability of Ni-Co bimetallic catalysts for CO_2 reforming of CH_4. *Appl. Catal. A Gen.* **339**, 121–129 (2008).

82. Christensen, K. O., Chen, D., Lødeng, R. & Holmen, A. Effect of supports and Ni crystal size on carbon formation and sintering during steam methane reforming. *Appl. Catal. A Gen.* **314**, 9–22 (2006).

83. San-José-Alonso, D., Juan-Juan, J., Illán-Gómez, M. J. & Román-Martínez, M. C. Ni, Co and bimetallic Ni–Co catalysts for the dry reforming of methane. *Appl. Catal. A Gen.* **371**, 54–59 (2009).

84. Alstrup, I. A new model explaining carbon filament growth on nickel, iron, and Ni–Cu Alloy Catalysts. *J. Catal.* **109**, 241–251 (1988).

85. Singha, R. K., Shukla, A., Yadav, A., Sivakumar Konathala, L. N. & Bal, R. Effect of metal-support interaction on activity and stability of Ni-CeO_2 catalyst for partial oxidation of methane. *Appl. Catal. B Environ.* **202**, 473–488 (2017).

86. Khajenoori, M., Rezaei, M. & Meshkani, F. Characterization of CeO_2 promoter of a nanocrystalline Ni/MgO catalyst in dry reforming of methane. *Chem. Eng. Technol.* **37**, 957–963 (2014).

87. Hou, Z. *et al.* Deactivation of Ni catalysts during methane autothermal reforming with CO_2 and O_2 in a fluidized-bed reactor. *J. Catal.* **250**, 331–341 (2007).

88. Lu, Y., Xue, J., Yu, C., Liu, Y. & Shen, S. Mechanistic investigations on the partial oxidation of methane to synthesis gas over a nickel-on-alumina catalyst. *Appl. Catal. A Gen.* **174**, 121–128 (1998).

89. Enger, B. C., Lødeng, R. L. & Holmen, A. Modified cobalt catalysts in the partial oxidation of methane at moderate temperatures. *J. Catal.* **262**, 188–198 (2009).

90. Schwab, E., Milanov, A., Schunk, S. A., Behrens, A. & Schödel, N. Dry reforming and reverse water gas shift: Alternatives for syngas production? *Chemie-Ingenieur-Technik* **87**, 347–353 (2015).

91. Gao, Y., Jiang, J., Meng, Y., Yan, F. & Aihemaiti, A. A review of recent developments in hydrogen production via biogas dry reforming. *Energy Convers. Manag.* **171**, 133–155 (2018).

92. Elsayed, N. H., Roberts, N. R. M., Joseph, B. & Kuhn, J. N. Low temperature dry reforming of methane over Pt–Ni–Mg/ceria–zirconia catalysts. *Appl. Catal. B Environ.* **179**, 213–219 (2015).

93. Wang, Y. *et al.* Low-Temperature Catalytic CO_2 Dry Reforming of Methane on Ni-Si/ZrO_2 Catalyst. *ACS Catal.* **8**, 6495–6506 (2018).

94. Han, J. W., Park, J. S., Choi, M. S. & Lee, H. Uncoupling the size and support effects of Ni catalysts for dry reforming of methane. *Appl. Catal. B Environ.* **203**, 625–632 (2017).

95. Akri, M. *et al.* Atomically dispersed nickel as coke-resistant active sites for methane dry reforming. *Nat. Commun.* **10**, 1–10 (2019).

96. Arora, S. & Prasad, R. An overview on dry reforming of methane: Strategies to reduce carbonaceous deactivation of catalysts. *RSC Adv.* **6**, 108668–108688 (2016).

97. Zhang, Q. *et al.* A sintering and carbon-resistant Ni-SBA-15 catalyst prepared by solid-state grinding method for dry reforming of methane. *J. CO_2 Util.* **17**, 10–19 (2017).

98. Wang, Y., Yao, L., Wang, S., Mao, D. & Hu, C. Low-temperature catalytic CO_2 dry reforming of methane on Ni-based catalysts: A review. *Fuel Process. Technol.* **169**, 199–206 (2018).

99. Kim, S. *et al.* Activity and stability of NiCe@SiO_2 multi–yolk–shell nanotube catalyst for tri-reforming of methane. *Appl. Catal. B Environ.* **259**, 118037 (2019).

100. Bu, K. *et al.* Methane dry reforming over boron nitride interface-confined and LDHs-derived Ni catalysts. *Appl. Catal. B Environ.* **252**, 86–97 (2019).

101. Bian, Z., Suryawinata, I. Y. & Kawi, S. Highly carbon resistant multicore-shell catalyst derived from Ni-Mg phyllosilicate nanotubes@silica for dry reforming of methane. *Appl. Catal. B Environ.* **195**, 1–8 (2016).

102. Das, S. *et al.* Core-shell structured catalysts for thermocatalytic, photocatalytic, and electrocatalytic conversion of CO_2. *Chem. Soc. Rev.* **49**, 2937–3004 (2020).

103. Chen, S., Zaffran, J. & Yang, B. Descriptor design in the computational screening of Ni-based catalysts with balanced activity and stability for dry reforming of methane reaction. *ACS Catal.* **10**, 3074–3083 (2020).

104. Dai, C. *et al.* Hollow zeolite encapsulated Ni–Pt bimetals for sintering and coking resistant dry reforming of methane. *J. Mater. Chem. A* **3**, 16461–16468 (2015).

105. Araiza, D. G., Arcos, D. G., Gómez-Cortés, A. & Díaz, G. Dry reforming of methane over Pt-Ni/CeO_2 catalysts: Effect of the metal composition on the stability. *Catal. Today* (2019)

doi:10.1016/j.cattod.2019.06.018.

106. Jawad, A., Rezaei, F. & Rownaghi, A. A. Highly efficient Pt/Mo-Fe/Ni-based Al_2O_3-CeO_2 catalysts for dry reforming of methane. *Catal. Today* **350**, 80–90 (2019).

107. Pawelec, B., Damyanova, S., Arishtirova, K., Fierro, J. L. G. & Petrov, L. Structural and surface features of PtNi catalysts for reforming of methane with CO_2. *Appl. Catal. A Gen.* **323**, 188–201 (2007).

108. Wang, A., Li, J. & Zhang, T. Heterogeneous single-atom catalysis. *Nat. Rev. Chem.* **2**, 65–81 (2018).

109. Li, X., Yang, X., Huang, Y., Zhang, T. & Liu, B. Supported noble-metal single atoms for heterogeneous catalysis. *Adv. Mater.* **31**, 1–19 (2019).

110. Hannagan, R. T., Giannakakis, G., Flytzani-Stephanopoulos, M. & Sykes, E. C. H. Single-atom alloy catalysis. *Chem. Rev.* (2020) doi:10.1021/acs.chemrev.0c00078.

111. Besenbacher, F. *et al.* Design of a surface alloy catalyst for steam reforming. *Science* **279**, 1913–1915 (1998).

112. Marcinkowski, M. D. *et al.* Pt/Cu single-atom alloys as coke-resistant catalysts for efficient C-H activation. *Nat. Chem.* **10**, 325–332 (2018).

113. Sun, G. *et al.* Breaking the scaling relationship via thermally stable Pt/Cu single atom alloys for catalytic dehydrogenation. *Nat. Commun.* **9**, (2018).

114. Meng, Y. *et al.* Theoretical research on a coke-resistant catalyst for the partial oxidation of methane: Pt/Cu single-atom alloys. *New J. Chem.* **44**, 3922–3929 (2020).

115. Ravel, B. & Newville, M. ATHENA, ARTEMIS, HEPHAESTUS: Data analysis for X-ray absorption spectroscopy using IFEFFIT. *J. Synchrotron Radiat.* **12**, 537–541 (2005).

116. Zhong, Y. J. *et al.* Highly efficient Ni@Ni–Pt/La_2O_3 catalyst for hydrogen generation from hydrous hydrazine decomposition: Effect of Ni–Pt surface alloying. *J. Power Sources* **300**, 294–300 (2015).

117. Huang, X. *et al.* High-performance transition metal-doped Pt_3Ni octahedra for oxygen reduction reaction. *Science* **348**, 1230–1234 (2015).

118. Tian, X. *et al.* Engineering bunched Pt-Ni alloy nanocages for efficient oxygen reduction in practical fuel cells. *Science* **366**, 850–856 (2019).

119. Tupy, S. A. *et al.* Correlating ethylene glycol reforming activity with in situ EXAFS detection of Ni segregation in supported NiPt bimetallic catalysts. *ACS Catal.* **2**, 2290–2296 (2012).

120. Guisbiers, G. *et al.* Size and shape effects on the phase diagrams of nickel-based bimetallic nanoalloys. *J. Phys. Chem. C* **121**, 6930–6939 (2017).

121. Buceta, D., Tojo, C., Vukmirovic, M. B., Deepak, F. L. & López-Quintela, M. A. Controlling bimetallic nanostructures by the microemulsion method with subnanometer resolution using a prediction model. *Langmuir* **31**, 7435–7439 (2015).

122. Hardacre, C., Rayment, T. & Lambert, R. M. Platinum/ceria CO oxidation catalysts derived from Pt/Ce crystalline alloy precursors. *J. Catal.* **158**, 102–108 (1996).

123. Abid, M., Paul-Boncour, V. & Touroude, R. Pt/CeO_2 catalysts in crotonaldehyde hydrogenation: Selectivity, metal particle size and SMSI states. *Appl. Catal. A Gen.* **297**, 48–59 (2006).

124. Beheshti Askari, A. *et al.* In situ X-ray microscopy reveals particle dynamics in a NiCo dry methane reforming catalyst under operating conditions. *ACS Catal.* **10**, 6223–6230 (2020).

125. Wang, C. *et al.* Coking and deactivation of a mesoporous Ni–CaO–ZrO_2 catalyst in dry reforming of methane: A study under different feeding compositions. *Fuel* **143**, 527–535 (2015).

126. Godínez-Salomón, F., Hallen-López, M. & Solorza-Feria, O. Enhanced electroactivity for the oxygen reduction on Ni@Pt core-shell nanocatalysts. *Int. J. Hydrogen Energy* **37**, 14902–14910 (2012).

127. Yan, B. *et al.* Dry reforming of ethane and butane with CO_2 over PtNi/CeO_2 bimetallic catalysts. *ACS Catal.* **6**, 7283–7292 (2016).

128. Fugane, K. *et al.* Improvement of cathode performance on Pt-CeO_x by optimization of electrochemical pretreatment condition for PEFC application. *Langmuir* **28**, 16692–16700 (2012).

129. Murphin Kumar, P. S. *et al.* Pt nanoparticles supported on mesoporous CeO_2 nanostructures obtained through green approach for efficient catalytic performance toward ethanol electro-oxidation. *ACS Sustain. Chem. Eng.* **5**, 11290–11299 (2017).

130. Singha, R. K. *et al.* Partial oxidation of methane to synthesis gas over Pt nanoparticles supported on nanocrystalline CeO_2 catalyst. *Catal. Sci. Technol.* **6**, 4601–4615 (2016).

131. Ye, R. P. *et al. High-performance of nanostructured Ni/CeO_2 catalyst on CO_2 methanation. Applied Catalysis B: Environmental* vol. 268 (Elsevier B.V., 2020).

132. Wang, C. *et al.* The importance of inner cavity space within Ni@SiO_2 nanocapsule catalysts for excellent coking resistance in the high-space-velocity dry reforming of methane. *Appl. Catal. B Environ.* **259**, 118019 (2019).

133. Lee, J., Ryou, Y., Chan, X., Kim, T. J. & Kim, D. H. How Pt interacts with CeO_2 under the reducing and oxidizing environments at elevated temperature: The origin of improved thermal stability of Pt/CeO_2 compared to CeO_2. *J. Phys. Chem. C* **120**, 25870–25879 (2016).

134. Vita, A. *et al.* Hydrogen-rich gas production by steam reforming of n-dodecane Part I: Catalytic activity of Pt/CeO_2 catalysts in optimized bed configuration. *Appl. Catal. B Environ.* **199**, 350–360 (2016).

135. Nie, L. *et al.* Activation of surface lattice oxygen in single-atom Pt/CeO_2 for low-temperature CO oxidation. *Science* **358**, 1419–1423 (2017).

136. de la Cruz-Flores, V. G., Martinez-Hernandez, A. & Gracia-Pinilla, M. A. Deactivation of

Ni-SiO_2 catalysts that are synthetized via a modified direct synthesis method during the dry reforming of methane. *Appl. Catal. A Gen.* **594**, 117455 (2020).

137. Lin, C. *et al.* Accelerated active phase transformation of NiO powered by Pt single atoms for enhanced oxygen evolution reaction. *Chem. Sci.* **9**, 6803–6812 (2018).
138. Oh, K. R. *et al.* In situ synthesis of trimeric ruthenium cluster-encapsulated ZIF-11 and its carbon derivatives for simultaneous conversion of glycerol and CO_2. *Chem. Mater.* **32**, 10084–10095 (2020).
139. Zhang, Z. *et al.* Thermally stable single atom Pt/m-Al_2O_3 for selective hydrogenation and CO oxidation. *Nat. Commun.* **8**, 1–10 (2017).
140. Qiao, B. *et al.* Single-atom catalysis of CO oxidation using Pt_1/FeO_x. *Nat. Chem.* **3**, 634–641 (2011).
141. Ogel, E. *et al.* Impact of preparation method and hydrothermal aging on particle size distribution of Pt/γ-Al_2O_3 and its performance in CO and NO Oxidation. *J. Phys. Chem. C* **123**, 5433–5446 (2019).
142. Ahmadi, M., Timoshenko, J., Behafarid, F. & Cuenya, B. R. Tuning the structure of Pt nanoparticles through support interactions: An in situ polarized X-ray absorption study coupled with atomistic simulations. *J. Phys. Chem. C* **123**, 10666–10676 (2019).
143. Siani, A., Captain, B., Adams, R. D., Alexeev, O. S. & Amiridis, M. D. Synthesis and structural characterization of SiO_2-supported PtFe catalysts prepared from $PtFe_2(C_8H_{12})(CO)_8$. *Top. Catal.* **54**, 318–333 (2011).
144. Nakaya, Y., Miyazaki, M., Yamazoe, S., Shimizu, K. I. & Furukawa, S. Active, selective, and durable catalyst for alkane dehydrogenation based on a well-designed trimetallic alloy. *ACS Catal.* **10**, 5163–5172 (2020).
145. H Sykes, E. C. & Christopher, P. Recent advances in single-atom catalysts and single-atom alloys: opportunities for exploring the uncharted phase space in-between. *Curr. Opin. Chem. Eng.* **29**, 67–73 (2020).
146. Arenas-Alatorre, J., Avalos-Borja, M. & Díaz, G. Microstructural characterization of bimetallic Ni–Pt catalysts supported on SiO_2. *Appl. Surf. Sci.* **189**, 7–17 (2002).
147. Ho, P. H. *et al.* Understanding structure-activity relationships in highly active La promoted Ni catalysts for CO_2 methanation. *Appl. Catal. B Environ.* **278**, (2020).
148. Gänzler, A. M. *et al.* Tuning the Pt/CeO_2 interface by in situ variation of the Pt particle size. *ACS Catal.* **8**, 4800–4811 (2018).
149. Mukainakano, Y. *et al.* Catalytic performance and characterization of Pt–Ni bimetallic catalysts for oxidative steam reforming of methane. *Chem. Eng. Sci.* **63**, 4891–4901 (2008).
150. Lucci, F. R. *et al.* Selective hydrogenation of 1,3-butadiene on platinum-copper alloys at the single-atom limit. *Nat. Commun.* **6**, (2015).
151. Wang, H. *et al.* Quasi Pd_1Ni single-atom surface alloy catalyst enables hydrogenation of nitriles to secondary amines. *Nat. Commun.* **10**, (2019).

152. Zhang, X. *et al.* Platinum–copper single atom alloy catalysts with high performance towards glycerol hydrogenolysis. *Nat. Commun.* **10**, 5812 (2019).

153. Zhang, Z. L. & Verykios, X. E. Carbon dioxide reforming of methane to synthesis gas over supported Ni catalysts. *Catal. Today* **21**, 589–595 (1994).

154. Richardson, J. T., Garrait, M. & Hung, J. K. Carbon dioxide reforming with Rh and Pt–Re catalysts dispersed on ceramic foam supports. *Appl. Catal. A Gen.* **255**, 69–82 (2003).

155. Al Abdulghani, A. J. *et al.* Methane dry reforming on supported cobalt nanoparticles promoted by boron. *J. Catal.* **392**, 126–134 (2020).

156. Lemonidou, A. A. & Vasalos, I. A. Carbon dioxide reforming of methane over 5 wt.% Ni/CaO-Al_2O_3 catalyst. *Appl. Catal. A Gen.* **228**, 227–235 (2002).

157. Múnera, J. F. *et al.* Kinetics and reaction pathway of the CO_2 reforming of methane on Rh supported on lanthanum-based solid. *J. Catal.* **245**, 25–34 (2007).

158. Ayodele, B. V., Khan, M. R., Lam, S. S. & Cheng, C. K. Production of CO-rich hydrogen from methane dry reforming over lanthania-supported cobalt catalyst: Kinetic and mechanistic studies. *Int. J. Hydrogen Energy* **41**, 4603–4615 (2016).

159. Xie, Z. *et al.* Dry reforming of methane over CeO_2-supported Pt-Co catalysts with enhanced activity. *Appl. Catal. B Environ.* **236**, 280–293 (2018).

160. Ayodele, B. V., Khan, M. R. & Cheng, C. K. Syngas production from CO_2 reforming of methane over ceria supported cobalt catalyst: Effects of reactants partial pressure. *J. Nat. Gas Sci. Eng.* **27**, 1016–1023 (2015).

161. Xie, Z. *et al.* Effects of oxide supports on the CO_2 reforming of ethane over Pt-Ni bimetallic catalysts. *Appl. Catal. B Environ.* **245**, 376–388 (2019).

162. El Hassan, N. *et al.* Low temperature dry reforming of methane on rhodium and cobalt based catalysts: Active phase stabilization by confinement in mesoporous SBA-15. *Appl. Catal. A Gen.* **520**, 114–121 (2016).

163. Li, Z., Jiang, B., Wang, Z. & Kawi, S. High carbon resistant Ni@Ni phyllosilicate@SiO_2 core shell hollow sphere catalysts for low temperature CH_4 dry reforming. *J. CO_2 Util.* **27**, 238–246 (2018).

164. Jiang, S., Lu, Y., Wang, S., Zhao, Y. & Ma, X. Insight into the reaction mechanism of CO_2 activation for CH_4 reforming over NiO-MgO: A combination of DRIFTS and DFT study. *Appl. Surf. Sci.* **416**, 59–68 (2017).

165. Buelens, L. C., Galvita, V. V., Poelman, H., Detavernier, C. & Marin, G. B. Super-dry reforming of methane intensifies CO_2 utilization via Le Chatelier's principle. *Science* **354**, 449–452 (2016).

166. Panagiotopoulou, P. & Kondarides, D. I. Effects of alkali additives on the physicochemical characteristics and chemisorptive properties of Pt/TiO_2 catalysts. *J. Catal.* **260**, 141–149 (2008).

167. Freysz, J. L., Saussey, J., Lavalley, J. C. & Bourges, P. In situ FTIR study of the NO+CO

reaction on a silica-supported platinum catalyst at atmospheric pressure using a new pulse technique. *J. Catal.* **197**, 131–138 (2001).

168. García-Diéguez, M., Finocchio, E., Larrubia, M. Á., Alemany, L. J. & Busca, G. Characterization of alumina-supported Pt, Ni and PtNi alloy catalysts for the dry reforming of methane. *J. Catal.* **274**, 11–20 (2010).

169. Gould, T. D. *et al.* Enhanced dry reforming of methane on Ni and Ni-Pt catalysts synthesized by atomic layer deposition. *Appl. Catal. A Gen.* **492**, 107–116 (2015).

170. Jaiswar, V. K., Katheria, S., Deo, G. & Kunzru, D. Effect of Pt doping on activity and stability of Ni/$MgAl_2O_4$ catalyst for steam reforming of methane at ambient and high pressure condition. *Int. J. Hydrogen Energy* **42**, 18968–18976 (2017).

171. Araújo, J. C. S. *et al.* The role of Pt loading on La_2O_3-Al_2O_3 support for methane conversion reactions via partial oxidation and steam reforming. *Fuel* **254**, 115681 (2019).

172. Tierney, H. L., Baber, A. E., Kitchin, J. R. & Sykes, E. C. H. Hydrogen dissociation and spillover on individual isolated palladium atoms. *Phys. Rev. Lett.* **103**, 1–4 (2009).

173. Kyriakou, G. *et al.* Isolated metal atom geometries as a strategy for selective heterogeneous hydrogenations. *Science* **335**, 1209–1212 (2012).

174. Moraes, T. S. *et al.* Ethanol conversion at low temperature over CeO_2—supported Ni-based catalysts. Effect of Pt addition to Ni catalyst. *Appl. Catal. B Environ.* **181**, 754–768 (2016).

175. Zhou, L. *et al.* Light-driven methane dry reforming with single atomic site antenna-reactor plasmonic photocatalysts. *Nat. Energy* **5**, 61–70 (2020).

176. Liu, J. *et al.* Tackling CO Poisoning with Single-Atom Alloy Catalysts. *J. Am. Chem. Soc.* **138**, 6396–6399 (2016).

177. Gamler, J. T. L. *et al.* Effect of lattice mismatch and shell thickness on strain in core@shell nanocrystals. *Nanoscale Adv.* **2**, 1105–1114 (2020).

178. Zhu, J. *et al.* Deconvolution of the particle size effect on CO_2 hydrogenation over iron-based catalysts. *ACS Catal.* **10**, 7424–7433 (2020).

179. Marchionni, V., Nachtegaal, M. & Ferri, D. Influence of CO on dry CH_4 oxidation on Pd/Al_2O_3 by operando spectroscopy: A multitechnique modulated excitation study. *ACS Catal.* **10**, 4791–4804 (2020).

180. Gao, P. *et al.* Direct production of lower olefins from CO_2 conversion via bifunctional catalysis. *ACS Catal.* **8**, 571–578 (2018).

181. Ma, Z. & Porosoff, M. D. Development of tandem catalysts for CO_2 hydrogenation to olefins. *ACS Catal.* **9**, 2639–2656 (2019).

182. Wang, J. *et al.* High-performance MaZrOx (Ma = Cd, Ga) Solid-Solution Catalysts for CO_2 Hydrogenation to Methanol. *ACS Catal.* **9**, 10253–10259 (2019).

183. Taheri Najafabadi, A., Fatemi, S., Sohrabi, M. & Salmasi, M. Kinetic modeling and optimization of the operating condition of MTO process on SAPO-34 catalyst. *J. Ind. Eng.*

Chem. **18**, 29–37 (2012).

184. Li, Z. *et al.* Highly selective conversion of carbon dioxide to lower olefins. *ACS Catal.* **7**, 8544–8548 (2017).

185. Liu, X. *et al.* Design of efficient bifunctional catalysts for direct conversion of syngas into lower olefins via methanol/dimethyl ether intermediates. *Chem. Sci.* **9**, 4708–4718 (2018).

186. Gao, J., Jia, C. & Liu, B. Direct and selective hydrogenation of CO_2 to ethylene and propene by bifunctional catalysts. *Catal. Sci. Technol.* **7**, 5602–5607 (2017).

187. Numpilai, T., Wattanakit, C., Chareonpanich, M., Limtrakul, J. & Witoon, T. Optimization of synthesis condition for CO_2 hydrogenation to light olefins over In_2O_3 admixed with SAPO-34. *Energy Convers. Manag.* **180**, 511–523 (2019).

188. Tsoukalou, A. *et al.* Structural evolution and dynamics of an In_2O_3 catalyst for CO_2 hydrogenation to methanol: An operando XAS-XRD and in situ TEM study. *J. Am. Chem. Soc.* **141**, 13497–13505 (2019).

189. Martin, O. *et al.* Indium oxide as a superior catalyst for methanol synthesis by CO_2 hydrogenation. *Angew. Chemie - Int. Ed.* **55**, 6261–6265 (2016).

190. Ye, J., Liu, C., Mei, D. & Ge, Q. Active oxygen vacancy site for methanol synthesis from CO_2 hydrogenation on In_2O_3(110): A DFT study. *ACS Catal.* **3**, 1296–1306 (2013).

191. Frei, M. S. *et al.* Role of zirconia in indium oxide-catalyzed CO_2 hydrogenation to methanol. *ACS Catal.* **10**, 1133–1145 (2020).

192. Zhang, M., Dou, M. & Yu, Y. Theoretical study of the promotional effect of ZrO_2 on In_2O_3 catalyzed methanol synthesis from CO_2 hydrogenation. *Appl. Surf. Sci.* **433**, 780–789 (2018).

193. Dang, S. *et al.* Role of zirconium in direct CO_2 hydrogenation to lower olefins on oxide/zeolite bifunctional catalysts. *J. Catal.* **364**, 382–393 (2018).

194. Zhu, J., Van Ommen, J. G., Bouwmeester, H. J. M. & Lefferts, L. Activation of O_2 and CH_4 on yttrium-stabilized zirconia for the partial oxidation of methane to synthesis gas. *J. Catal.* **233**, 434–441 (2005).

195. Dole, H. A. E. *et al.* Low temperature toluene oxidation over Pt nanoparticles supported on yttria stabilized-zirconia. *Catal. Letters* **143**, 996–1002 (2013).

196. Dang, S. *et al.* Rationally designed indium oxide catalysts for CO_2 hydrogenation to methanol with high activity and selectivity. *Sci. Adv.* **6**, (2020).

197. Ahmad, M. S. *et al.* Effect of reaction conditions on the lifetime of SAPO-34 catalysts in methanol to olefins process – A review. *Fuel* **283**, 118851 (2021).

198. Han, L. *et al.* Polyacrylamide-assisted synthesis of hierarchical porous SAPO-34 zeolites with excellent MTO catalytic performance. *Microporous Mesoporous Mater.* **311**, 110676 (2021).

199. Gao, S. *et al.* Insight into the deactivation mode of methanol-to-olefins conversion over

SAPO-34: Coke, diffusion, and acidic site accessibility. *J. Catal.* **367**, 306–314 (2018).

200. Zhong, J. *et al.* Recent advances of the nano-hierarchical SAPO-34 in the methanol-to-olefin (MTO) reaction and other applications. *Catal. Sci. Technol.* **7**, 4905–4923 (2017).

201. Sun, Q., Wang, N., Bai, R., Chen, X. & Yu, J. Seeding induced nano-sized hierarchical SAPO-34 zeolites: cost-effective synthesis and superior MTO performance. *J. Mater. Chem. A* **4**, 14978–14982 (2016).

202. Vasanthavel, S. & Kannan, S. Structural investigations on the tetragonal to cubic phase transformations in zirconia induced by progressive yttrium additions. *J. Phys. Chem. Solids* **112**, 100–105 (2018).

203. Basahel, S. N., Ali, T. T., Mokhtar, M. & Narasimharao, K. Influence of crystal structure of nanosized ZrO_2 on photocatalytic degradation of methyl orange. *Nanoscale Res. Lett.* **10**, (2015).

204. Baklanova, N. I., Kolesov, B. A. & Zima, T. M. Raman study of yttria-stabilized zirconia interfacial coatings on Nicalon^{TM} fiber. *J. Eur. Ceram. Soc.* **27**, 165–171 (2007).

205. Deshpande, S., Patil, S., Kuchibhatla, S. V. & Seal, S. Size dependency variation in lattice parameter and valency states in nanocrystalline cerium oxide. *Appl. Phys. Lett.* **87**, 1–3 (2005).

206. Li, Y. *et al.* Investigation of oxygen vacancy and photoluminescence in calcium tungstate nanophosphors with different particle sizes. *Mater. Res. Bull.* **50**, 36–41 (2014).

207. Chen, T. Y. *et al.* Unraveling highly tunable selectivity in CO_2 hydrogenation over bimetallic In-Zr oxide catalysts. *ACS Catal.* **9**, 8785–8797 (2019).

208. Numpilai, T. *et al.* CO_2 hydrogenation to methanol at high reaction temperatures over In_2O_3/ZrO_2 catalysts: Influence of calcination temperatures of ZrO_2 support. *Catal. Today* (2020) doi:10.1016/j.cattod.2020.03.011.

209. Rahman, S. *et al.* Mesoporous TUD-1 supported indium oxide nanoparticles for epoxidation of styrene using molecular O_2. *RSC Adv.* **5**, 46850–46860 (2015).

210. Ramirez, A., Gevers, L., Bavykina, A., Ould-Chikh, S. & Gascon, J. Metal organic framework-derived iron catalysts for the direct hydrogenation of CO_2 to short chain olefins. *ACS Catal.* **8**, 9174–9182 (2018).

211. Jiang, X. *et al.* A combined experimental and DFT study of H_2O effect on In_2O_3/ZrO_2 catalyst for CO_2 hydrogenation to methanol. *J. Catal.* **383**, 283–296 (2020).

212. Yang, G. *et al.* Nanosize-enhanced lifetime of SAPO-34 catalysts in methanol-to-olefin reactions. *J. Phys. Chem. C* **117**, 8214–8222 (2013).

213. Chen, G., Sun, Q. & Yu, J. Nanoseed-assisted synthesis of nano-sized SAPO-34 zeolites using morpholine as the sole template with superior MTO performance. *Chem. Commun.* **53**, 13328–13331 (2017).

214. Tada, S. *et al.* Cu species incorporated into amorphous ZrO_2 with high activity and selectivity in CO_2-to-methanol hydrogenation. *J. Phys. Chem. C* **122**, 5430–5442 (2018).

215. Witoon, T., Chalorngtham, J., Dumrongbunditkul, P., Chareonpanich, M. & Limtrakul, J. CO_2 hydrogenation to methanol over Cu/ZrO_2 catalysts: Effects of zirconia phases. *Chem. Eng. J.* **293**, 327–336 (2016).

216. Dou, M., Zhang, M., Chen, Y. & Yu, Y. Theoretical study of methanol synthesis from CO_2 and CO hydrogenation on the surface of ZrO_2 supported In_2O_3 catalyst. *Surf. Sci.* **672–673**, 7–12 (2018).

217. Köck, E. M., Kogler, M., Bielz, T., Klötzer, B. & Penner, S. In situ FT-IR spectroscopic study of CO_2 and CO adsorption on Y_2O_3, ZrO_2, and yttria-stabilized ZrO_2. *J. Phys. Chem. C* **117**, 17666–17673 (2013).

218. Pustovarenko, A. *et al.* Metal−organic framework-derived synthesis of cobalt indium catalysts for the hydrogenation of CO_2 to methanol. *ACS Catal.* **10**, 5064–5076 (2020).

219. Wang, P., Zha, F., Yao, L. & Chang, Y. Synthesis of light olefins from CO_2 hydrogenation over (CuO-ZnO)-kaolin/SAPO-34 molecular sieves. *Appl. Clay Sci.* **163**, 249–256 (2018).

220. Han, J. *et al.* Simultaneous evaluation of reaction and diffusion over molecular sieves for shape-selective catalysis. *ACS Catal.* **10**, 8727–8735 (2020).

221. Hoch, L. B. *et al.* The rational design of a single-component photocatalyst for gas-phase CO_2 reduction using both UV and visible light. *Adv. Sci.* **1**, 1400013 (2014).

222. Samson, K. *et al.* Influence of ZrO_2 structure and copper electronic state on activity of Cu/ZrO_2 catalysts in methanol synthesis from CO_2. *ACS Catal.* **4**, 3730–3741 (2014).

223. Zhang, Y. *et al.* Structure−activity−selectivity relationships in propane dehydrogenation over Rh/ZrO_2 catalysts. *ACS Catal.* **10**, 6377–6388 (2020).

224. Frei, M. S. *et al.* Atomic-scale engineering of indium oxide promotion by palladium for methanol production via CO_2 hydrogenation. *Nat. Commun.* **10**, 1–11 (2019).

225. T. Merle-Méjean, P. Barberis, S. B. Othmane, F. Nardou, P. E. Q. Chemical forms of hydroxyls on/in zirconia: An FT-IR study. *J. Eur. Ceram. Soc.* **18**, 1579–1586 (1998).

226. Peng, Q. *et al.* Tuning hydrocarbon pool intermediates by the acidity of SAPO-34 catalysts for improving methanol-to-olefins reaction. *ACS Sustain. Chem. Eng.* **6**, 16867–16875 (2018).

227. Liu, X. *et al.* Tandem catalysis for hydrogenation of CO and CO_2 to lower olefins with bifunctional catalysts composed of spinel oxide and SAPO-34. *ACS Catal.* **10**, 8303–8314 (2020).